

1 LEVERAGING MULTI-MESSENGER ASTROPHYSICS FOR DARK MATTER SEARCHES

By

Daniel Nicholas Salazar-Gallegos

A DISSERTATION

Submitted to  
Michigan State University  
in partial fulfillment of the requirements  
for the degree of

Physics—Doctor of Philosophy  
Computational Mathematics in Science and Engineering—Dual Major

Today

**ABSTRACT**

3 I did Dark Matter with HAWC and IceCube. I also used Graph Neural Networks

<sup>4</sup> Copyright by

<sup>5</sup> DANIEL NICHOLAS SALAZAR-GALLEGOS

<sup>6</sup> Today

## ACKNOWLEDGMENTS

8 I love my friends. Thanks to everyone that helped me figure this out. Amazing thanks to the people  
9 at LANL who supported me. Eames, etc Dinner Parties Jenny and her child Kaydince Kirsten, Pat,  
10 Andrea Family. You're so far but so critical to my formation. Unconditional love. Roommate

## TABLE OF CONTENTS

12	LIST OF TABLES . . . . .	vii
13	LIST OF FIGURES . . . . .	viii
14	LIST OF ABBREVIATIONS . . . . .	xv
15	CHAPTER 1      INTRODUCTION . . . . .	1
16	CHAPTER 2      DARK MATTER IN THE COSMOS . . . . .	2
17	2.1 Introduction . . . . .	2
18	2.2 Dark Matter Basics . . . . .	3
19	2.3 Evidence for Dark Matter . . . . .	4
20	2.4 Searching for Dark Matter: Particle DM . . . . .	11
21	2.5 Sources for Indirect Dark Matter Searches . . . . .	16
22	2.6 Multi-Messenger Dark Matter . . . . .	18
23	CHAPTER 3      MULTIMESSENGER ASTROPHYSICS: DETECTING HIGH EN-	
24	ERGY NEUTRAL MESSENGERS . . . . .	21
25	3.1 Introduction . . . . .	21
26	3.2 Charged Particles in a Medium . . . . .	21
27	3.3 Photons ( $\gamma$ ) . . . . .	22
28	3.4 Neutrinos ( $\nu$ ) . . . . .	22
29	3.5 Opportunities to Combine for Dark Matter . . . . .	22
30	CHAPTER 4      HIGH ALTITUDE WATER CHERENKOV (HAWC) OBSERVATORY .	24
31	4.1 The Detector . . . . .	24
32	4.2 Events Reconstruction and Data Acquisition . . . . .	24
33	4.3 Remote Monitoring . . . . .	24
34	CHAPTER 5      ICECUBE NEUTRINO OBSERVATORY . . . . .	25
35	5.1 The Detector . . . . .	25
36	5.2 Events Reconstruction and Data Acquisition . . . . .	25
37	5.3 Northern Test Site . . . . .	25
38	CHAPTER 6      GLORY DUCK: MULTI-WAVELENGTH SEARCH FOR DARK MATT-	
39	TER ANNIHILATION TOWARDS DWARF SPHEROIDAL GALAX-	
40	IES . . . . .	26
41	6.1 Introduction . . . . .	26
42	6.2 Dataset and Background . . . . .	28
43	6.3 Analysis . . . . .	29
44	6.4 Likelihood Methods . . . . .	34
45	6.5 HAWC Results . . . . .	40
46	6.6 Glory Duck Combined Results . . . . .	43
47	6.7 HAWC Systematics . . . . .	48

48	6.8 <i>J</i> -factor distributions . . . . .	49
49	6.9 Discussion and Conclusions . . . . .	55
50	<b>CHAPTER 7        MULTITHREADING HAWC ANALYSES FOR DARK MATTER</b>	
51	<b>SEARCHES . . . . .</b>	59
52	7.1 Introduction . . . . .	59
53	7.2 Dataset and Background . . . . .	59
54	7.3 Analysis . . . . .	61
55	7.4 Likelihood Methods . . . . .	64
56	7.5 Computational Methods: Multithreading . . . . .	65
57	7.6 Analysis Results . . . . .	71
58	7.7 Systematics . . . . .	72
59	7.8 Conclusion and Discussion . . . . .	73
60	<b>CHAPTER 8        HEAVY DARK MATTER ANNIHILATION SEARCH WITH ICE-</b>	
61	<b>CUBE'S NORTH SKY TRACK DATA . . . . .</b>	79
62	<b>CHAPTER 9        NU DUCK . . . . .</b>	80
63	<b>APPENDIX A      MULTI-EXPERIMENT SUPPLEMENTARY FIGURES . . . . .</b>	81
64	<b>APPENDIX B      MULTITHREADING DARK MATTER ANALYSES SUPPLEMEN-</b>	
65	<b>TARY MATERIAL . . . . .</b>	82
66	B.1 Remaining Spectral Models . . . . .	82
67	B.2 <code>mpu_analysis.py</code> . . . . .	83
68	B.3 Comparison with Glory Duck . . . . .	92
69	<b>BIBLIOGRAPHY . . . . .</b>	95

## LIST OF TABLES

<p>71    Table 6.1    Summary of the relevant properties of the dSphs used in the present work. Column 1 lists the dSphs. Columns 2 and 3 present their heliocentric distance and galactic coordinates, respectively. Columns 4 and 5 report the <math>J</math>-factors of each source given from the <math>\mathcal{GS}</math> and <math>\mathcal{B}</math> independent studies and their estimated <math>\pm 1\sigma</math> uncertainties. The values <math>\log_{10} J</math> (<math>\mathcal{GS}</math> set) [45] correspond to the mean <math>J</math>-factor values for a source extension truncated at the outermost observed star. The values <math>\log_{10} J</math> (<math>\mathcal{B}</math> set) [47] are provided for a source extension at the tidal radius of each dSph. <b>Bolded sources are within HAWC's field of view and provided to the Glory Duck analysis.</b> . . . . .</p> <p>80    Table 6.2    Summary of dSph observations by each experiment used in this work. A ‘-’ indicates the experiment did not observe the dSph for this study. For Fermi-LAT, the exposure at 1 GeV is given. For HAWC, <math> \Delta\theta </math> is the absolute difference between the source declination and HAWC latitude. HAWC is more sensitive to sources with smaller <math> \Delta\theta </math>. For IACTs, we show the zenith angle range, the total exposure, the energy range, the angular radius <math>\theta</math> of the signal or ON region, the ratio of exposures between the background-control (OFF) and signal (ON) regions (<math>\tau</math>), and the significance of gamma-ray excess in standard deviations, <math>\sigma</math>. . . . .</p> <p>89    Table 7.1    Summary of the relevant properties of the dSphs used in the present work. Column 1 lists the dSphs. Columns 2 and 3 present their heliocentric distance and galactic coordinates, respectively. Column 4 reports the <math>J</math>-factors of each source given from the <math>\mathcal{LS}</math> studies and estimated <math>\pm 1\sigma</math> uncertainties. The values <math>\log_{10} J</math> (<math>\mathcal{LS}</math> set) [65] correspond to the mean <math>J</math>-factor values for a source extension truncated at <math>0.5^\circ</math>. . . . .</p> <p>95    Table 7.2    Timing summaries for analyses for serial and multithreaded processes. <math>M</math> tasks is the number of functional-parallel tasks ran for the computation. <math>T_{p,c}</math> is a single run time in hours:minutes:seconds for runs utilizing <math>p</math> nodes and <math>c</math> threads. Runs are run interactively on the same computer to maximize consistency. Empty entries are indicated with ‘-’. (.) entries are estimated entries extrapolated from data earlier in the column. . . . .</p> <p>101    Table 7.3    Speed up summaries for analyses for serial and multithreaded processes. <math>M</math> tasks is the number of functional-parallel tasks ran for the computation. <math>S_{p,c}</math> is a single speedup comparison for runs utilizing <math>p</math> nodes and <math>c</math> threads. <math>[\cdot]</math> are the estimated speedups calculated from Tab. 7.2, Eq. (7.10), and Eq. (7.5). Empty entries are indicated with ‘-’. . . . .</p> <p>106    Proof I know how to include</p>	<p>34</p> <p>35</p> <p>65</p> <p>69</p> <p>71</p>
--	---

## LIST OF FIGURES

108	Figure 2.1	Rotation curve fit to NGC 6503 from [7]. Dashed line is the contribution 109 from visible matter. Dotted curves are from gas. Dash-dot curves are from 110 dark matter (DM). Solid line is the composite contribution from all matter 111 and DM sources. Data are indicated with bold dots with error bars. Data 112 agree strongly with a matter + DM composite prediction. . . . .	5
113	Figure 2.2	Light from distant galaxy is bent in unique ways depending on the distribution 114 of mass between the galaxy and Earth. Yellow dashed lines indicate where 115 the light would have gone if the matter were not present [8]. . . . .	7
116	Figure 2.3	(left) Optical image of galactic cluster 1E0657-558. (right) X-ray image of the 117 cluster with redder meaning hotter and higher baryon density. (both) Green 118 contours are reconstruction of gravity contours from weak lensing. White 119 rings are the best fit mass maxima at 68.3%, 95.5%, and 99.7% confidence. 120 The matter maxima of the clusters are clearly separated from x-ray maxima. [9]	8
121	Figure 2.4	Plank CMB sky. Sky map features small variations in temperature in primor- 122 dial light. These anisotropies are used to make inferences about the universe's 123 energy budget and developmental history. [10] . . . . .	9
124	Figure 2.5	Observed Cosmic Microwave Background power spectrum as a function of 125 multipole moment from Plank [10]. Blue line is best fit model from $\Lambda$ CDM. 126 Red points and lines are data and error, respectively. . . . .	10
127	Figure 2.6	Predicted power spectra of CMB for different $\Omega_m h^2$ values for fixed baryon 128 density from [11]. (left) Low $\Omega_m h^2$ increases the prominence of first and 129 second peaks. (middle) $\Omega_m h^2$ is most similar to the observed power spectrum. 130 The second and third peaks are similar in height. (right) $\Omega_m h^2$ is large which 131 suppresses the first peak and raises the prominence of the third peak. . . . .	10
132	Figure 2.7	The Standard Model (SM) of particle physics. Figure taken from <a href="http://www.quantumdiaries.org/2014/03/14/the-standard-model-a-beautiful-but-flawed-theory/">http://www.quantumdiaries.org/2014/03/14/the-standard-model-a-beautiful-but-flawed-theory/</a> . . . . .	12
135	Figure 2.8	Simplified Feynman diagram demonstrating with different ways DM can 136 interact with SM particles. The 'X's refer to the DM particles whereas the 137 SM refer to fundamental particles in the SM. The large circle in the center 138 indicates the vertex of interaction and is purposely left vague. The colored 139 arrows refer to different directions of time as well as their respective labels. 140 The arrows indicate the initial and final state of the DM -SM interaction in time.	13

141	Figure 2.9 A single jet event in ATLAS detector from 2017 [16]. Jet momentum was 142 observed to be 1.9 TeV. Missing transverse momentum was observed to be 143 1.9 TeV compared to the initial transverse momentum of the event was 0. 144 Implied MET is traced by a red dashed line in event display. . . . .	14
145	Figure 2.10 More detailed pseudo-Feynman diagram of particle cascade from dark matter 146 annihilation into 2 quarks. The quarks hadronize and down to stable particles 147 like $\gamma$ or the anti-proton ( $p^-$ ). Diagram pulled from ICRC 2021 presentation 148 on DM annihilation search [17]. . . . .	15
149	Figure 2.11 Dark Matter (DM) decay spectrum for $b\bar{b}$ initial state and $\gamma$ final state. Redder 150 spectra are for larger DM masses. Bluer spectra are light DM masses. $x$ is a 151 unitless factor defined as the ratio of the mass of DM, $m_\chi$ , and the final state 152 particle energy $E_\gamma$ . Figure from [19]. . . . .	17
153	Figure 2.12 Different dark matter density profiles compared. Some models produce ex- 154 ceptionally large densities at small r [20]. . . . .	18
155	Figure 2.13 The Milky Way Galaxy in photons ( $\gamma$ ) and neutrinos ( $\nu$ ) [22]. The Galactic 156 center is at $l=0^\circ$ and is the brightest region in all panels. (top) An Optical 157 color image of the Milky Way galaxy seen from Earth. Clouds of gas and dust 158 obscure some light from stars. (2nd down) Integrated flux of $\gamma$ -rays observed 159 by the Fermi-LAT telescope [23]. (middle) Expected neutrino emission 160 that corresponds with Fermi-LAT observations. (2nd up) Expected neutrino 161 emission profile after considering detector systematics of IceCube. (bottom) 162 Observed neutrino emission from region of the galactic plane. Substantial 163 neutrino emission was detected. . . . .	19
164	Figure 2.14 Dark Matter annihilation spectra for different final state particle and standard 165 model annihilation channels [24]. Photons (red), $e^\pm$ (green), $\bar{p}$ (blue), $\nu$ (black). . . . .	20
166	Figure 3.1 TODO: Show a nuclear reactor with cherenkov radiation[NEEDS A SOURCE][FACT 167 CHECK THIS] . . . . .	22
168	Figure 3.2 TODO: absorption spectrum of liquid and solid water[NEEDS A SOURCE][FACT 169 CHECK THIS] . . . . .	23

170	Figure 6.1 Sensitivities of five gamma-ray experiments compared to percentages of the Crab nebula's emission and dark matter annihilation. Solid lines present estimated sensitivities to power law spectra [FACT CHECK THIS]for each experiment. Green lines are Fermi-LAT sensitivities where lighter green is the sensitivity to the galactic center and dark green is its sensitivity to higher declinations. Orange, red, and purple solid lines represent the MAGIC, HESS, and VERITAS 50 hour sensitivities respectively. The maroon and brown lines are the HAWC 1 year and 5 year sensitivities. Across four decades of gamma-ray energy, these experiments have similar sensitivities on the order $10^{-12}$ erg cm $^{-2}$ s $^{-1}$ . The dotted lines are estimated dark matter fluxes assuming $m_\chi = 5$ TeV DM annihilating to bottom quarks (red), tau leptons (blue), and W bosons (green). Faded gray lines outline percentage flux of the Crab nebula. Figure is an augmented version of [25]	27
183	Figure 6.2 Effect of Electroweak (EW) corrections on expected DM annihilation spectrum for $\chi\chi \rightarrow W^-W^+$ . Solid lines are spectral models that consider EW corrections. Dash-dot lines are spectral models without EW corrections. Red lines are models for $M_\chi = 1$ TeV. Blue lines represent models for $M_\chi = 100$ TeV. All models are sourced from the PPPC4DMID [44].	31
188	Figure 6.3 $\frac{dJ}{d\Omega}$ maps for Segue1 (top) and Coma Berenices (bottom). Origin is centered on the specific dwarf spheroidal galaxies (dSph). X and Y axes are the angular separation from the center of the dwarf. Plots of the remaining 11 dSph HAWC studied are linked in Fig. A.1	33
192	Figure 6.4 Illustration of the combination technique showing a comparison between $-2 \ln \lambda$ provided by four instruments (colored lines) from the observation of the same dSph without any $J$ nuisance and their sum, <i>i.e.</i> the resulting combined likelihood (thin black line). According to the test statistics of Equation (6.6), the intersection of the likelihood profiles with the line $-2 \ln \lambda = 2.71$ indicates the 95% C.L. upper limit on $\langle \sigma v \rangle$ . The combined likelihood (thin black line) shows a smaller value of upper limit on $\langle \sigma v \rangle$ than those derived by individual instruments. We also show how the uncertainties on the $J$ factor effects the combined likelihood and degrade the upper limit on $\langle \sigma v \rangle$ (thick black line). All likelihood profiles are normalized so that the global minimum $\widehat{\langle \sigma v \rangle}$ is 0. We note that each profile depends on the observational conditions in which a target object was observed. The sensitivity of a given instrument can be degraded and the upper limits less constraining if the observations are performed in non-optimal conditions such as a high zenith angle or a short exposure time.	38
207	Figure 6.5	41

208	Figure 6.6 HAWC TS values for best fit $\langle\sigma v\rangle$ versus $m_\chi$ for seven SM annihilation channels with $J$ factors from $\mathcal{GS}$ . The solid black line shows the combined best fit TS values. The colored, dashed lines are the TS values for each of the 13 sources HAWC studied.	42
212	Figure 6.7 HAWC Brazil bands at 95% confidence level on $\langle\sigma v\rangle$ versus DM mass for seven annihilation channels with $J$ -factors from $\mathcal{GS}$ [53]. The solid line represents the combined limit from 13 dSphs. The dashed line is the expected limit. The green band is the 68% containment. The yellow band is the 95% containment.	43
217	Figure 6.8 Upper limits at 95% confidence level on $\langle\sigma v\rangle$ in function of the DM mass for eight annihilation channels, using the set of $J$ factors from Ref. [53] ( $\mathcal{GS}$ set in Table 6.1). The black solid line represents the observed combined limit, the black dashed line is the median of the null hypothesis corresponding to the expected limit, while the green and yellow bands show the 68% and 95% containment bands. Combined upper limits for each individual detector are also indicated as solid, colored lines. The value of the thermal relic cross-section in function of the DM mass is given as the red dotted-dashed line [54].	44
226	Figure 6.9 Same as Fig. 6.8, using the set of $J$ factors from Ref. [47, 55] ( $\mathcal{B}$ set in Table 6.1).	45
227	Figure 6.10 Comparisons of the combined limits at 95% confidence level for each of the eight annihilation channels when using the $J$ factors from Ref. [53] ( $\mathcal{GS}$ set in Table 6.1), plain lines, and the $J$ factor from Ref. [47, 55] ( $\mathcal{B}$ set in Table 6.1), dashed lines. The cross-section given by the thermal relic is also indicated [54].	47
231	Figure 6.11 Comparisons of the combined limits at 95% confidence level for a point source analysis and extended source using [53] $\mathcal{GS}$ J-factor distributions and PPPC [44] annihilation spectra. Shown are the limits for Segue1 which will have the most significant impact on the combined limit. 6 of the 7 DM annihilation channels are shown. Solid lines are extended source studies. Dashed lines are point source studies. Overall, the extended source analysis improves the limit by a factor of 2.	49
238	Figure 6.12 Same as Fig. 6.11 on Coma Berenices. This dSph also contributes significantly to the limit. The limits are identical in this case.	50
240	Figure 6.13 Comparison of combined limits when correcting for HAWC's pointing systematic. All DM annihilation channels are shown. The solid black line is the ratio between published limit to the declination corrected limit. The blue solid line or "Combined_og" represented the limits computed for Glory Duck. The solid orange line or "Combined_ad" represented the limits computed after correcting for the pointing systematic.	51

246	Figure 6.14 Differential map of $dJ/\Omega$ from model built in Section 6.8.1 and profiles provided directly from authors. (Top) Differential from Segue1. (bottom) Differential from Coma Berenices. Note that their scales are not the same. Segue1 shows the deepest discrepancies which is congruent with its large uncertainties. Both models show anuli where unique models become apparent.	52
251	Figure 6.15 HAWC limits for Coma Berenices (top) and Segue1 (bottom) for two different map sets. Blue lines are limits calculated on maps with poor model representation. Orange lines are limits calculated on spatial profiles provided by the authors of [45]. Black line is the ratio of the poor spatial model limits to the corrected spatial models. The left y-axis measures $\langle\sigma v\rangle$ for the blue and orange lines. The right y-axis measures the ratio and is unitless.	53
257	Figure 6.16 Comparisons between the $J$ -factors versus the angular radius for the computation of $J$ factors from Ref. [53] ( $\mathcal{GS}$ set in Table 6.1) in blue and for the computation from Ref. [47, 55] ( $\mathcal{B}$ set in Tab. 6.1) in orange. The solid lines represent the central value of the $J$ -factors while the shaded regions correspond to the $1\sigma$ standard deviation.	56
262	Figure 6.17 Comparisons between the $J$ -factors versus the angular radius for the computation of $J$ factors from Ref. [53] ( $\mathcal{GS}$ set in Tab. 6.1) in blue and for the computation from Ref. [47, 55] ( $\mathcal{B}$ set in Tab. 6.1) in orange. The solid lines represent the central value of the $J$ -factors while the shaded regions correspond to the $1\sigma$ standard deviation.	57
267	Figure 7.1 Difference between spectral hypotheses from PPPC [44] and HDM [64]. Shown is the expected DM annihilation spectrum for $\chi\chi \rightarrow W^-W^+$ . Solid lines are spectral models with EW corrections from the PPPC. Dash-dot lines are spectral models from HDM. Red lines are models for $M_\chi = 1$ TeV. Blue lines represent models for $M_\chi = 100$ TeV.	62
272	Figure 7.2 Photon spectra for $\chi\chi \rightarrow \gamma\gamma$ (left) and $\chi\chi \rightarrow ZZ$ (right) after gaussian convolution of line features. Both spectra have $\delta$ -features at photon energies equal to the DM mass. Bluer lines are annihilation spectra with lower DM mass. Redder lines are spectra from larger DM mass. All Spectral models are sourced from the Heavy Dark Matter models [64]. Axes are drawn roughly according to the energy sensitivity of HAWC.	63
278	Figure 7.3 $\frac{dJ}{d\Omega}$ maps for Coma Berenices, Draco, Segue1, and Sextans. Columns are divided for the $\pm 1\sigma$ uncertainties in $dJ/d\Omega$ around the mean value from $\mathcal{LS}$ [65]. Origin is centered on the specific dwarf spheroidal galaxies (dSph). $\theta$ and $\phi$ axes are the angular separation from the center of the dwarf	64

282	Figure 7.4	Infographic on how jobs and DM computation was organized in Section 6.3. Jobs were built for each permutation of CHANS and SOURCES shown by the left block in the figure. Each job, which took on the order 2 hrs to compute, had the following work flow: 1. Import HAWC analysis software, 2 min to run. 2. Load HAWC count maps, 5 min to run. 3. Load HAWC energy and spatial resolutions, 4 min. 5. Load DM spatial source templates and spectral models, less than 1 s. 6. Perform likelihood fit on data and model, about 8 min per DM mass. 7. Write results to file, less than 1s. . . . .	66
290	Figure 7.5	Graphic of Gustafson parallel coding pattern. $f_s$ is the fraction of a program, in time, spent on serial computation. $f_p$ is the fraction of computing time that is parallelizable. $T_p$ is the total time for a parallel program to run. $T_1$ is the total time for a parallel program to run if only 1 processor is allocated. $P_N$ is the $N$ -th processor where it's row is the computation the processor performs. The Gustafson pattern is most similar to what is implemented for this analysis. Figure is pulled from [67]. . . . .	67
297	Figure 7.6	Task chart for one multi-threaded job developed for this project. Green blocks indicate a shared resource across the threads AND computation performed serially. Red blocks indicate functional parallel processing within each thread. 3 threads are represented here, yet many more can be employed during the full analysis. Jobs are defined by the SOURCE as these require unique maps to be loaded into the likelihood estimator. The $m_\chi$ , CHAN, and $\langle\sigma v\rangle$ variables are entered into the thread pool and allocated as evenly as possible across the threads. . . . .	69
305	Figure 7.7	HAWC upper limits at 95% confidence level on $\langle\sigma v\rangle$ versus DM mass for $\chi\chi \rightarrow b\bar{b}, t\bar{t}, u\bar{u}, d\bar{d}, s\bar{s}, c\bar{c}, gg, W^+W^-$ , and $hh$ . Limits are with $\mathcal{LS}$ $J$ - factors [65]. The solid line represents the observed combined limit. Dashed lines represent limits from individual dSphs. . . . .	72
309	Figure 7.8	HAWC upper limits at 95% confidence level on $\langle\sigma v\rangle$ versus DM mass for $\chi\chi \rightarrow \nu_e\bar{\nu}_e, \nu_\mu\bar{\nu}_\mu, \nu_\tau\bar{\nu}_\tau, e\bar{e}, \mu\bar{\mu}, \tau\bar{\tau}, \gamma\gamma$ and $ZZ$ . Limits use $\mathcal{LS}$ $J$ factors [65]. The solid line represents the observed combined limit. Dashed lines represent limits from individual dSphs. . . . .	73
313	Figure 7.9	HAWC TS values for best fit $\langle\sigma v\rangle$ versus $m_\chi$ for SM annihilation channels: $\chi\chi \rightarrow b\bar{b}, t\bar{t}, u\bar{u}, d\bar{d}, s\bar{s}, c\bar{c}, gg, W^+W^-$ , and $hh$ . Limits use $\mathcal{LS}$ $J$ factors. The solid black line shows the combined best fit TS values. The colored, dashed lines are the TS values from each dSph. . . . .	74
317	Figure 7.10	HAWC TS values for best fit $\langle\sigma v\rangle$ versus $m_\chi$ for SM annihilation channels: $\chi\chi \rightarrow \nu_e\bar{\nu}_e, \nu_\mu\bar{\nu}_\mu, \nu_\tau\bar{\nu}_\tau, e\bar{e}, \mu\bar{\mu}, \tau\bar{\tau}, \gamma\gamma$ and $ZZ$ . Limits use $\mathcal{LS}$ $J$ factors. The solid black line shows the combined best fit TS values. The colored, dashed lines are the TS values from each dSph. . . . .	75

321	Figure 7.11 TODO: fill this out . . . . .	76
322	Figure 7.12 TODO: show p <sub>1</sub> and m <sub>1</sub> limits around[NEEDS A SOURCE][FACT CHECK THIS] . . . . .	77
324	Figure 7.13 TODO: there will be 2[NEEDS A SOURCE][FACT CHECK THIS] . . . . .	78
325	Figure A.1 Sister figure to Figure 6.3. Sources in the first row from left to right: Bootes I, Canes Venatici I, II. In second row: Draco, Hercules, Leo I. In the first row: Leo II, Leo IV, Sextans. In the final row: Ursa Major I, Ursa Major II. . . . .	81
328	Figure B.1 Sister figure to Figure 7.2 for remaining SM primary annihilation channels studied for this thesis. These did not require any post generation smoothing and so are directly pulled from [64] with a binning scheme most helpful for a HAWC analysis. . . . .	82
332	Figure B.2 TODO: fill this out . . . . .	92
333	Figure B.3 TODO: fill this out . . . . .	93
334	Figure B.4 TODO: fill this out . . . . .	94

**LIST OF ABBREVIATIONS**

- 336 **MSU** Michigan State University  
337 **LANL** Los Alamos National Laboratory  
338 **DM** Dark Matter  
339 **SM** Standard Model  
340 **HAWC** High Altitude Water Cherenkov Observatory  
341 **dSph** Dwarf Spheroidal Galaxy

342

## **CHAPTER 1**

### **INTRODUCTION**

343 Is the text not rendering right? Ah ok it knows im basically drafting the doc still

## CHAPTER 2

344

### DARK MATTER IN THE COSMOS

345 **2.1 Introduction**

346 The dark matter problem can be summarized in part by the following thought experiment.

347 Let us say you are the teacher for an elementary school classroom. You take them on a field  
348 trip to your local science museum and among the exhibits is one for mass and weight. The exhibit  
349 has a gigantic scale, and you come up with a fun problem for your class.

350 You ask your class, "What is the total weight of the classroom? Give your best estimation to  
351 me in 30 minutes, and then we'll check your guess on the scale. If your guess is within 10% of the  
352 right answer, we will stop for ice cream on the way back."

353 The students are ecstatic to hear this, and they get to work. The solution is some variation of  
354 the following strategy. The students should give each other their weight or best guess if they do  
355 not know. Then, all they must do is add each student's weight and get a grand total for the class.

356 The measurement on the giant scale should show the true weight of the class. When comparing  
357 the measured weight to your estimation, multiply the measurement by  $1.0 \pm 0.1$  to get the  $\pm 10\%$   
358 tolerances for your estimation.

359 Two of your students, Sandra and Mario, return to you with a solution.

360 They say, "We weren't sure of everyone's weight. We used 65 lbs. for the people we didn't  
361 know and added everyone who does know. There are 30 of us, and we got 2,000 lbs.! That's a ton!"

362 You estimated 1,900 lbs. assuming the average weight of a student in your class was 60 lbs.  
363 So, you are pleased with Sandra's and Mario's answer. You instruct your students to all gather on  
364 the giant scale and read off the weight together. To all your surprise, the scale reads *10,000 lbs.*!  
365 10,000 is significantly more than a 10% error from 2,000. In fact, it is approximately 5 times more  
366 massive than either your or your students' estimates. You think to yourself and conclude there  
367 must be something wrong with the scale. You ask an employee to check the scale and verify it is  
368 well calibrated. They confirm that the scale is in working order. You weigh a couple of students  
369 individually to assess that the scale is well calibrated. Sandra weighs 59 lbs., and Mario weighs

370 62 lbs., typical weights for their age. You then weigh each student individually and see that their  
371 weights individually do not deviate greatly from 60 lbs. So, where does all the extra weight come  
372 from?

373 This thought experiment serves as an analogy to the Dark Matter problem. The important  
374 substitution to make however is to replace the students with stars and the classroom with a galaxy,  
375 say the Milky Way. Individually the mass of stars is well measured and defined with the Sun as our  
376 nearest test case. However, when we set out to measure the mass of a collection of stars as large as  
377 galaxies, our well-motivated estimation is wildly incorrect. There simply is no way to account for  
378 this discrepancy except without some unseen, or dark, contribution to mass and matter in galaxies.  
379 I set out in my thesis to narrow the possibilities of what this Dark Matter could be.

380 This chapter is organized like the following... **TODO: Text should look like ... Chapter x has**  
381 **blah blah blah.**

382 **2.2 Dark Matter Basics**

383 Presently, a more compelling theory of cosmology that includes Dark Matter (DM) in order  
384 to explain a variety of observations is  $\Lambda$  Cold Dark Matter, or  $\Lambda$ CDM. I present the evidence  
385 supporting  $\Lambda$ CDM in Section 2.3 yet discuss the conclusions of the  $\Lambda$ CDM model here. According  
386 to  $\Lambda$ CDM fit to observations on the Cosmic Microwave Background (CMB), DM is 26.8% of the  
387 universe's current energy budget. Baryonic matter, stuff like atoms, gas, and stars, contributes to  
388 4.9% of the universe's current energy budget [1, 2, 3].

389 DM is dark; it does not interact readily with light at any wavelength. DM also does not interact  
390 noticeably with the other standard model forces (Strong and Weak) at a rate that is readily observed  
391 [3]. DM is cold, which is to say that the average velocity of DM is below relativistic speeds [1].  
392 'Hot' DM would not likely manifest the dense structures we observe like galaxies, and instead  
393 would produce much more diffuse galaxies than what is observed [3, 1]. DM is old; it played a  
394 critical role in the formation of the universe and the structures within it [1, 2].

395 Observations of DM have so far been only gravitational. The parameter space available to what  
396 DM could be therefore is extremely broad. The broad DM parameter space is iteratively tested in

397 DM searches by supposing a hypothesis that has not yet been ruled out and performing observations  
398 to test them. When the observations yield a null result, the parameter space is constrained further.  
399 I present some approaches for DM searches in Section 2.4.

400 **2.3 Evidence for Dark Matter**

401 Dark Matter (DM) has been a looming problem in physics for almost 100 years. Anomalies  
402 have been observed by astrophysicists in galactic dynamics as early as 1933 when Fritz Zwicky  
403 noticed unusually large velocity dispersion in the Coma cluster. Zwicky's measurement was the  
404 first recorded to use the Virial theorem to measure the mass fraction of visible and invisible matter  
405 in celestial bodies [4]. From Zwicky in [5], "*If this would be confirmed, we would get the surprising*  
406 *result that dark matter is present in much greater amount than luminous matter.*" Zwicky's and  
407 others' observation did not instigate a crisis in astrophysics because the measurements did not  
408 entirely conflict with their understanding of galaxies [4]. In 1978, Rubin, Ford, and Norbert  
409 measured rotation curves for ten spiral galaxies [6]. Rubin et al.'s 1978 publication presented a  
410 major challenge to the conventional understanding of galaxies that could no longer be dismissed by  
411 measurement uncertainties. Evidence has been mounting ever since for this exotic form of matter.  
412 The following subsections provide three compelling pieces of evidence in support of the existence  
413 of DM.

414 **2.3.1 First Clues: Stellar Velocities**

415 Zwicky, and later Rubin, measured the stellar velocities of various galaxies to estimate their  
416 virial mass. The Virial Theorem upon which these observations are interpreted is written as

$$2T + V = 0. \quad (2.1)$$

417 Where  $T$  is the kinetic energy and  $V$  is the potential energy in a self-gravitating system. The  
418 classical Newton's law of gravity from stars and gas was used for gravitational potential modeled in  
419 the observed galaxies:

$$V = -\frac{1}{2} \sum_i \sum_{j \neq i} \frac{m_i m_j}{r_{ij}}. \quad (2.2)$$

420 Zwicky et al. measured just the velocities of stars apparent in optical wavelengths [5]. Rubin et al.  
 421 added by measuring the velocity of the hydrogen gas via the 21 cm emission line of Hydrogen [6].  
 422 The velocities of the stars and gas are used to infer the total mass of galaxies and galaxy clusters  
 423 via Equation (2.1). An inferred mass is obtained from the luminosity of the selected sources. The  
 424 two inferences are compared to each other as a luminosity to mass ratio which typically yielded [1]

$$\frac{M}{L} \sim 400 \frac{M_{\odot}}{L_{\odot}} \quad (2.3)$$

425  $M_{\odot}$  and  $L_{\odot}$  referring to stellar mass and stellar luminosity, respectively. These ratios clearly indicate  
 426 a discrepancy in apparent light and mass from stars and gas and their velocities.

427 Rubin et al. [6] demonstrated that the discrepancy was unlikely to be an underestimation of  
 428 the mass of the stars and gas. The inferred "dark" mass was up to 5 times more than the luminous  
 429 mass. This dark mass also needed to extend well beyond the extent of the luminous matter.

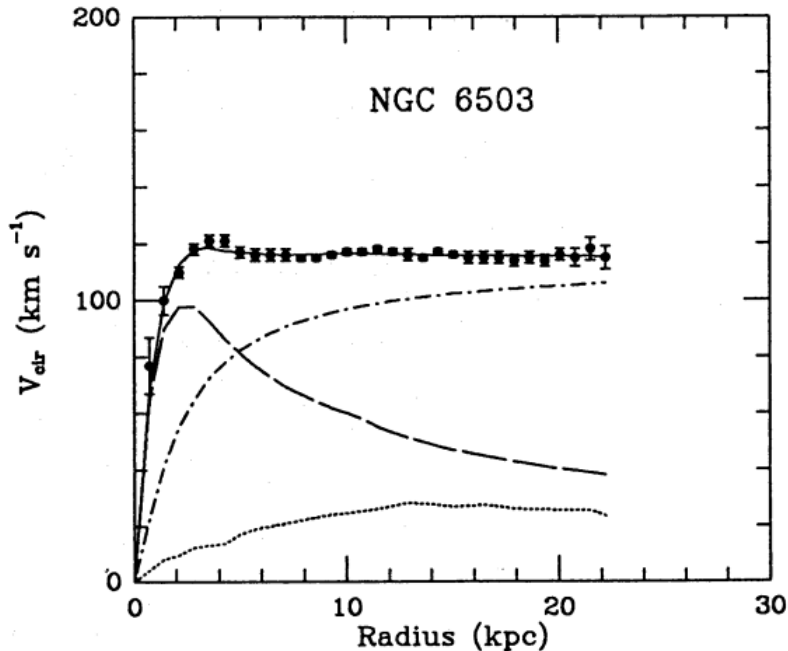


Figure 2.1 Rotation curve fit to NGC 6503 from [7]. Dashed line is the contribution from visible matter. Dotted curves are from gas. Dash-dot curves are from dark matter (DM). Solid line is the composite contribution from all matter and DM sources. Data are indicated with bold dots with error bars. Data agree strongly with a matter + DM composite prediction.

430 Figure 2.1 features one of many rotation curves plotted from the stellar velocities within galaxies.

431 The measured rotation curves mostly feature a flattening of velocities at higher radius which is not  
432 expected if the gravity was only coming from gas and luminous matter. The extension of the  
433 flat velocity region also indicates that the DM is distributed far from the center of the galaxy.  
434 Modern velocity measurements include significantly larger objects, galactic clusters, and smaller  
435 objects, dwarf galaxies. Yet, measurements along this regime are leveraging the Virial theorem  
436 with Newtonian potential energies. We know Newtonian gravity is not a comprehensive description  
437 of gravity. New observational techniques have been developed since 1978, and those are discussed  
438 in the following sections.

439 **2.3.2 Evidence for Dark Matter: Gravitational Lensing**

440 Modern evidence for dark matter comes from new avenues beyond stellar velocities. Grav-  
441 itational lensing from DM is a new channel from general relativity. General relativity predicts  
442 aberrations in light caused by massive objects. In recent decades we have been able to measure the  
443 lensing effects from compact objects and DM halos. Figure 2.2 shows how different massive ob-  
444 jects change the final image of a faraway galaxy resulting from gravitational lensing. Gravitational  
445 lensing developed our understanding of dark matter in two important ways.

446 Gravitational lensing provides additional compelling evidence for DM. The observation of two  
447 merging galactic clusters in 2006, shown in Figure 2.3, provided a compelling argument for DM  
448 outside the Standard Model. These clusters merged recently in astrophysical time scales. Galaxies  
449 and star cluster have mostly passed by each other as the likelihood of their collision is low. Therefore,  
450 these massive objects will mostly track the highest mass, dark and/or baryonic, density. Yet, the  
451 intergalactic gas is responsible for the majority of the baryonic mass in the systems [4]. These gas  
452 bodies will not phase through and will heat up as they collide together. The hot gas is located via  
453 x-ray emission from the cluster. Two observations of the clusters were performed independently of  
454 each other.

455 The first was the lensing of light around the galaxies due to their gravitational influences.  
456 When celestial bodies are large enough, the gravity they exert bends space and time itself. The  
457 warped space-time lenses light and will deflect in an analogous way to how glass lenses will bend

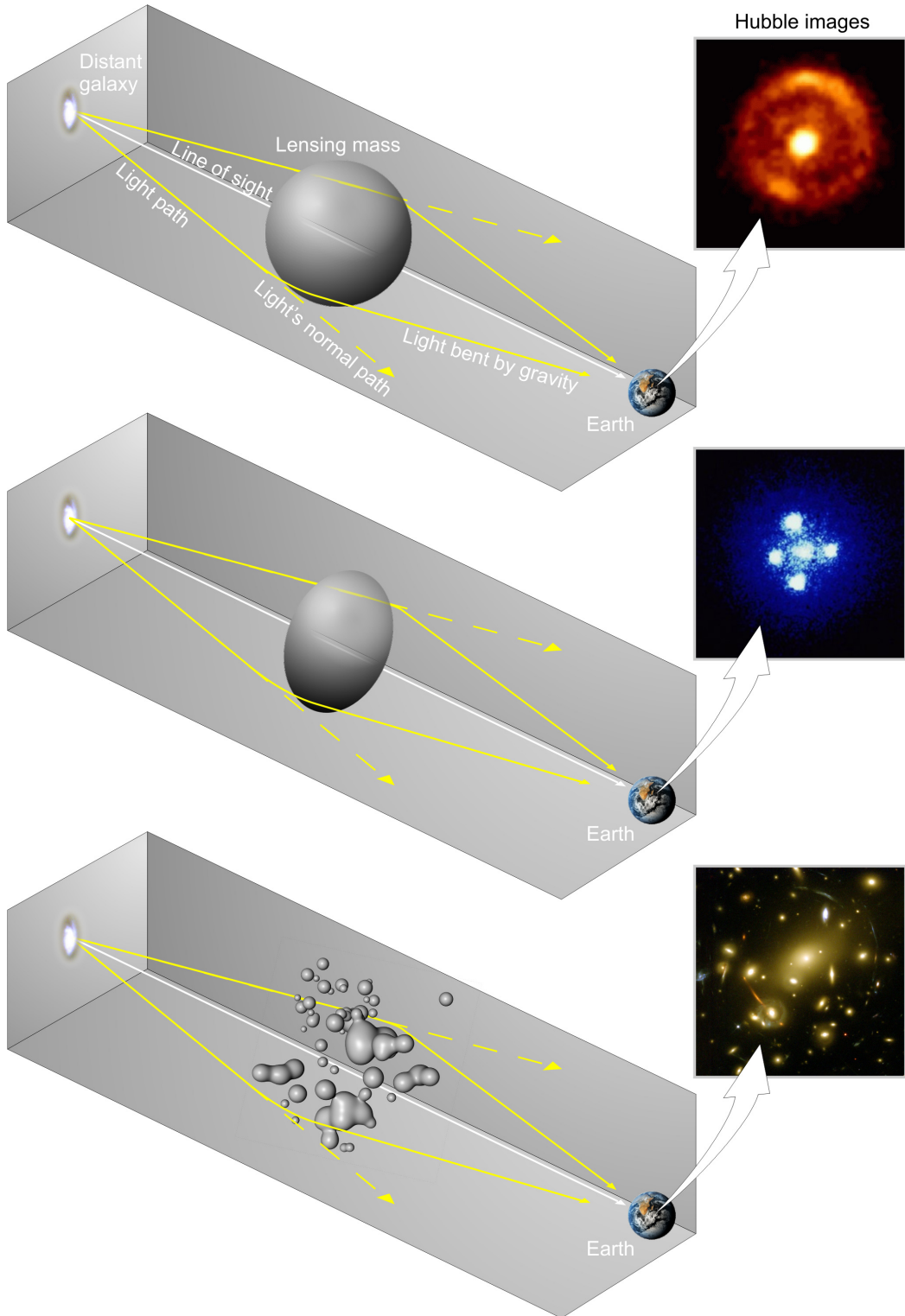


Figure 2.2 Light from distant galaxy is bent in unique ways depending on the distribution of mass between the galaxy and Earth. Yellow dashed lines indicate where the light would have gone if the matter were not present [8].

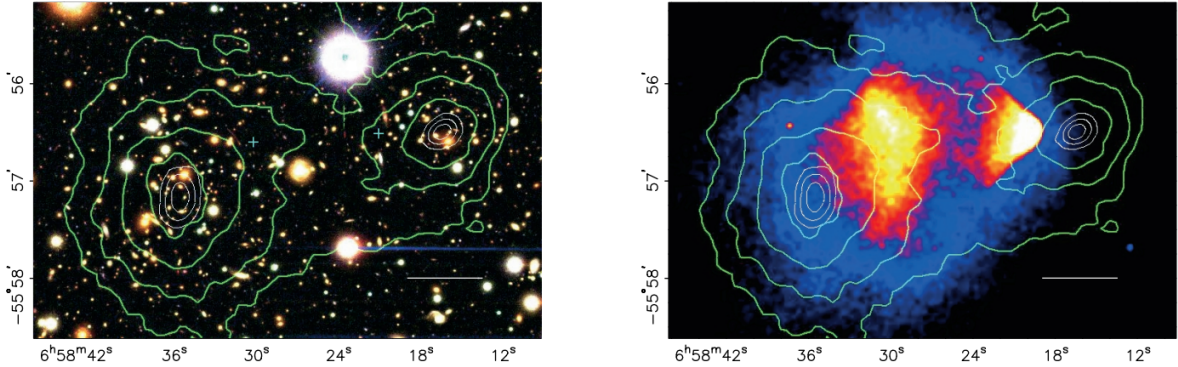


Figure 2.3 (left) Optical image of galactic cluster 1E0657-558. (right) X-ray image of the cluster with redder meaning hotter and higher baryon density. (both) Green contours are reconstruction of gravity contours from weak lensing. White rings are the best fit mass maxima at 68.3%, 95.5%, and 99.7% confidence. The matter maxima of the clusters are clearly separated from x-ray maxima. [9]

458 light, see Figure 2.2. With a sufficient understanding of light sources behind a massive object, we  
 459 can reconstruct the contours of the gravitational lenses. The gradient of the contours shown in  
 460 Figure 2.3 then indicates how dense the matter is and where it is.

461 The x-ray emission can then be observed from the clusters. Since these galaxies are mostly gas  
 462 and are merging, then the gas should be getting hotter. If they are merging, the x-ray emissions  
 463 should be the strongest where the gas is mostly moving through each other. Hence, X-ray emission  
 464 maps out where the gas is in the merging galaxy cluster.

465 The lensing and x-ray observations were done on the Bullet cluster featured on Figure 2.3.  
 466 The x-ray emissions do not align with the gravitational contours from lensing. The incongruence  
 467 in mass density and baryon density suggests that there is a lot of matter somewhere that does  
 468 not interact with light. Moreover, this dark matter cannot be baryonic [9]. The Bullet Cluster  
 469 measurement did not really tell us what DM is exactly, but it did give the clue that DM also does  
 470 not interact with itself very strongly. If DM did interact strongly with itself, then it would have been  
 471 more aligned with the x-ray emission [9]. There have been follow-up studies of galaxy clusters with  
 472 similar results. The Bullet Cluster and others like it provide a persuasive case against something  
 473 possibly amiss in our gravitational theories.

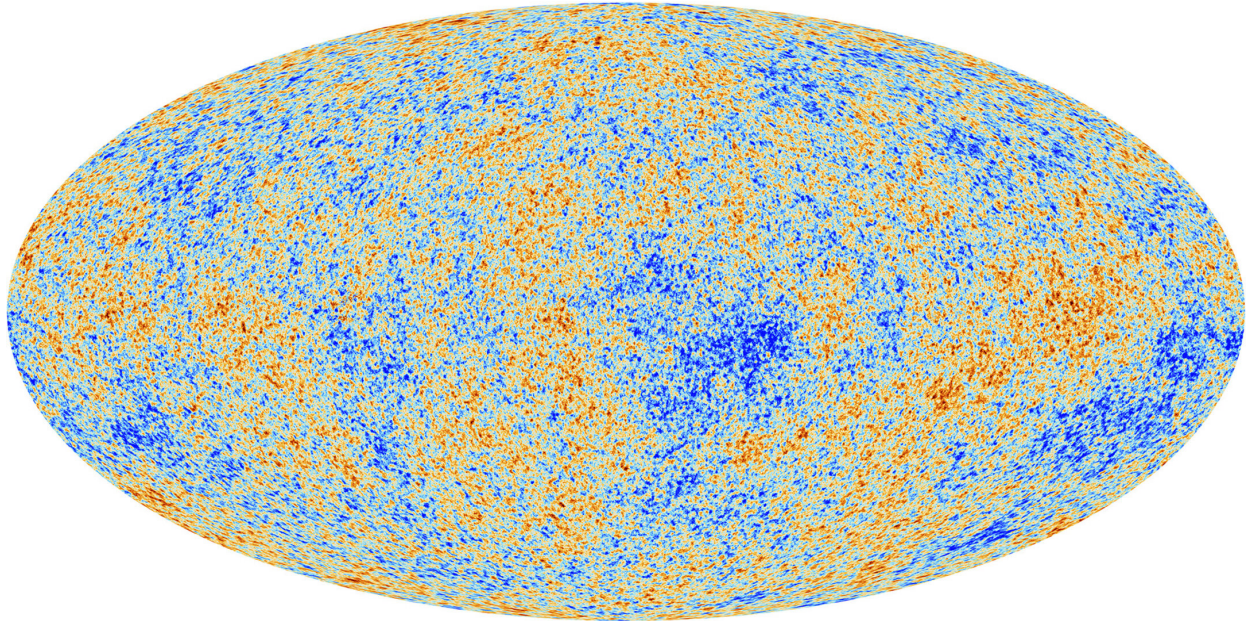


Figure 2.4 Plank CMB sky. Sky map features small variations in temperature in primordial light. These anisotropies are used to make inferences about the universe’s energy budget and developmental history. [10]

474     **2.3.3 Evidence for Dark Matter: Cosmic Microwave Background**

475       The Cosmic Microwave Background (CMB) is the primordial light from the early universe  
476       when Hydrogen atoms formed from the free electron and proton soup in the early universe. The  
477       CMB is the earliest light we can observe; released when the universe was about 380,000 years old.  
478       Then we look at how the simulated universes look like compared to what we see. Figure 2.4 is the  
479       most recent CMB image from the Plank satellite after subtracting the average value and masking the  
480       galactic plane [10]. Redder regions indicate a slightly hotter region in the CMB, and blue indicates  
481       colder. The intensity variations are on the order of 1 in 1000 with respect to the average value.

482       The Cosmic Microwave Background shows that the universe had DM in it from an incredibly  
483       early stage. To measure the DM, Dark Energy, and matter fractions of the universe from the CMB,  
484       the image is analyzed into a power spectrum, which shows the amplitude of the fluctuations as  
485       a function of spherical multipole moments.  $\Lambda$ CDM provides the best fit to the power spectra of  
486       the CMB as shown in Figure 2.5. The CMB power spectrum is quite sensitive to the fraction  
487       of each energy contribution in the early universe. Low  $l$  modes are dominated by variations  
488       in gravitational potential. Intermediate  $l$  emerge from oscillations in photon-baryon fluid from

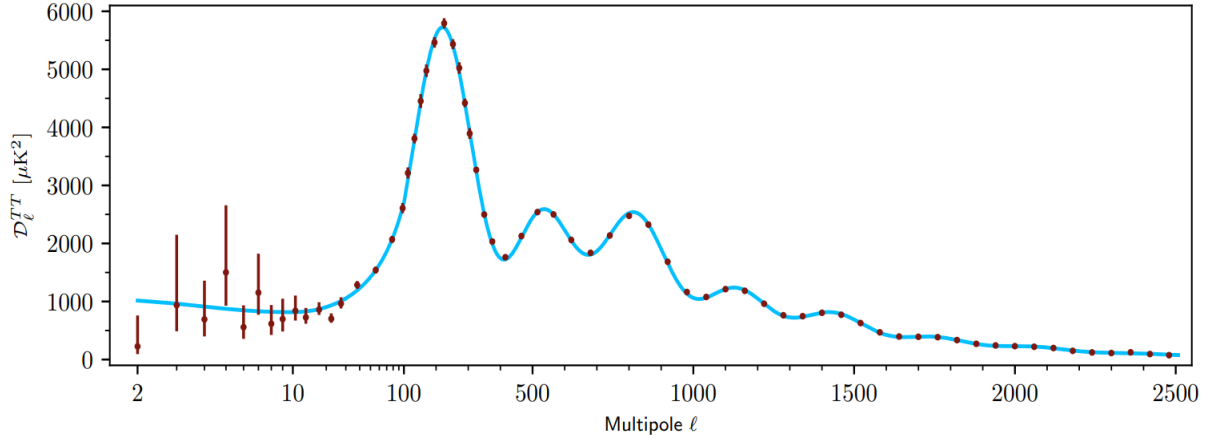


Figure 2.5 Observed Cosmic Microwave Background power spectrum as a function of multipole moment from Plank [10]. Blue line is best fit model from  $\Lambda$ CDM. Red points and lines are data and error, respectively.

489 competing baryon pressures and gravity. High  $l$  is a damped region from the diffusion of photons  
 490 during electron-proton recombination. [1]

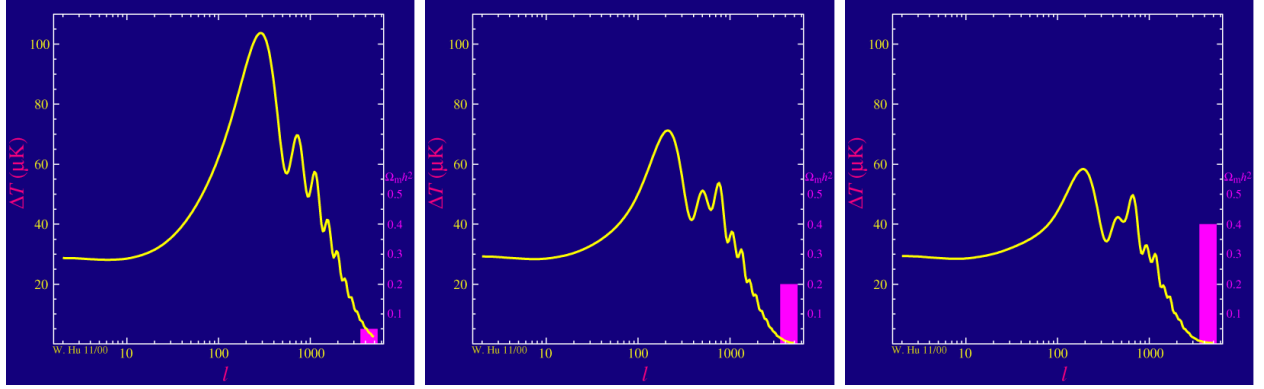


Figure 2.6 Predicted power spectra of CMB for different  $\Omega_m h^2$  values for fixed baryon density from [11]. (left) Low  $\Omega_m h^2$  increases the prominence of first and second peaks. (middle)  $\Omega_m h^2$  is most similar to the observed power spectrum. The second and third peaks are similar in height. (right)  $\Omega_m h^2$  is large which suppresses the first peak and raises the prominence of the third peak.

491 The harmonics would look quite different for a universe with less DM. Figure 2.6 demonstrates  
 492 the effect  $\Omega_m h^2$  has on the expected power spectrum for fixed baryon matter density. [11] Sweeping  
 493  $\Omega_m h^2$  in this way clearly shows the effect dark matter has on the CMB power spectrum. The  
 494 observations fit well with the  $\Lambda$ CDM model, and the derived fractions are as follows. The matter  
 495 fraction:  $\Omega_m = 0.3153$ ; and the baryon fraction:  $\Omega_b = 0.04936$  [10]. Plank's observations also  
 496 provide a measure of the Hubble constant,  $H_0$ .  $H_0$  especially has seen a growing tension in the

497 past decade that continues to deepened with observations from instruments like the James Webb  
498 Telescope [12, 13]. As Hubble tensions deepen, we may find that perhaps  $\Lambda$ **CDM**, despite its  
499 successes, is missing some critical physics.

500 Overall, the Newtonian motion of stars in galaxies, weak lensing from galactic clusters, and  
501 power spectra from primordial light form a compelling body of research in favor of dark matter.  
502 It takes another leap of theory and experimentation to make observations of DM that are non-  
503 gravitational in nature. In Section 2.3, the evidence for DM implies strongly that the DM is matter  
504 and not a lost parameter in the gravitational fields between massive objects. Finally, if we take one  
505 axiom: that this matter has quantum behavior, such as being described by some Bohr wavelength  
506 and abiding by some fermion or boson statistics; then we arrive at particle dark matter. One particle  
507 DM hypothesis is the Weakly Interacting Massive Particle (WIMP). This DM candidate theory is  
508 discussed further in the next section and is the focus of this thesis.

## 509 2.4 Searching for Dark Matter: Particle DM

510 Section 2.4 shows the Standard Model of particle physics and is currently the most accurate  
511 model for the dynamics of fundamental particles like electrons and photons. The current status  
512 of the SM does not have a viable DM candidate. When looking at the standard model, we can  
513 immediately exclude any charged particle because charged particles interact strongly with light.  
514 Specifically, this will rule out the following charged, fundamental particles:  $e, \mu, \tau, W, u, d, s, c, t, b$   
515 and their corresponding antiparticles. Recalling from Section 2.2 that DM must be long-lived and  
516 stable over the age of the universe which excludes all SM particles with decay half-lives at or shorter  
517 than the age of the universe. The lifetime constraint additionally eliminates the  $Z$  and  $H$  bosons.  
518 Finally, the candidate DM needs to be somewhat massive. Recall from Section 2.2 that DM is cold  
519 or not relativistic through the universe. This eliminates the remaining SM particles:  $\nu_{e,\mu,\tau}, g, \gamma$  as  
520 DM candidates. Because there are no DM candidates within the SM, the DM problem strongly  
521 hints to physics beyond the SM (BSM).

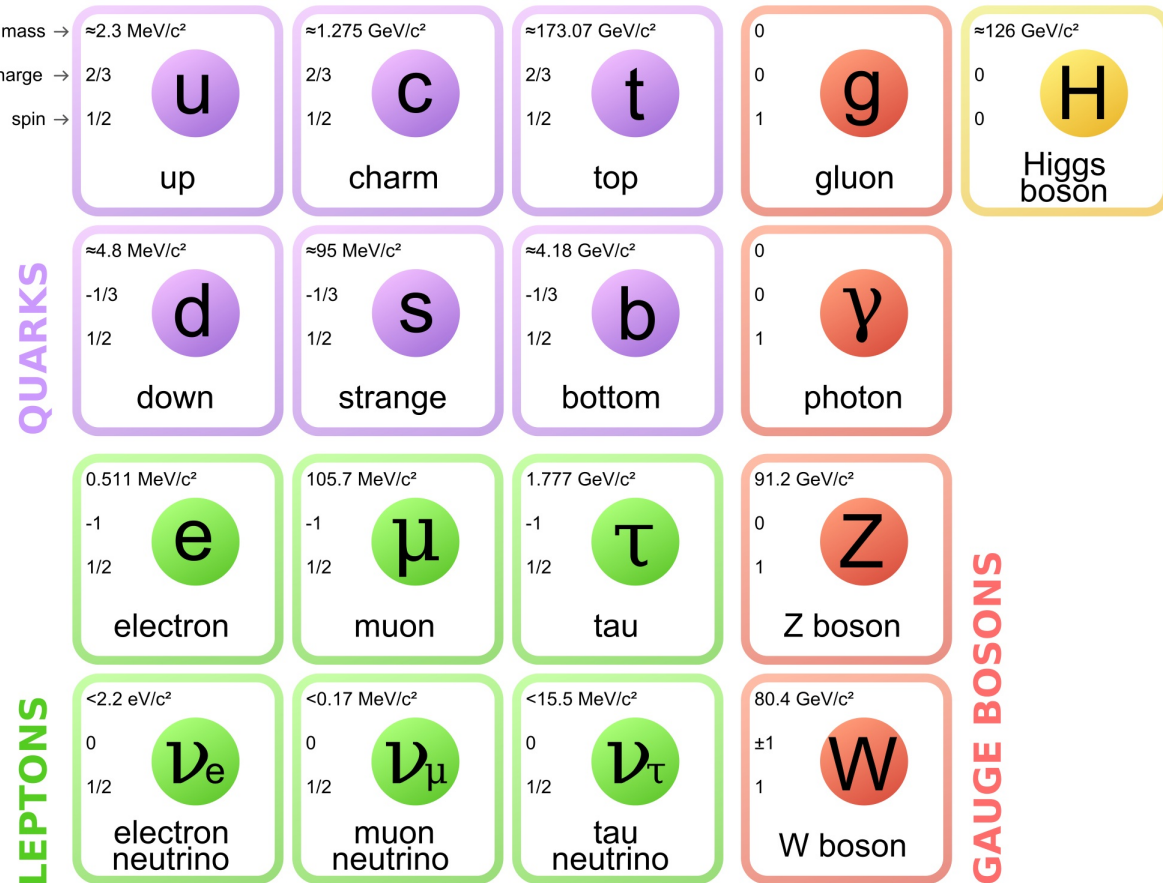


Figure 2.7 The Standard Model (SM) of particle physics. Figure taken from <http://www.quantumdiaries.org/2014/03/14/the-standard-model-a-beautiful-but-flawed-theory/>

### 522 2.4.1 Shake it, Break it, Make it

523 When considering DM that couples in some way with the SM, the interactions are roughly  
 524 demonstrated by interaction demonstrated in Figure 2.8. The figure is a simplified Feynman  
 525 diagram where the arrow of time represents the interaction modes of: **Shake it, Break it, Make it.**

526 **Shake it** refers to the direct detection of dark matter. Direct detection interactions start with  
 527 a free DM particle and an SM particle. The DM and SM interact via elastic or inelastic collision  
 528 and recoil away from each other. The DM remains in the dark sector and imparts some momentum  
 529 onto the SM particle. The hope is that the momentum imparted onto the SM particle is sufficiently  
 530 high enough to pick up with extremely sensitive instruments. Because we cannot create the DM in  
 531 the lab, a direct detection experiment must wait until DM is incident on the detector. Most direct  
 532 detection experiments are therefore placed in low-background environments with inert detection

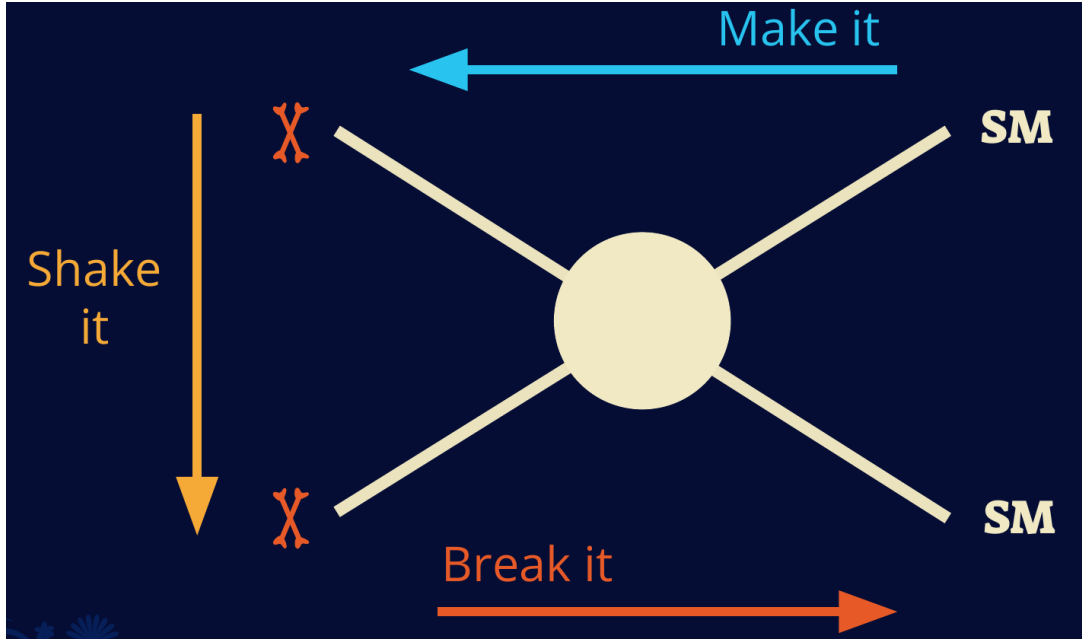


Figure 2.8 Simplified Feynman diagram demonstrating different ways DM can interact with SM particles. The 'X's refer to the DM particles whereas the SM refer to fundamental particles in the SM. The large circle in the center indicates the vertex of interaction and is purposely left vague. The colored arrows refer to different directions of time as well as their respective labels. The arrows indicate the initial and final state of the DM -SM interaction in time.

533 media like the noble gas Xenon. [14]

534 **Make it** refers to the production of DM from SM initial states. The experiment starts with  
 535 particles in the SM. These SM particles are accelerated to incredibly high energies and then collide  
 536 with each other. In the confluence of energy, DM hopefully emerges as a byproduct of the SM  
 537 annihilation. Often it is the collider experiments that are energetic enough to hypothetically produce  
 538 DM. These experiments include the world-wide collaborations ATLAS and CMS at CERN where  
 539 proton collide together at extreme energies. The DM searches, however, are complex. DM likely  
 540 does not interact with the detectors and lives long enough to escape the detection apparatus of  
 541 CERN's colliders. This means any DM production experiment searches for an excess of events  
 542 with missing momentum or energy in the events. An example event with missing transverse  
 543 momentum is shown in Figure 2.9. The missing momentum with no particle tracks implies a  
 544 neutral particle carried the energy out of the detector. However, there are other neutral particles  
 545 in the SM, like neutrons or neutrinos, so any analysis has to account for SM signatures of missing

546 momentum. [15]

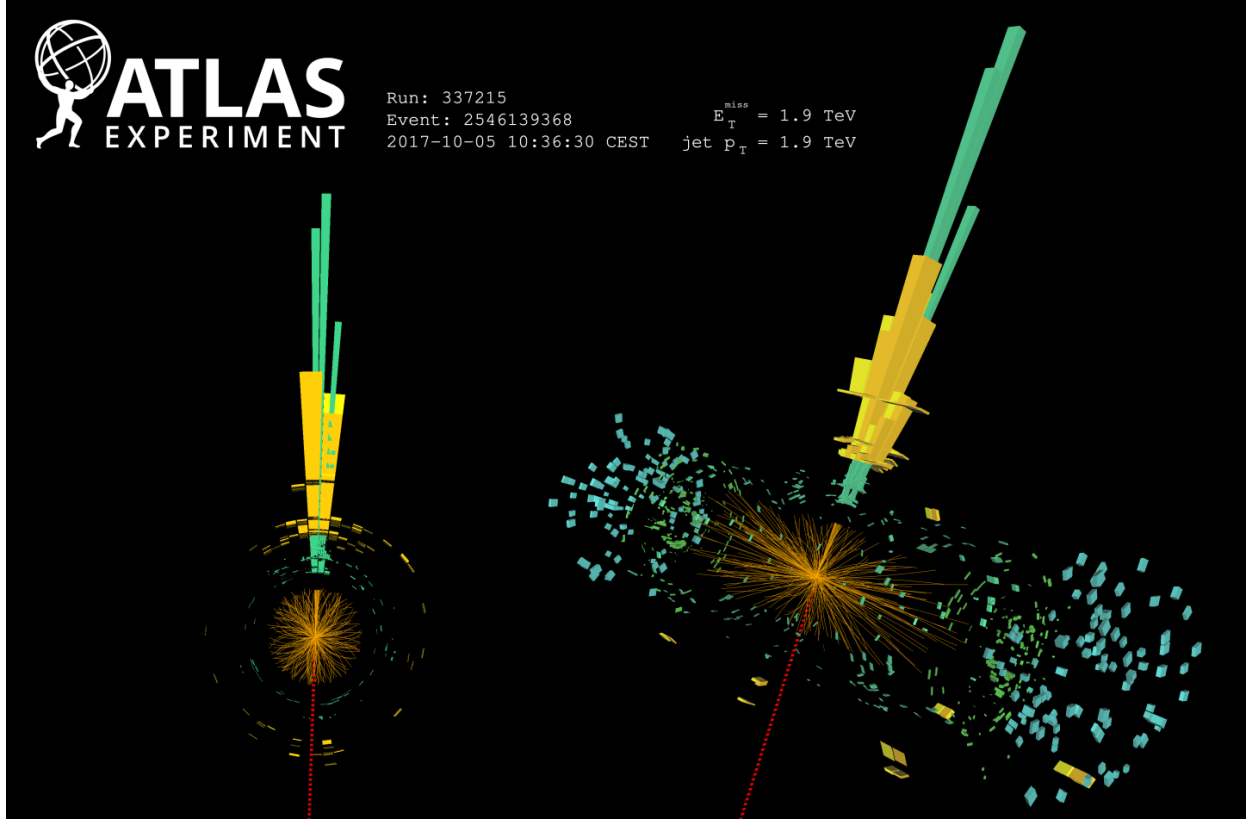


Figure 2.9 A single jet event in ATLAS detector from 2017 [16]. Jet momentum was observed to be 1.9 TeV. Missing transverse momentum was observed to be 1.9 TeV compared to the initial transverse momentum of the event was 0. Implied MET is traced by a red dashed line in event display.

#### 547 2.4.2 Break it: Standard Model Signatures of Dark Matter through Indirect Searches

548 **Break it** refers to the creation of SM particles from the dark sector, and it is the primary focus  
549 of this thesis. The interaction begins with DM or in the dark sector. The hypothesis is that this  
550 DM will either annihilate with itself or decay and produce an SM byproduct. This method is  
551 often referred to as the Indirect Detection of DM because we have no lab to directly control or  
552 manipulate the DM. Therefore, most indirect DM searches are performed using observations of  
553 known DM densities among the astrophysical sources. The strength is that we have the whole of the  
554 universe and its 13.6-billion-year lifespan to use as a detector and particle accelerator. Additionally,  
555 locations of dark matter are well cataloged since it was astrophysical observations that presented

556 the problem of DM in the first place.

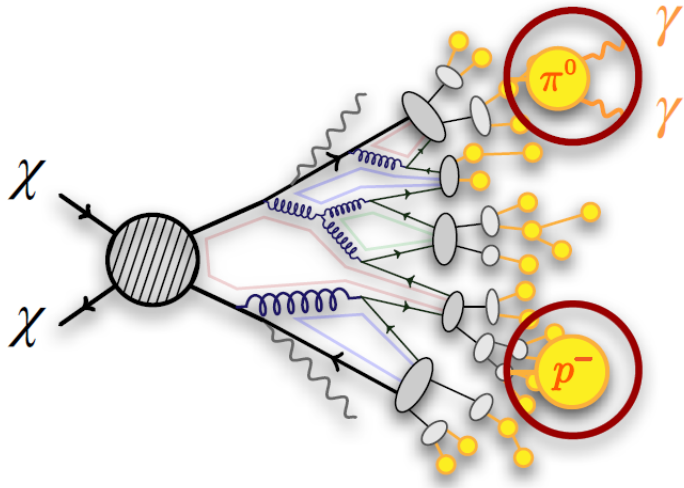


Figure 2.10 More detailed pseudo-Feynman diagram of particle cascade from dark matter annihilation into 2 quarks. The quarks hadronize and down to stable particles like  $\gamma$  or the anti-proton ( $p^-$ ). Diagram pulled from ICRC 2021 presentation on DM annihilation search [17].

557 However, anything can happen in the universe. There are many difficult to deconvolve back-  
558 grounds when searching for DM. One prominent example is the galactic center. We know the  
559 galactic center has a large DM content because of stellar kinematics in our Milky Way and DM halo  
560 simulations. Yet, any signal from the galactic center is challenging to parse apart from the extreme  
561 environment of our supermassive black hole, unresolved sources, and diffuse emission from the  
562 interstellar medium [18]. Despite the challenges, any DM model that yields evidence in the other  
563 two observation methods, **Shake it or Make it** must be corroborated with indirect observations of  
564 the known DM sources. Without corroborating evidence, DM observation in the lab is hard-pressed  
565 to demonstrate that it is the model contributing to the DM seen at the universal scale.

566 In the case of WIMP DM, signals are described in terms of primary SM particles produced  
567 from DM decay or annihilation. The SM initial state particles are then simulated down to stable  
568 final states such as the  $\gamma$ ,  $\nu$ ,  $p$ , or  $e$  which can traverse galactic lengths to reach Earth.

569 Figure 2.10 shows the quagmire of SM particles that emerges from SM initial states that are not  
570 stable [17]. There are many SM particles with varying energies that can be produced in such an

571 interaction. For any arbitrary DM source and stable SM particle, the SM flux from DM annihilating  
 572 to a neutral particle in the SM,  $\phi$ , from a region in the sky is described by the following.

$$\frac{d\Phi_\phi}{dE_\phi} = \frac{\langle\sigma v\rangle}{8\pi m_\chi^2} \frac{dN_\phi}{dE_\phi} \times \int_{\text{source}} d\Omega \int_{l.o.s} \rho_\chi^2 dl(r, \theta') \quad (2.4)$$

573 In Equation (6.1),  $\langle\sigma v\rangle$  is the velocity-weighted annihilation cross-section of DM to the SM.  $m_\chi$   
 574 refers to the mass of DM, noted with Greek letter  $\chi$ .  $\frac{dN_\phi}{dE_\phi}$  is the N particle flux weighted by the  
 575 particle energy. An example is provided in Figure 2.11 for the  $\gamma$  final state. The integrated terms  
 576 are performed over the solid angle,  $d\Omega$ , and line of sight, l.o.s.  $\rho$  is the density of DM for a  
 577 location  $(r, \theta')$  in the sky. The terms left of the '×' are often referred to as the particle physics  
 578 component. The terms on the right are referred to as the astrophysical component. For decaying  
 579 DM, the equation changes to...

$$\frac{d\Phi_\phi}{dE_\phi} = \frac{1}{4\pi\tau m_\chi} \frac{dN_\phi}{dE_\phi} \times \int_{\text{source}} d\Omega \int_{l.o.s} \rho_\chi dl(r, \theta') \quad (2.5)$$

580 In Equation (7.1),  $\tau$  is the decay lifetime of the DM. Just as in Equation (6.1), the left and right  
 581 terms are the particle physics and the astrophysical components respectively. The integrated  
 582 astrophysical component of Equation (6.1) is often called the J-Factor. Whereas the integrated  
 583 astrophysical component of Equation (7.1) is often called the D-Factor.

584     Exact DM  $\text{DM} \rightarrow \text{SM SM}$  branching ratios are not known, so it is usually assumed to go 100%  
 585 into an SM particle/anti-particle. Additionally, when a DM annihilation or decay produces one of  
 586 the neutral, long-lived SM particles ( $\nu$  or  $\gamma$ ), the particle is traced back to a DM source. For DM  
 587 above GeV energies, there are very few SM processes that can produce particles with such a high  
 588 energy. Seeing such a signal would almost certainly be an indication of the presence of dark matter.  
 589 Fortunately, the universe provides us with the largest volume and lifetime ever for a particle physics  
 590 experiment.

## 591 2.5 Sources for Indirect Dark Matter Searches

592     The first detection of DM relied on optical observations. Since then, we have developed new  
 593 techniques to find DM dense regions. As described in Section 2.3.1, many DM dense regions were  
 594 through observing galactic rotation curves. Our Milky Way galaxy is among DM dense regions

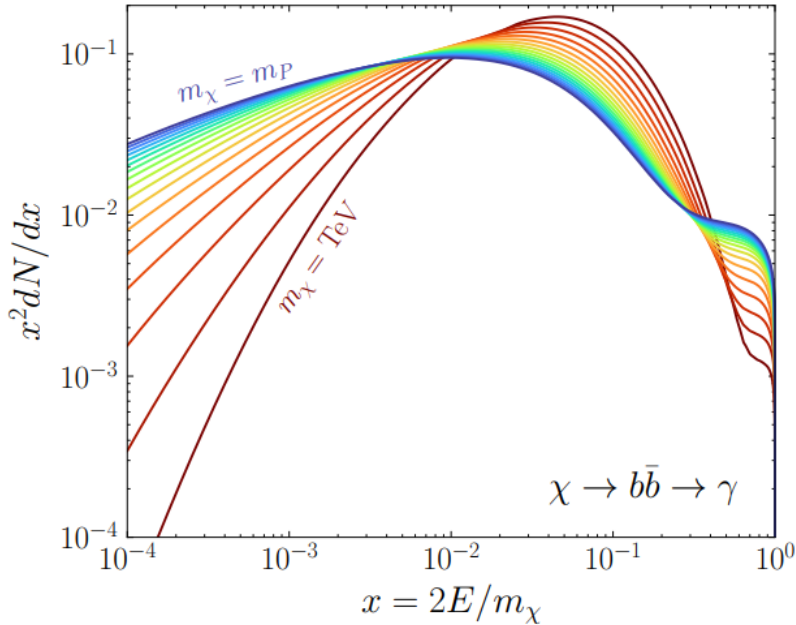


Figure 2.11 Dark Matter (DM) decay spectrum for  $b\bar{b}$  initial state and  $\gamma$  final state. Redder spectra are for larger DM masses. Bluer spectra are light DM masses.  $x$  is a unitless factor defined as the ratio of the mass of DM,  $m_\chi$ , and the final state particle energy  $E_\gamma$ . Figure from [19].

discovered, and it is the largest nearby DM dense region to look at. Additionally, the DM halo surrounding the Milky Way is clumpy [18]. There are regions in the DM halo of the Milky Way that have more DM than others that have captured gas over time. These sub-halos were dense enough collapse gas and form stars. These apparent sub galaxies are known as dwarf spheroidal galaxies and are the main sources studied in this thesis. Each source type comes with different trade-offs. Galactic Center studies will be very sensitive to the assumed distribution of DM. The central DM density can vary substantially as demonstrated in Figure 2.12. At distances close to the center of the galaxy, or small  $r$ , the differences in DM densities can be 3-4 orders of magnitude. Searches toward the galactic center will therefore be quite sensitive to the assumed DM distribution.

Searches toward Dwarf Spheroidal Galaxies (dSph's) suffer from uncertainties in the DM density less than the galactic center studies. This is mostly from their diminutive size being smaller than the angular resolution of most  $\gamma$ -ray observatories [18]. The DM content dSph's are typically determined with the Virial theorem, Equation (2.1), and are usually majority DM [18] in mass. DSph's tend to be ideal sources to look at for DM searches. Their environments are quiet with little

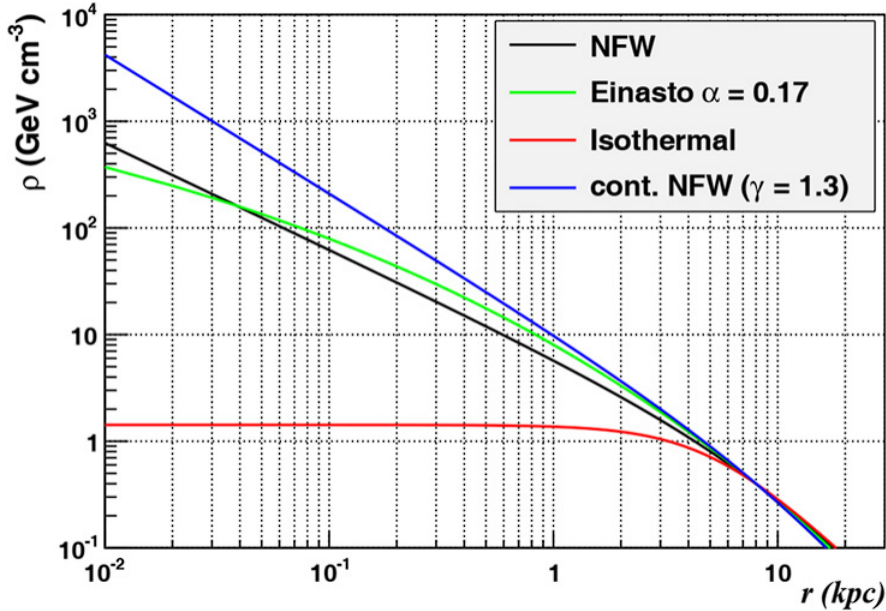


Figure 2.12 Different dark matter density profiles compared. Some models produce exceptionally large densities at small  $r$  [20].

609 astrophysical background. Unlike the galactic center, the most active components of dSph's are the  
 610 stars within them versus a violent accretion disc around a black hole. All this together means that  
 611 dSph's are among the best sources to look at for indirect DM searches. dSph's are the targets of  
 612 focus for this thesis.

## 613 2.6 Multi-Messenger Dark Matter

614 Astrophysics entered a new phase in the past few decades that leverages our increasing sensitivity  
 615 to SM channels and general relativity (GR). Up until the 21st century, astrophysical observations  
 616 were performed with photons ( $\gamma$ ) only. Astrophysics with this 'messenger' is fairly mature now.  
 617 Novel observations of the universe have since only adjusted the sensitivity of the wavelength of  
 618 light that is observed except at MeV energies. Gems like the CMB [10], and more have ultimately  
 619 been observations of different wavelengths of light. Multi-messenger astrophysics proposes using  
 620 other SM particles such the  $p^{+-}$ , or  $\nu$  or gravitation waves predicted by general relativity.

621 The experiment LIGO had a revolutionary discovery in 2016 with the first detection of a binary  
 622 black hole merger [21]. This opened the collective imagination to observing the universe through  
 623 gravitational waves. There has also been a surge of interest in the neutrino ( $\nu$ ) sector. IceCube

624 demonstrated that we are sensitive to neutrinos in regions that correlate with significant photon  
 625 emission like the galactic plane [22]. Neutrinos, like gravitational waves and light, travel mostly  
 626 unimpeded from their source to our observatories. This makes pointing to the originating source  
 627 of these messengers much easier than it is for cosmic rays which are deflected from their source by  
 628 magnetic fields.

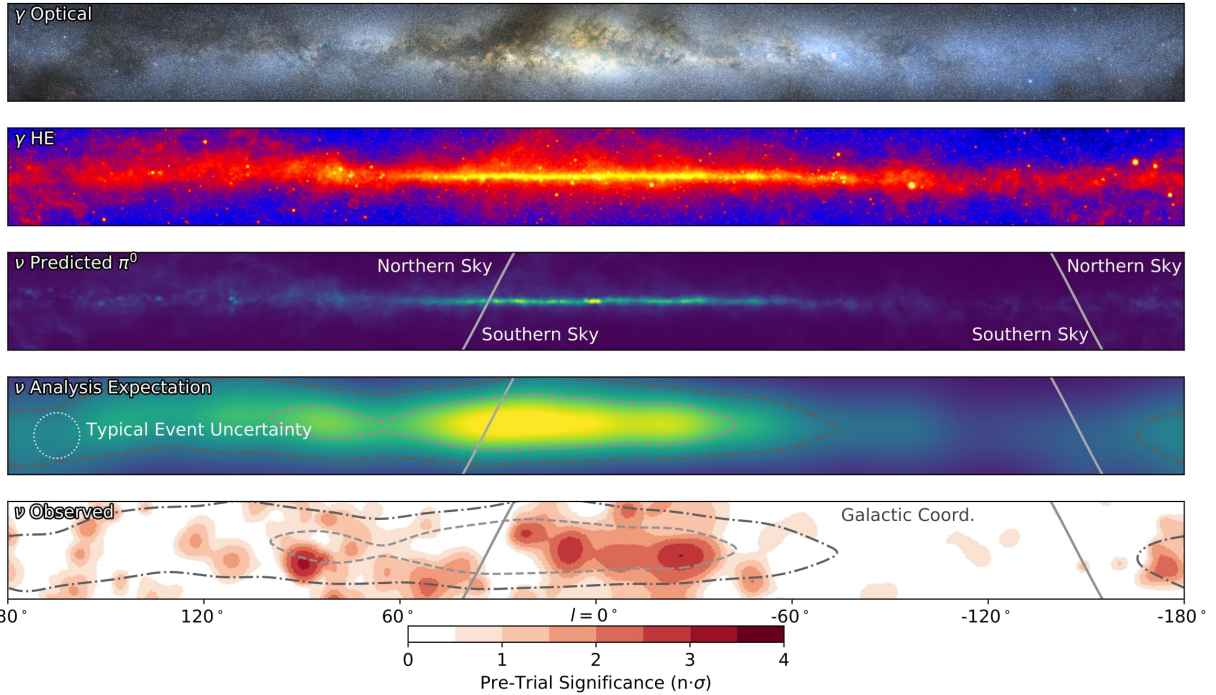


Figure 2.13 The Milky Way Galaxy in photons ( $\gamma$ ) and neutrinos ( $\nu$ ) [22]. The Galactic center is at  $l=0^\circ$  and is the brightest region in all panels. (top) An Optical color image of the Milky Way galaxy seen from Earth. Clouds of gas and dust obscure some light from stars. (2nd down) Integrated flux of  $\gamma$ -rays observed by the Fermi-LAT telescope [23]. (middle) Expected neutrino emission that corresponds with Fermi-LAT observations. (2nd up) Expected neutrino emission profile after considering detector systematics of IceCube. (bottom) Observed neutrino emission from region of the galactic plane. Substantial neutrino emission was detected.

629 The IceCube collaboration recently published a groundbreaking result of the Milky Way in  
 630 neutrinos. The recent result from IceCube, shown in Figure 2.13, proves that we can make  
 631 observations under different messenger regimes. The top two panels show the appearance of the  
 632 galactic plane to different wavelengths of light. Some sources are more apparent in some panels,  
 633 while others are not. This new channel is powerful because neutrinos are readily able to penetrate  
 634 through gas and dust in the Milky Way. This new image also refines our understanding of how high

635 energy particles are produced. For example, the fit to IceCube data prefers neutrino production  
 636 from the decay of  $\pi^0$  [22].

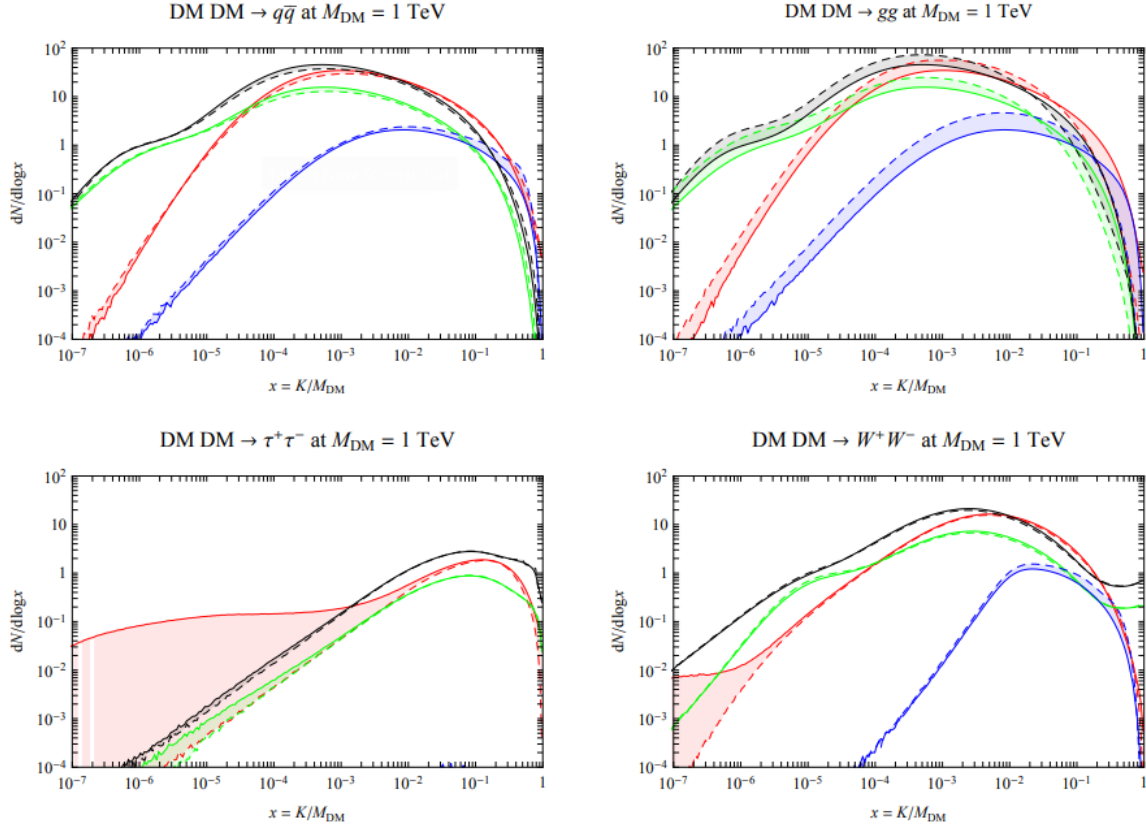


Figure 2.14 Dark Matter annihilation spectra for different final state particle and standard model annihilation channels [24]. Photons (red),  $e^\pm$  (green),  $\bar{p}$  (blue),  $\nu$  (black).

637 Exposing our observations to more cosmic messengers greatly increases our sensitivity to  
 638 rare processes. In the case of DM, Figure 2.14, there are many SM particles produced in DM  
 639 annihilation. Among the final state fluxes are gammas and neutrinos. Charged particles are also  
 640 produced however they would not likely make it to Earth since they will be deflected by magnetic  
 641 fields between the source and Earth. This means observatories that can see the neutral messengers  
 642 are especially good for DM searches and for combining data for a multi-messenger DM search.

## CHAPTER 3

### 643 MULTIMESSENGER ASTROPHYSICS: DETECTING HIGH ENERGY NEUTRAL 644 MESSENGERS

#### 645 3.1 Introduction

646 Before the 20th century, all astrophysics observations were optical in nature. We literally only  
647 saw things with highly magnified optical observations. Then we discovered cosmic rays. cosmic  
648 rays are charged particles, typically naked protons or H+. This was seen by Victor Hess in 19??.  
649 Around the same time we discovered neutrinos from beta decay. Sometime around 1950 we started  
650 to build neutrino detectors which were mostly sensitive to neutrinos from the sun. Finally, it was  
651 theorized that compact objects like black holes and neutron stars would create waves in space-time  
652 when they experience mergers or collisions.

653 In the 21st century, we have developed new observation techniques and detectors that are no only  
654 sensitive to these four messengers - photons ([TODO: photon](#)), neutrinos ([TODO: nu](#)), Cosmic  
655 Rays (CR), and Gravitational Wave (WV) - we're collect high energy versions of these events.  
656 For the standad model particles, we're now sensitive to all messengers above the MeV eneryg  
657 range. Additionally, the GW's were sensitive to are in the stellar mass black hole region and above  
658 within our galactic neighborhood. This means were becoming sensitive to the fundamental physics  
659 occuring within the universe and we can rely on the universe as a TeV+ particle accelerator. We  
660 also have the abaility to correlate high energy events across messengers and gain new insights on  
661 the processes that occur in our universe.

662 This thesis focuses on very high energy (VHE) gamma rays and neutrinos. These can both be  
663 observed through the water cherenkov detection technique altho not exclusively. Methods on how  
664 to detect and observe these neutral messengers are discussed Section 3.3 and Section 3.4

#### 665 3.2 Charged Particles in a Medium

666 For high enery gamma-rays and neutrinos, we can exploit the same effect that charged particles  
667 have with water. This effect is known as Cherenkov radiation. Cherenkov Radiation occurs when a  
668 charged particle, usually electrons ( $e$ ) or muons ( $\mu$ ), traverse a medium, like water, faster than the

669 speed of light in that medium. This is similar to sonic boom where an object moves through air  
670 faster than the speed of sound in air. Cherenkov radiation can therefore be thought of as an 'optic  
671 boom'. Many astro-particle physics experiments will use water as the medium as because water  
672 has a unique set of properties ideal for charged particle tracking.



Figure 3.1 TODO: Show a nuclear reactor with cherenkov radiation[NEEDS A SOURCE][FACT CHECK THIS]

673 The frequency of light emitted due to cherenkov radiation follows the equation:

$$INSERT\ Cherenkov\ wavelength\ calc\ HERE. \quad (3.1)$$

674 The absorption spectra is shown in the following figure:

675 **3.3 Photons ( $\gamma$ )**

676 **3.4 Neutrinos ( $\nu$ )**

677 **3.5 Opportunities to Combine for Dark Matter**



Figure 3.2 TODO: absorption spectrum of liquid and solid water[NEEDS A SOURCE][FACT CHECK THIS]

## **CHAPTER 4**

678                   **HIGH ALTITUDE WATER CHERENKOV (HAWC) OBSERVATORY**

679   **4.1 The Detector**

680   **4.2 Events Reconstruction and Data Acquisition**

681   **4.2.1 G/H Discrimination**

682   **4.2.2 Angle**

683   **4.2.3 Energy**

684   **4.3 Remote Monitoring**

685   **4.3.1 ATHENA Database**

686   **4.3.2 HOMER**

687

## CHAPTER 5

### ICECUBE NEUTRINO OBSERVATORY

688 **5.1 The Detector**

689 **5.2 Events Reconstruction and Data Acquisition**

690 **5.2.1 Angle**

691 **5.2.2 Energy**

692 **5.3 Northern Test Site**

693 **5.3.1 PIgeon remote dark rate testing**

694 **5.3.2 Bulkhead Construction**

## CHAPTER 6

### 695       **GLORY DUCK: MULTI-WAVELENGTH SEARCH FOR DARK MATTTER** 696       **ANNIHILATION TOWARDS DWARF SPHEROIDAL GALAXIES**

#### 697   **6.1 Introduction**

698       The field of astrophysics now has several instruments and observatories sensitive to high  
699       energy gamma-rays. The energy sensitivity for the modern gamma-ray program spans many orders  
700       of magnitude. Figure 6.1 demonstrates these similar sensitivities across energies for the five  
701       experiments: Fermi-LAT, HAWC, HESS, MAGIC, and VERITAS.

702       Each of the five experiments featured in Figure 6.1 have independently searched for DM  
703       annihilation from dwarf spheroidal galaxies (dSph) and set limits. Intriguingly, there are regions of  
704       substantial overlap in their energy sensitivities. This clearly motivates an analysis that combines data  
705       from these five. Each experiment has unique gamma-ray detection methods and their weaknesses  
706       and strengths can be leveraged with each other. The HAWC gamma-ray observatory is extensively  
707       introduced in chapter 4, so it is not introduced here. A brief description of the remaining experiments  
708       are in the following paragraphs.

709       The Large Area Telescope (LAT) is a pair conversion telescope mounted on the NASA Fermi  
710       satellite in orbit  $\sim$ 550 km above the Earth [26]. LAT's field of view covers about 20% of the  
711       whole sky, and it sweeps the whole sky approximately every 3 hours. LAT's gamma-ray energy  
712       sensitivity ranges from 20 MeV up to 1 TeV. Previous DM searches towards dSphs using Fermi-LAT  
713       are published in [27] and [28]

714       The High Energy Spectroscopic System (HESS), Major Atmospheric Gamma Imaging  
715       Cherenkov (MAGIC), and Very Energetic Radiation Imaging Telescope Array System (VERI-  
716       TAS) are arrays of Imaging Atmospheric Cherenkov Telescopes (IACT). These telescopes observe  
717       the Cherenkov light emitted from gamma-ray showers in the Earth's atmosphere. The field of  
718       view for these telescopes is no larger than  $5^\circ$  with energy sensitivities ranging from 30 GeV up  
719       to 100 TeV [29, 30, 31]. IACTs are able to make precise observations in selected regions of the  
720       sky, however can only be operated in ideal dark conditions. HESS's observations of the dwarves

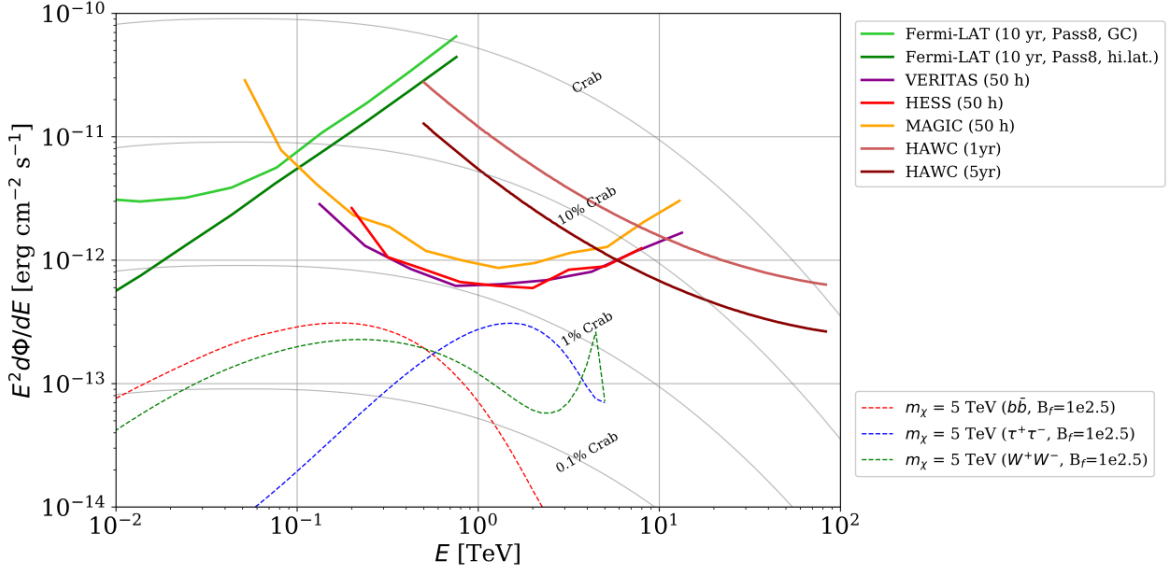


Figure 6.1 Sensitivities of five gamma-ray experiments compared to percentages of the Crab nebula’s emission and dark matter annihilation. Solid lines present estimated sensitivities to power law spectra [FACT CHECK THIS] for each experiment. Green lines are Fermi-LAT sensitivities where lighter green is the sensitivity to the galactic center and dark green is its sensitivity to higher declinations. Orange, red, and purple solid lines represent the MAGIC, HESS, and VERITAS 50 hour sensitivities respectively. The maroon and brown lines are the HAWC 1 year and 5 year sensitivities. Across four decades of gamma-ray energy, these experiments have similar sensitivities on the order  $10^{-12}$  erg  $\text{cm}^{-2}\text{s}^{-1}$ . The dotted lines are estimated dark matter fluxes assuming  $m_\chi = 5$  TeV DM annihilating to bottom quarks (red), tau leptons (blue), and W bosons (green). Faded gray lines outline percentage flux of the Crab nebula. Figure is an augmented version of [25]

721 Sculptor and Carina were between January 2008 and December 2009. HESS’s observations of  
 722 Coma Berenices were from 2010 to 2013, and Fornax was observed in 2010 [32, 33, 34]. MAGIC  
 723 provided deep observations of Segue1 between 2011 and 2013 [35]. MAGIC also provides data  
 724 for three dwarves: Coma Berenices, Draco, and Ursa Major II where observations were made  
 725 in: January - June 2019 [36], March - September 2018 [36], and 2014 - 2016 [37] respectively.  
 726 VERITAS provided data for Boötes I, Draco, Segue 1, and Ursa Minor from 2009 to 2016 [38].

727 This chapter presents the Glory Duck analysis, the name given for the search for dark matter  
 728 annihilation from dSph by combining data from the five gamma-ray observatories: Fermi-LAT,  
 729 HAWC, HESS, MAGIC, and VERITAS. Specifically, the methods in analysis and modeling are  
 730 presented for the HAWC gamma-ray observatory. This work was published to the Journal of  
 731 Cosmology and Astroparticle Physics and presented at the International Cosmic Ray Conference

732 in 2019, 2021, and 2023 [39, 40, 41] and others.

733 **6.2 Dataset and Background**

734 This section enumerates the data and background methods used for HAWC’s study of dSphs.  
735 Section 6.2.1 and Section 6.2.2 are most useful for fellow HAWC collaborators looking to replicate  
736 the Glory Duck analysis.

737 **6.2.1 Itemized HAWC files**

- 738 • Detector Resolution: `response_aerie_svn_27754_systematics_best_mc_test_no`  
739 `broadpulse\_10pctlogchargesmearing_0.63qe_25kHzNoise_run5481_curvatu`  
740 `re0_index3.root`
- 741 • Data Map: `maps-20180119/liff/maptree_1024.root`
- 742 • Spectral Dictionary: `DM_CirrelliSpectrum_dict_gammas.npy`
- 743 • Analysis wiki: [https://private.hawc-observatory.org/wiki/index.php/Glory\\_Duck\\_Multi-Experiment\\_Dark\\_Matter\\_Search](https://private.hawc-observatory.org/wiki/index.php/Glory_Duck_Multi-Experiment_Dark_Matter_Search)

745 **6.2.2 Software Tools and Development**

746 This analysis was performed using HAL and 3ML [42, 43] in Python version 2. I built software  
747 to implement the *A Poor Particle Physicist Cookbook for Dark Matter Indirect Detection* (PPPC)  
748 [44] DM spectral model and dSphs spatial model from [45] for HAWC analysis. A NumPy version  
749 of this dictionary was made for both Py2 and Py3. The code base for creating this dictionary is  
750 linked on my GitLab sandbox:

- 751 • Py2: [Dictionary Generator \(Deprecated\)](#)
- 752 • Py3: [PPPC2Dict](#)

753 The analysis was performed using the  $f_{\text{hit}}$  framework performed in the HAWC Crab paper  
754 [42]. The Python2 NumPy dictionary file for gamma-ray final states is `dmCirSpecDict.npy`. The  
755 corresponding Python3 file is `DM_CirrelliSpectrum_dict_gammas.npy`. These files can also

756 be used for decay channels and the PPPC describes how [44]. All other software used for data  
757 analysis, DM profile generation, and job submission to SLURM are also kept in my sandbox for  
758 [the Glory Duck](#) project.

759 **6.2.3 Data Set and Background Description**

760 The HAWC data maps used for this analysis contain 1017 days of data between runs 2104  
761 (2014-11-26) and 7476 (2017-12-20). They were generated from pass 4.0 reconstruction. The  
762 analysis is performed using the  $f_{hit}$  energy binning scheme with bins (1-9) similar to what was done  
763 for the Crab and previous HAWC dSph analysis [42, 46]. Bin 0 was excluded as it has substantial  
764 hadronic contamination and poor angular resolution.

765 This analysis was done on dSphs because of their large DM mass content relative to baryonic  
766 mass. We consider the following to estimate the background to this study.

- 767 • The dSphs are small in HAWC’s field of view, so the analysis is not sensitive to large or small  
768 scale anisotropies.
- 769 • The dSphs used in this analysis are off the galactic plane.
- 770 • The dSphs are baryonically faint relative to their expected dark matter content and are not  
771 expected to contain high energy gamma-ray sources.

772 Therefor we make no additional assumptions on the background from our sources and use  
773 HAWC’s standard direct integration method for background estimation [42]. It is possible for  
774 gamma rays from DM annihilation to scatter in transit to HAWC via Inverse Compton Scattering  
775 (ICS). This was investigated and its impact on the flux is basically zero. Supporting information  
776 on this is in Section 6.7.1

777 **6.3 Analysis**

778 The expected differential photon flux from DM-DM annihilation to standard model particles,  
779  $d\Phi_\gamma/dE_\gamma$ , over solid angle,  $\Omega$  is described by the familiar equation.

$$\frac{d\Phi_\gamma}{dE_\gamma} = \frac{\langle\sigma v\rangle}{8\pi m_\chi^2} \frac{dN_\gamma}{dE_\gamma} \times \int_{\text{source}} d\Omega \int_{l.o.s} \rho_\chi^2 dl(r, \theta') \quad (6.1)$$

780 Where  $\langle \sigma v \rangle$  is the velocity weighted annihilation cross-section.  $\frac{dN}{dE}$  is the expected differential  
 781 number of photons produced at each energy per annihilation.  $m_\chi$  is the rest mass of the supposed  
 782 DM particle.  $\rho_\chi$  is the DM density.  $J$  is the astrophysical J-factor and is defined as

$$J = \int d\Omega \int_{l.o.s} dl \rho_\chi^2(r, \theta') \quad (6.2)$$

783  $l$  is the distance to the source from Earth.  $r$  is the radial distance from the center of the source.  $\theta'$  is  
 784 the half angle defining a cone containing the DM source. How each component is synthesized and  
 785 considered for HAWC's analysis is presented in the following sections. Section 6.3.1 presents the  
 786 particle physics model for DM annihilation. Section 6.3.2 presents the spatial distributions built  
 787 for each dSph.

### 788 6.3.1 $\frac{dN_\gamma}{dE_\gamma}$ - Particle Physics Component

789 For these spectra, we import the PPPC with Electroweak (EW) corrections [44]. The spectrum  
 790 is implemented as a model script in astromodels for 3ML. The EW corrections were previously not  
 791 considered for HAWC and are significant for DM annihilating to EW coupled SM particles such  
 792 as all leptons, and the  $\gamma$ ,  $Z$ , and  $W$  bosons [46]. Figure 6.2 demonstrates the significance of EW  
 793 corrections for W boson annihilation. Across EW SM channels, the gamma-ray spectra become  
 794 harder than spectra without EW corrections. Tables from the PPPC were reformatted into Python  
 795 NumPy dictionaries for collaboration-wide use. A class in astromodels was developed to include  
 796 the EW correction from the PPPC and is aptly named `PPPCSpectra` within `DM_models.py`.

### 797 6.3.2 $J$ - Astrophysical Component

798 The J-factor profiles for each source are imported from Geringer-Sameth (referred to with  $\mathcal{GS}$ )  
 799 [45]. These were pulled from the publication as  $J(\theta)$ , where  $\theta$  is the angular separation from the  
 800 center of the source. HAWC requires maps in terms of  $\frac{dJ}{d\Omega}$ , so the conversion from the maps was  
 801 done in the following way...

802 First, convert the angular distances to solid angles

$$\Omega = 2 \cdot \pi(1 - \cos(\theta)) \quad (6.3)$$

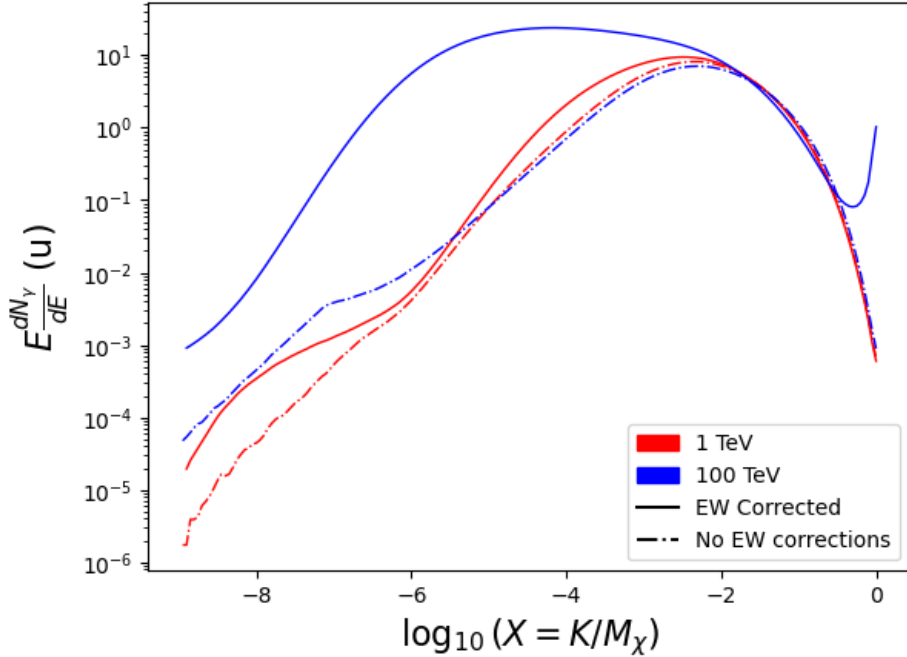


Figure 6.2 Effect of Electroweak (EW) corrections on expected DM annihilation spectrum for  $\chi\chi \rightarrow W^-W^+$ . Solid lines are spectral models that consider EW corrections. Dash-dot lines are spectral models without EW corrections. Red lines are models for  $M_\chi = 1$  TeV. Blue lines represent models for  $M_\chi = 100$  TeV. All models are sourced from the PPPC4DMID [44].

803 which reduces with a small angle approximation to  $\pi\theta^2$ . Next, the central difference for both the  
 804  $\Delta J$  and  $\Delta\Omega$  value were calculated from the discretized  $J(\theta)$  with the central difference stencil:

$$\Delta\phi_i = \phi_{i+1} - \phi_{i-1} \quad (6.4)$$

805 Where  $\phi$  is either  $\Omega$  or  $J$ . These were done separately in case the grid spacing in  $\theta$  was not uniform.  
 806 Finally, these lists are divided so that we are left with an approximation of the  $dJ/d\Omega$  profile that  
 807 is a function of  $\theta$ . Admittedly, this is an approximation method for the map which introduces small  
 808 errors compared to the true profile estimate. This was checked as a systematic against the author's  
 809 profiling of the spatial distribution and is documented in Section 6.8.1.

810 With  $\frac{dJ}{d\Omega}(\theta)$ , a map is generated, first by filling in the north-east quadrant of the map. This  
 811 quadrant is then reflected twice, vertically then horizontally, to fill the full map. Maps are then  
 812 normalized by dividing the discrete 2D integral of the map. The 2D integral was a simple height

813 of bins, Newton's integral:

$$p^2 \cdot \sum_{i,j=0}^{N,M} \frac{dJ}{d\Omega}(\theta_{i,j}, \phi_{i,j}) \quad (6.5)$$

814 These maps are HEALpix maps with NSIDE 16384 and saved in the `.fits` format.

815 Another DM spatial distribution model from Bonnivard ( $\mathcal{B}$ ) [47] was used for the Glory Duck  
816 study. However, to save computational time, limits from  $\mathcal{GS}$  were scaled to  $\mathcal{B}$  instead of each  
817 experiment performing a full study a second time. How these models compare is demonstrated  
818 for each dSph in Figure 6.16 and Figure 6.17 Plots of these maps are provided for each source  
819 in chapter A Examples of the two most impactful dSphs derived from  $\mathcal{GS}$ , Segue1 and Coma  
820 Berenices are featured in Figure 6.3

### 821 **6.3.3 Source Selection and Annihilation Channels**

822 We use many of the dSphs presented in HAWC's previous dSph DM search [46]. HAWC's  
823 sources for Glory Duck include Boötes I, Coma Berenices, Canes Venatici I + II, Draco, Hercules,  
824 Leo I, II, + IV, Segue 1, Sextans, and Ursa Major I + II. A full description of all sources used  
825 in Glory Duck is found in Table 6.1. Triangulum II was excluded from the Glory Duck analysis  
826 because of large uncertainties in its  $J$  factor. Ursa Minor was excluded from HAWC's contribution  
827 to the combination because the source extension model extended Ursa Minor beyond HAWC's field  
828 of view. Ursa Minor was not expected to contribute significantly to the combined limit, so work  
829 was not invested in a solution to include Ursa Minor.

830 This analysis improves on the previous HAWC dSph paper [46] in the following ways. Pre-  
831 viously, the dSphs were treated and implemented as point sources. For this analysis, dSphs are  
832 modeled and treated as extended source. The impact of this change with respect to the upper limit  
833 is source dependent and is explored in Section 6.7.2. Previously, the particle physics model used for  
834 gamma-ray spectra from DM annihilation did not have EW corrections where the PPPC includes  
835 them. Finally, the gamma-ray ray dataset is much larger. The study performed here analyzes over  
836 1000 days of data compared to 507.

837 The SM annihilation channels probed for the Glory Duck combination include  $b\bar{b}$ ,  $e\bar{e}$ ,  $\mu\bar{\mu}$ ,  $\tau\bar{\tau}$ ,  
838  $t\bar{t}$ ,  $W^+W^-$ , and  $ZZ$ . A summary of all sources, with a description of each experiments' sensitivity

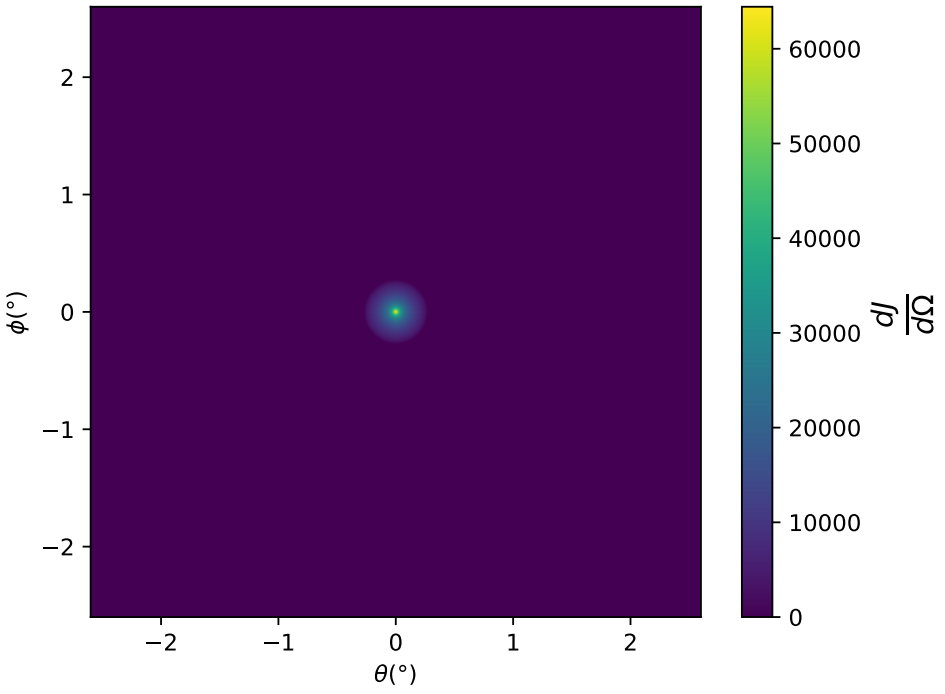
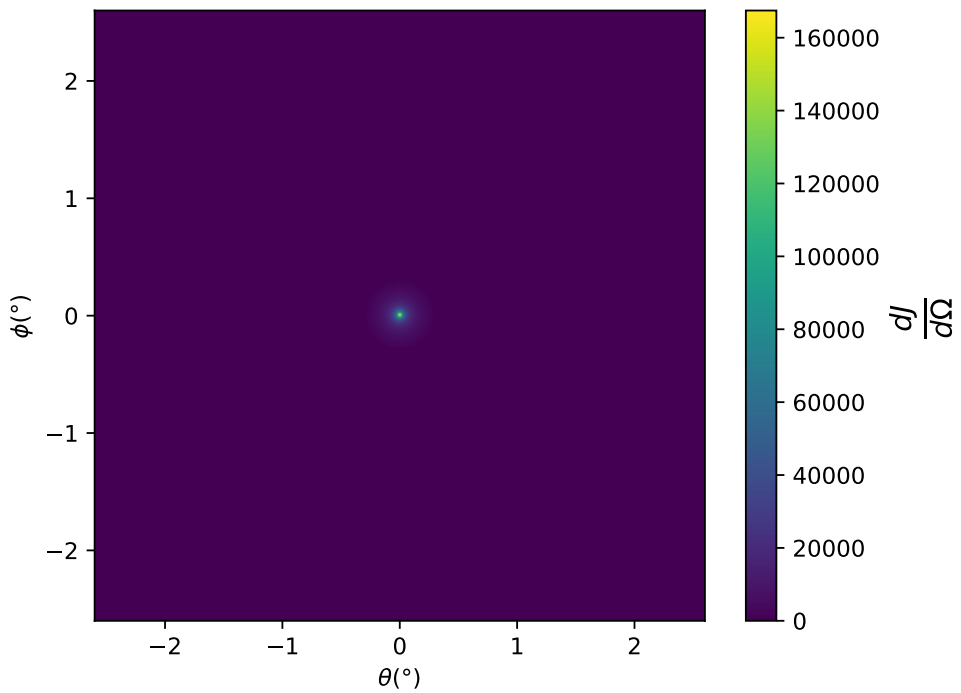


Figure 6.3  $\frac{dJ}{d\Omega}$  maps for Segue1 (top) and Coma Berenices (bottom). Origin is centered on the specific dwarf spheroidal galaxies (dSph). X and Y axes are the angular separation from the center of the dwarf. Plots of the remaining 11 dSph HAWC studied are linked in Fig. A.1.

Table 6.1 Summary of the relevant properties of the dSphs used in the present work. Column 1 lists the dSphs. Columns 2 and 3 present their heliocentric distance and galactic coordinates, respectively. Columns 4 and 5 report the  $J$ -factors of each source given from the  $\mathcal{GS}$  and  $\mathcal{B}$  independent studies and their estimated  $\pm 1\sigma$  uncertainties. The values  $\log_{10} J$  ( $\mathcal{GS}$  set) [45] correspond to the mean  $J$ -factor values for a source extension truncated at the outermost observed star. The values  $\log_{10} J$  ( $\mathcal{B}$  set) [47] are provided for a source extension at the tidal radius of each dSph. **Bolded sources are within HAWC's field of view and provided to the Glory Duck analysis.**

Name	Distance (kpc)	$l, b$ ( $^{\circ}$ )	$\log_{10} J$ ( $\mathcal{GS}$ set) $\log_{10}(\text{GeV}^2 \text{cm}^{-5} \text{sr})$	$\log_{10} J$ ( $\mathcal{B}$ set) $\log_{10}(\text{GeV}^2 \text{cm}^{-5} \text{sr})$
<b>Boötes I</b>	66	358.08, 69.62	$18.24^{+0.40}_{-0.37}$	$18.85^{+1.10}_{-0.61}$
<b>Canes Venatici I</b>	218	74.31, 79.82	$17.44^{+0.37}_{-0.28}$	$17.63^{+0.50}_{-0.20}$
<b>Canes Venatici II</b>	160	113.58, 82.70	$17.65^{+0.45}_{-0.43}$	$18.67^{+1.54}_{-0.97}$
Carina	105	260.11, -22.22	$17.92^{+0.19}_{-0.11}$	$18.02^{+0.36}_{-0.15}$
<b>Coma Berenices</b>	44	241.89, 83.61	$19.02^{+0.37}_{-0.41}$	$20.13^{+1.56}_{-1.08}$
<b>Draco</b>	76	86.37, 34.72	$19.05^{+0.22}_{-0.21}$	$19.42^{+0.92}_{-0.47}$
Fornax	147	237.10, -65.65	$17.84^{+0.11}_{-0.06}$	$17.85^{+0.11}_{-0.08}$
<b>Hercules</b>	132	28.73, 36.87	$16.86^{+0.74}_{-0.68}$	$17.70^{+1.08}_{-0.73}$
<b>Leo I</b>	254	225.99, 49.11	$17.84^{+0.20}_{-0.16}$	$17.93^{+0.65}_{-0.25}$
<b>Leo II</b>	233	220.17, 67.23	$17.97^{+0.20}_{-0.18}$	$18.11^{+0.71}_{-0.25}$
<b>Leo IV</b>	154	265.44, 56.51	$16.32^{+1.06}_{-1.70}$	$16.36^{+1.44}_{-1.65}$
Leo V	178	261.86, 58.54	$16.37^{+0.94}_{-0.87}$	$16.30^{+1.33}_{-1.16}$
Leo T	417	214.85, 43.66	$17.11^{+0.44}_{-0.39}$	$17.67^{+1.01}_{-0.56}$
Sculptor	86	287.53, -83.16	$18.57^{+0.07}_{-0.05}$	$18.63^{+0.14}_{-0.08}$
<b>Segue I</b>	23	220.48, 50.43	$19.36^{+0.32}_{-0.35}$	$17.52^{+2.54}_{-2.65}$
Segue II	35	149.43, -38.14	$16.21^{+1.06}_{-0.98}$	$19.50^{+1.82}_{-1.48}$
<b>Sextans</b>	86	243.50, 42.27	$17.92^{+0.35}_{-0.29}$	$18.04^{+0.50}_{-0.28}$
<b>Ursa Major I</b>	97	159.43, 54.41	$17.87^{+0.56}_{-0.33}$	$18.84^{+0.97}_{-0.43}$
<b>Ursa Major II</b>	32	152.46, 37.44	$19.42^{+0.44}_{-0.42}$	$20.60^{+1.46}_{-0.95}$
Ursa Minor	76	104.97, 44.80	$18.95^{+0.26}_{-0.18}$	$19.08^{+0.21}_{-0.13}$

839 to the source, is provided in Table 6.2.

## 840 6.4 Likelihood Methods

### 841 6.4.1 HAWC Likelihoods

842 For every analysis bin in energy,  $f_{hit}$  bins (1-9), and location, we can expect  $N$  signal events and  
843  $B$  background events. The expected number of excess signal events from dark matter annihilation,

Table 6.2 Summary of dSph observations by each experiment used in this work. A ‘-’ indicates the experiment did not observe the dSph for this study. For Fermi-LAT, the exposure at 1 GeV is given. For HAWC,  $|\Delta\theta|$  is the absolute difference between the source declination and HAWC latitude. HAWC is more sensitive to sources with smaller  $|\Delta\theta|$ . For IACTs, we show the zenith angle range, the total exposure, the energy range, the angular radius  $\theta$  of the signal or ON region, the ratio of exposures between the background-control (OFF) and signal (ON) regions ( $\tau$ ), and the significance of gamma-ray excess in standard deviations,  $\sigma$ .

Source name	Fermi-LAT	HAWC	H.E.S.S, MAGIC, VERITAS						
	Exposure ( $10^{11}$ s m $^2$ )	$ \Delta\theta $ ( $^\circ$ )	IACT	Zenith ( $^\circ$ )	Exposure (h)	Energy range (GeV)	$\theta$ ( $^\circ$ )	$\tau$	$S$ ( $\sigma$ )
Boötes I	2.6	4.5	VERITAS	15 – 30	14.0	100–41000	0.10	8.6	-1.0
Canes Venatici I	2.9	14.6	–	–	–	–	–	–	–
Canes Venatici II	2.9	15.3	–	–	–	–	–	–	–
Carina	3.1	–	H.E.S.S.	27 – 46	23.7	310 – 70000	0.10	18.0	-0.3
Coma Berenices	2.7	4.9	H.E.S.S.	47 – 49	11.4	550 – 70000	0.10	14.4	-0.4
Draco	3.8	38.1	MAGIC	5 – 37	49.5	60 – 10000	0.17	1.0	–
			MAGIC	29 – 45	52.1	70 – 10000	0.22	1.0	–
			VERITAS	25 – 40	49.8	120 – 70000	0.10	9.0	-1.0
Fornax	2.7	–	H.E.S.S.	11 – 25	6.8	230 – 70000	0.10	45.5	-1.5
Hercules	2.8	6.3	–	–	–	–	–	–	–
Leo I	2.5	6.7	–	–	–	–	–	–	–
Leo II	2.6	3.1	–	–	–	–	–	–	–
Leo IV	2.4	19.5	–	–	–	–	–	–	–
Leo V	2.4	–	–	–	–	–	–	–	–
Leo T	2.6	–	–	–	–	–	–	–	–
Sculptor	2.7	–	H.E.S.S.	10 – 46	11.8	200 – 70000	0.10	19.8	-2.2
Segue I	2.5	2.9	MAGIC	13 – 37	158.0	60 – 10000	0.12	1.0	-0.5
			VERITAS	15 – 35	92.0	80 – 50000	0.10	7.6	0.7
Segue II	2.7	–	–	–	–	–	–	–	–
Sextans	2.4	20.6	–	–	–	–	–	–	–
Ursa Major I	3.4	32.9	–	–	–	–	–	–	–
Ursa Major II	4.0	44.1	MAGIC	35 – 45	94.8	120 – 10000	0.30	1.0	-2.1
Ursa Minor	4.1	–	VERITAS	35 – 45	60.4	160 – 93000	0.10	8.4	-0.1

844  $S$ , is estimated by convolving Equation (6.1) with HAWC's energy response and pixel point spread  
 845 functions. I then compute the test statistic (TS) with the log-likelihood ratio test,

$$\text{TS} = -2 \ln \left( \frac{\mathcal{L}_0}{\mathcal{L}^{\max}} \right) \quad (6.6)$$

847 where  $\mathcal{L}_0$  is the null hypothesis, or no DM emission, likelihood.  $\mathcal{L}^{\max}$  is the best fit signal  
 848 hypothesis where  $\langle \sigma v \rangle$  maximizes the likelihood. We calculate the likelihood of each source and  
 849 model, assuming events are Poisson distributed, with

$$\mathcal{L} = \prod_i \frac{(B_i + S_i)^{N_i} e^{-(B_i + S_i)}}{N_i!} \quad (6.7)$$

850 where  $S_i$  is the sum of expected number of signal counts.  $B_i$  is the number of background counts  
 851 observed.  $N_i$  is the total number of counts.

852 I also calculate an upper limit on  $\langle \sigma v \rangle$  by calculating the 95% confidence level (CL). For the  
 853 CL, we define a parameter,  $\text{TS}_{95}$ , as

$$\text{TS}_{95} \equiv \sum_{\text{bins}} \left[ 2N \ln \left( 1 + \frac{\epsilon S_{\text{ref}}}{B} \right) - 2\epsilon S_{\text{ref}} \right] \quad (6.8)$$

854 where the expected signal counts from a dSph is scaled by  $\epsilon$ .  $S_{\text{ref}}$  is the expected number of excess  
 855 counts in a bin from DM emission from a dSph with a corresponding annihilation cross-section,  
 856  $\langle \sigma v \rangle$ . We scan  $\epsilon$  such that

$$2.71 = \text{TS}_{\max} - \text{TS}_{95} \quad (6.9)$$

#### 857 6.4.2 Glory Duck Joint Likelihood

858 The joint likelihood for the 5-experiment combination was done similarly as Section 6.4.1. We  
 859 calculate upper limits on  $\langle \sigma v \rangle$  from the TS, Eq. (6.6), and define the likelihood ratio more generally

$$\lambda(\langle \sigma v \rangle | \mathcal{D}_{\text{dSphs}}) = \frac{\mathcal{L}(\langle \sigma v \rangle; \hat{\nu} | \mathcal{D}_{\text{dSphs}})}{\mathcal{L}(\widehat{\langle \sigma v \rangle}; \hat{\nu} | \mathcal{D}_{\text{dSphs}})} \quad (6.10)$$

860  $\mathcal{D}_{\text{dSphs}}$  is the totality of observations across experiments and dSphs.  $\nu$  are the nuisance parameters  
 861 which are the  $J$  factors in this study.  $\widehat{\langle \sigma v \rangle}$  and  $\hat{\nu}$  are the respective estimate that maximize  $\mathcal{L}$   
 862 globally. Finally,  $\hat{\nu}$  is the set of nuisance parameters that maximize  $\mathcal{L}$  for a fixed value of  $\langle \sigma v \rangle$ .

863        The *complete* joint likelihood,  $\mathcal{L}$  that encompasses all observations from all instruments and  
 864   dSphs can be factorized into *partial* functions for each dSph  $l$  (with  $\mathcal{L}_{\text{dSph},l}$ ) and its  $J$  factor ( $\mathcal{J}_l$ ):

$$\mathcal{L} (\langle \sigma v \rangle; \nu | \mathcal{D}_{\text{dSphs}}) = \prod_{l=1}^{N_{\text{dSphs}}} \mathcal{L}_{\text{dSph},l} (\langle \sigma v \rangle; J_l, \nu_l | \mathcal{D}_l) \times \mathcal{J}_l (J_l | J_{l,\text{obs}}, \sigma_{\log J_l}). \quad (6.11)$$

865   For this study,  $N_{\text{dSphs}} = 20$  is the number of dSphs studied.  $\mathcal{D}_l$  are the gamma-ray observations  
 866   of dSph,  $l$ .  $\nu_l$  are the nuisance parameters modifying the gamma-ray observations of dSph,  $l$ ,  
 867   but excludes  $\mathcal{J}_l$ .  $\mathcal{J}_l$  is the  $J$  factor for dSph,  $l$ , as defined in Equation (6.2), and it is a nuisance  
 868   parameter whose value is unknown.  $\log_{10} J_{l,\text{obs}}$  and  $\sigma_{\log J_l}$  are obtained from fitting a log-normal  
 869   function of  $J_{l,\text{obs}}$  to the posterior distribution of  $J_l$  [48].  $\log_{10} J_{l,\text{obs}}$  and  $\sigma_{\log J_l}$  values are provided  
 870   in Table 6.1. The term  $\mathcal{J}_l$  constraining  $J_l$  is written as:

$$\mathcal{J}_l (J_l | J_{l,\text{obs}}, \sigma_{\log J_l}) = \frac{1}{\ln(10) J_{l,\text{obs}} \sqrt{2\pi} \sigma_{\log J_l}} \exp\left(-\frac{(\log_{10} J_l - \log_{10} J_{l,\text{obs}})^2}{2\sigma_{\log J_l}^2}\right). \quad (6.12)$$

871   Both the  $\mathcal{GS}$  and  $\mathcal{B}$ , displayed in Table 6.1, sets of  $J$  factors are used in this analysis. Equation (6.12)  
 872   is also normalized, so it can also be interpreted as a probability density function (PDF) for  $J_{l,\text{obs}}$ .  
 873   From Equation (6.1), we can also see that  $\langle \sigma v \rangle$  and  $J_l$  are degenerate when computing  $\mathcal{L}_{\text{dSph},l}$ .  
 874   Therefore, as noted in [49], it is sufficient to compute  $\mathcal{L}_{\text{dSph},l}$  versus  $\langle \sigma v \rangle$  for a fixed value of  $J_l$ .  
 875   We used  $J_{l,\text{obs}}(\mathcal{GS})$  reported in Tab. 6.1, in order to perform the profile of  $\mathcal{L}$  with respect to  $J_l$ .  
 876   The degeneracy implies that for any  $J'_l \neq J_{l,\text{obs}}$  (in practice in our case we used  $J'_l = J_{l,\text{obs}}(\mathcal{B})$  to  
 877   compute results from a different set of  $J$  factors):

$$\mathcal{L}_{\text{dSph},l} (\langle \sigma v \rangle; J'_l, \nu_l | \mathcal{D}_l) = \mathcal{L}_{\text{dSph},l} \left( \frac{J'_l}{J_{l,\text{obs}}} \langle \sigma v \rangle; J_{l,\text{obs}}, \nu_l | \mathcal{D}_l \right), \quad (6.13)$$

878   which is a straightforward rescaling operation that reduces the computational needs of the profiling  
 879   operation since:

$$\mathcal{L} (\langle \sigma v \rangle; \hat{\nu} | \mathcal{D}_{\text{dSphs}}) = \prod_{l=1}^{N_{\text{dSphs}}} \max_{J_l} \left[ \mathcal{L}_{\text{dSph},l} (\langle \sigma v \rangle; J_l, \hat{\nu}_l | \mathcal{D}_l) \times \mathcal{J}_l (J_l | J_{l,\text{obs}}, \sigma_{\log J_l}) \right]. \quad (6.14)$$

880   In addition, Eq. (6.13) enables the combination of data from different gamma-ray instruments and  
 881   observed dSphs via tabulated values of  $\mathcal{L}_{\text{dSph},l}$ , or equivalently of  $\lambda$  from Eq. (6.10) as was done in

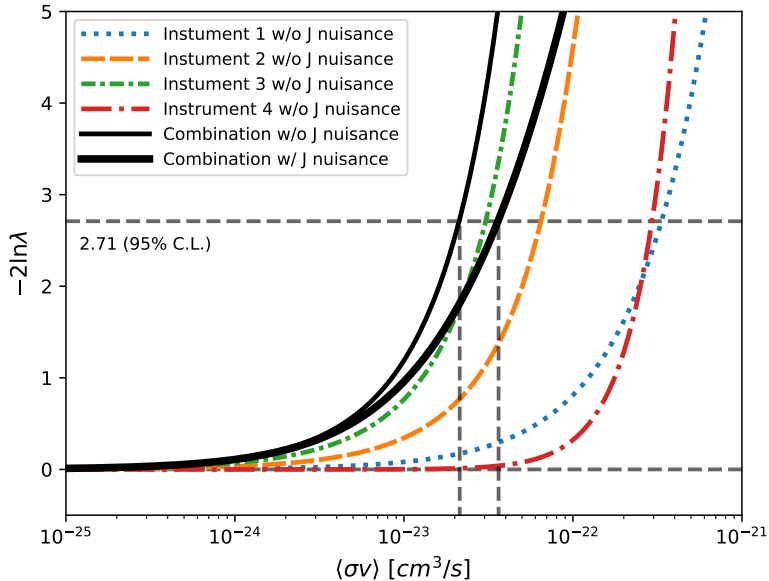


Figure 6.4 Illustration of the combination technique showing a comparison between  $-2 \ln \lambda$  provided by four instruments (colored lines) from the observation of the same dSph without any  $J$  nuisance and their sum, *i.e.* the resulting combined likelihood (thin black line). According to the test statistics of Equation (6.6), the intersection of the likelihood profiles with the line  $-2 \ln \lambda = 2.71$  indicates the 95% C.L. upper limit on  $\langle \sigma v \rangle$ . The combined likelihood (thin black line) shows a smaller value of upper limit on  $\langle \sigma v \rangle$  than those derived by individual instruments. We also show how the uncertainties on the  $J$  factor effects the combined likelihood and degrade the upper limit on  $\langle \sigma v \rangle$  (thick black line). All likelihood profiles are normalized so that the global minimum  $\widehat{\langle \sigma v \rangle}$  is 0. We note that each profile depends on the observational conditions in which a target object was observed. The sensitivity of a given instrument can be degraded and the upper limits less constraining if the observations are performed in non-optimal conditions such as a high zenith angle or a short exposure time.

882 this work, versus  $\langle \sigma v \rangle$ .  $\mathcal{L}_{dSph,l}$  is computed for a fixed value of  $J_l$  and profiled with respect to all  
 883 instrumental nuisance parameters  $\nu_l$ , these nuisance parameters are discussed in more detail below.  
 884 These values are produced by each detector independently and therefore there is no need to share  
 885 sensitive low-level information used to produce them, such as event lists. Figure 6.4 illustrates the  
 886 multi-instrument combination technique used in this study with a comparison of the upper limit  
 887 on  $\langle \sigma v \rangle$  obtained from the combination of the observations of four experiments towards one dSph  
 888 versus the upper limit from individual instruments. It also shows graphically the effect of the  
 889  $J$ -factor uncertainty on the combined observations.

890 The *partial* joint likelihood function for gamma-ray observations of each dSph ( $\mathcal{L}_{dSph,l}$ ) is

written as the product of the likelihood terms describing the  $N_{\text{exp},l}$  observations performed with any of our observatories:

$$\mathcal{L}_{\text{dSph},l} (\langle \sigma v \rangle; J_l, \nu_l | \mathcal{D}_l) = \prod_{k=1}^{N_{\text{exp},l}} \mathcal{L}_{lk} (\langle \sigma v \rangle; J_l, \nu_{lk} | \mathcal{D}_{lk}), \quad (6.15)$$

where each  $\mathcal{L}_{lk}$  term refers to an observation of the  $l$ -th dSph with associated  $k$ -th instrument responses.  $N_{\text{exp},l}$  varies from dSph to dSph and can be inferred from Table 6.2.

Each collaboration separately analyzes their data for  $\mathcal{D}_{lk}$  corresponding to dSph  $l$  and gamma-ray detector  $k$ , using as many common assumptions as possible in the analysis. HAWC’s treatment was described earlier in Section 6.4.1 whereas the specifics of the remaining experiments is left to the publication. We compute the values for the likelihood functions  $\mathcal{L}_{lk}$  (see Eq. (6.15)) for a fixed value of  $J_l$  and profile over the rest of the nuisance parameters  $\nu_{lk}$ . Then, values of  $\lambda$  from Eq. (6.10) are computed as a function of  $\langle \sigma v \rangle$ , and shared using a common format. Results are computed for seven annihilation channels,  $W^+W^-$ ,  $ZZ$ ,  $b\bar{b}$ ,  $t\bar{t}$ ,  $e^+e^-$ ,  $\mu^+\mu^-$ , and  $\tau^+\tau^-$  over 62  $m_\chi$  values between 5 GeV and 100 TeV provided in [44]. The  $\langle \sigma v \rangle$  range is defined between  $10^{-28}$  and  $10^{-18} \text{ cm}^3 \cdot \text{s}^{-1}$ , with 1001 logarithmically spaced values. The likelihood combination, i.e. Equation (6.11), and profile over the  $J$ -factor to compute the profile likelihood ratio  $\lambda$ , Equation (6.10), are carried out with two different public analysis software packages, namely `gLike` [50] and `LklCom` [51], that provide the same results [52].

As mentioned previously, each experiment computes the  $\mathcal{L}_{lk}$  from Equation (6.10) differently. The remainder of this section highlights the differences in this calculation across the experiments. Four experiments, namely *Fermi*-LAT, H.E.S.S., HAWC and MAGIC, use a binned likelihood to compute the  $\mathcal{L}_{lk}$ . For these experiments, for each observation  $\mathcal{D}_{lk}$  of a given dSph  $l$  carried out using a given gamma-ray detector  $k$ , the binned likelihood function is:

$$\mathcal{L}_{lk} (\langle \sigma v \rangle; J_l, \nu_{lk} | \mathcal{D}_{lk}) = \prod_{i=1}^{N_E} \prod_{j=1}^{N_P} \left[ \mathcal{P}(s_{lk,ij}(\langle \sigma v \rangle, J_l, \nu_{lk}) + b_{lk,ij}(\nu_{lk}) | N_{lk,ij}) \right] \times \mathcal{L}_{lk,\nu} (\nu_{lk} | \mathcal{D}_{\nu_{lk}}) \quad (6.16)$$

where  $N_E$  and  $N_P$  are the number of considered bins in reconstructed energy and arrival direction, respectively;  $\mathcal{P}$  represents a Poisson PDF for the number of gamma-ray candidate events  $N_{lk,ij}$

914 observed in the  $i$ -th bin in energy and  $j$ -th bin in arrival direction, when the expected number is  
 915 the sum of the expected mean number of signal events  $s_{ij}$  (produced by DM annihilation) and of  
 916 background events  $b_{ij}$ ;  $\mathcal{L}_{lk,\nu}$  is the likelihood term for the extra  $\nu_{lk}$  nuisance parameters that vary  
 917 from one instrument  $k$  to another. The expected counts for signal events  $s_{ij}$  for a given dSph  $l$  and  
 918 detector  $k$  is given by:

$$s_{ij}(\langle\sigma\nu\rangle, J) = \int_{E'_{\min,i}}^{E'_{\max,i}} dE' \int_{P'_{\min,j}}^{P'_{\max,j}} d\Omega' \int_0^\infty dE \int_{\Delta\Omega_{tot}} d\Omega \int_0^{T_{\text{obs}}} dt \frac{d^2\Phi(\langle\sigma\nu\rangle, J)}{dEd\Omega} \text{IRF}(E', P' | E, P, t) \quad (6.17)$$

919 where  $E'$  and  $E$  are the reconstructed and true energies,  $P'$  and  $P$  the reconstructed and true  
 920 arrival directions;  $E'_{\min,i}$ ,  $P'_{\min,j}$ ,  $E'_{\max,i}$ , and  $P'_{\max,j}$  are their lower and upper limits of the  $i$ -th  
 921 energy bin and the  $j$ -th arrival direction bin;  $T_{\text{obs}}$  is the (dead-time corrected) total observation  
 922 time;  $t$  is the time along the observations;  $d^2\Phi/dEd\Omega$  is the DM flux in the source region (see  
 923 Equation (6.1)); and  $\text{IRF}(E', P' | E, P, t)$  is the IRF, which can be factorized as the product of the  
 924 effective collection area of the detector  $A_{\text{eff}}(E, P, t)$ , the PDFs for the energy estimator  $f_E(E' | E, t)$ ,  
 925 and arrival direction  $f_P(P' | E, P, t)$  estimators. Note that for Fermi-LAT, HAWC, MAGIC, and  
 926 VERITAS the effect of the finite angular resolution is taken into account through the convolution  
 927 of  $d\Phi/dEd\Omega$  with  $f_P$  in Equation (6.17), whereas in the cases of H.E.S.S.  $f_P$  is approximated by a  
 928 delta function. This approximation has been made in order to maintain compatibility of the result  
 929 with what has been previously published. The difference introduced by this approximation is  $< 5\%$   
 930 for all considered dSphs. A more comprehensive review of the differences between the analyses of  
 931 different instruments can be found in [25].

## 932 6.5 HAWC Results

933 13 of the 20 dSphs considered for the Glory Duck analysis are within HAWC's field of view.  
 934 These dSph are analyzed for emission from DM annihilation according to the likelihood method  
 935 described in Section 6.4. The 13 likelihood profiles are then stacked to synthesize a combined  
 936 limit on the dark matter cross-section,  $\langle\sigma\nu\rangle$ . This combination is done for the 7 SM annihilation  
 937 channels used in the Glory Duck analysis. Figure 6.5 shows the combined limit for all annihilation  
 938 channels with HAWC only observations. We also perform 300 studies of Poisson trials on the

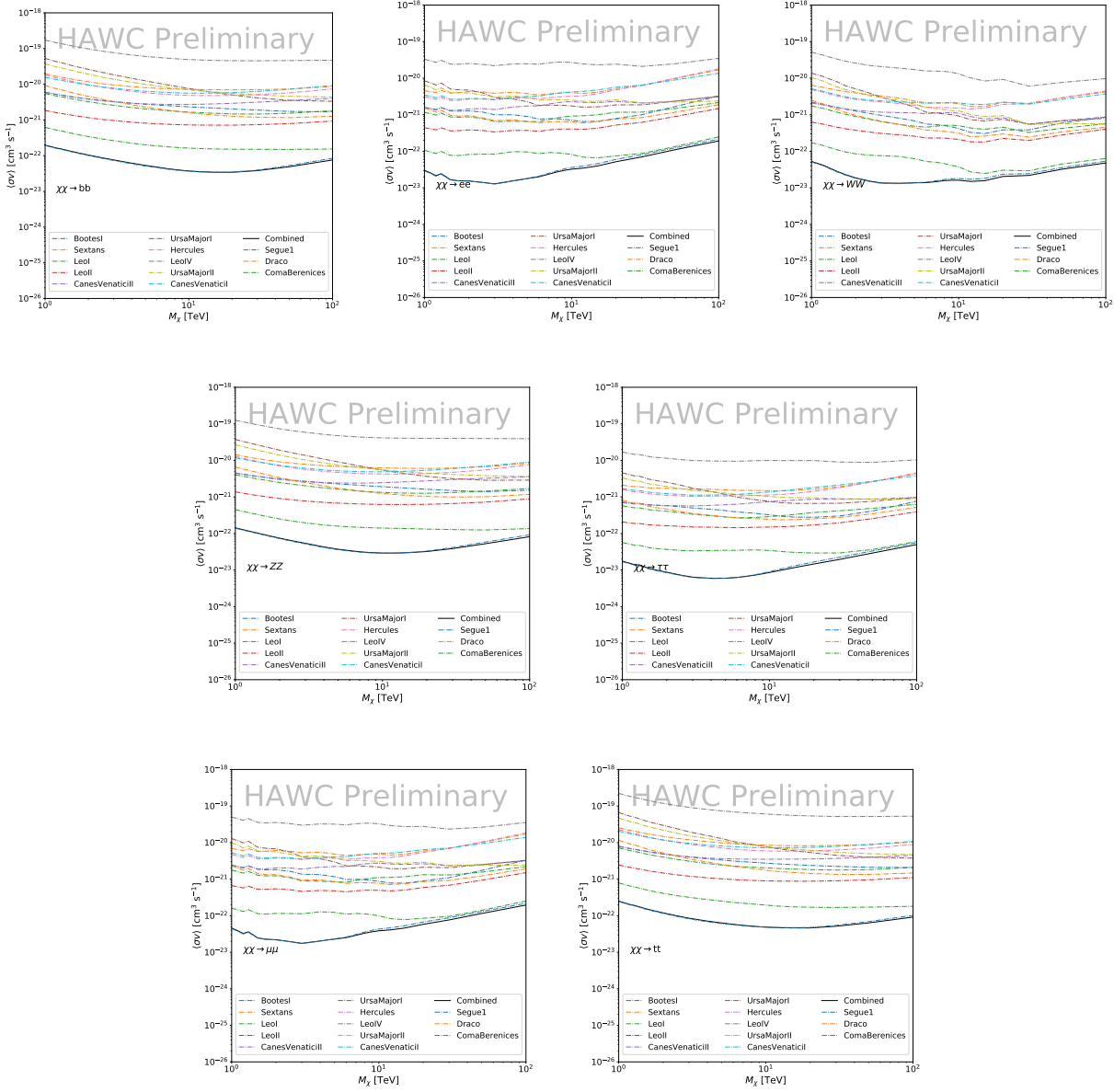


Figure 6.5

background. These trials are used to produce HAWC Brazil bands which were shared with the other collaborators for combined Brazil Bands. The results on fitting to HAWC's Poisson trials of the DM hypothesis is shown in Figure 6.7 for all the DM annihilation channels studied for Glory Duck.

No DM was found in HAWC observations. HAWC's limits are dominated by the dSphs Segue1 and Coma Berenices. The remaining 11 dSphs do not contribute significantly to the limit because

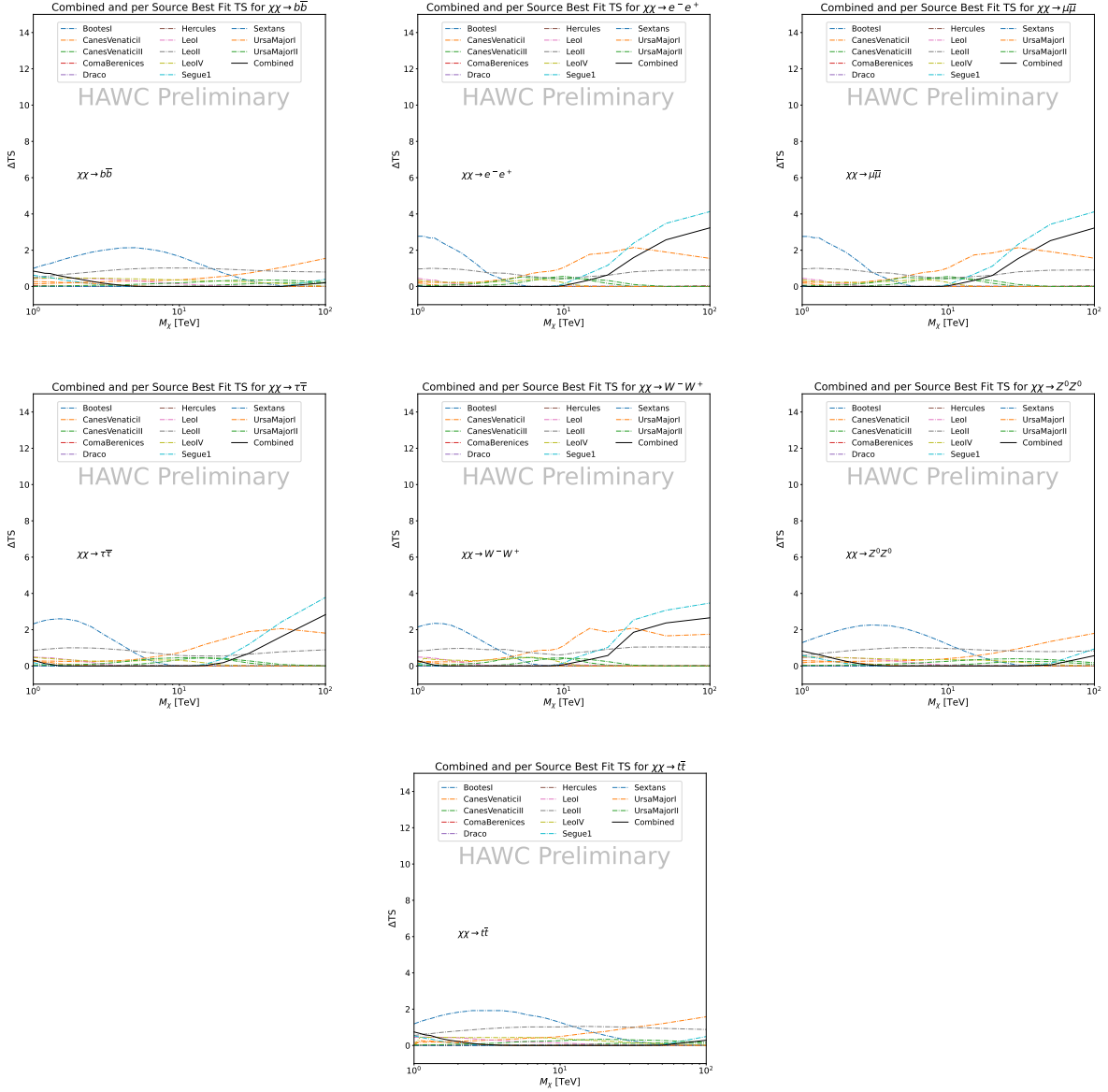


Figure 6.6 HAWC TS values for best fit  $\langle \sigma v \rangle$  versus  $m_\chi$  for seven SM annihilation channels with  $J$  factors from  $\mathcal{GS}$ . The solid black line shows the combined best fit TS values. The colored, dashed lines are the TS values for each of the 13 sources HAWC studied.

945 they are at high zenith and/or have much smaller  $J$  factors. Even though some remaining dSphs  
 946 have large  $J$  factors, they are towards the edge of HAWC's field of view where HAWC analysis is  
 947 less sensitive.

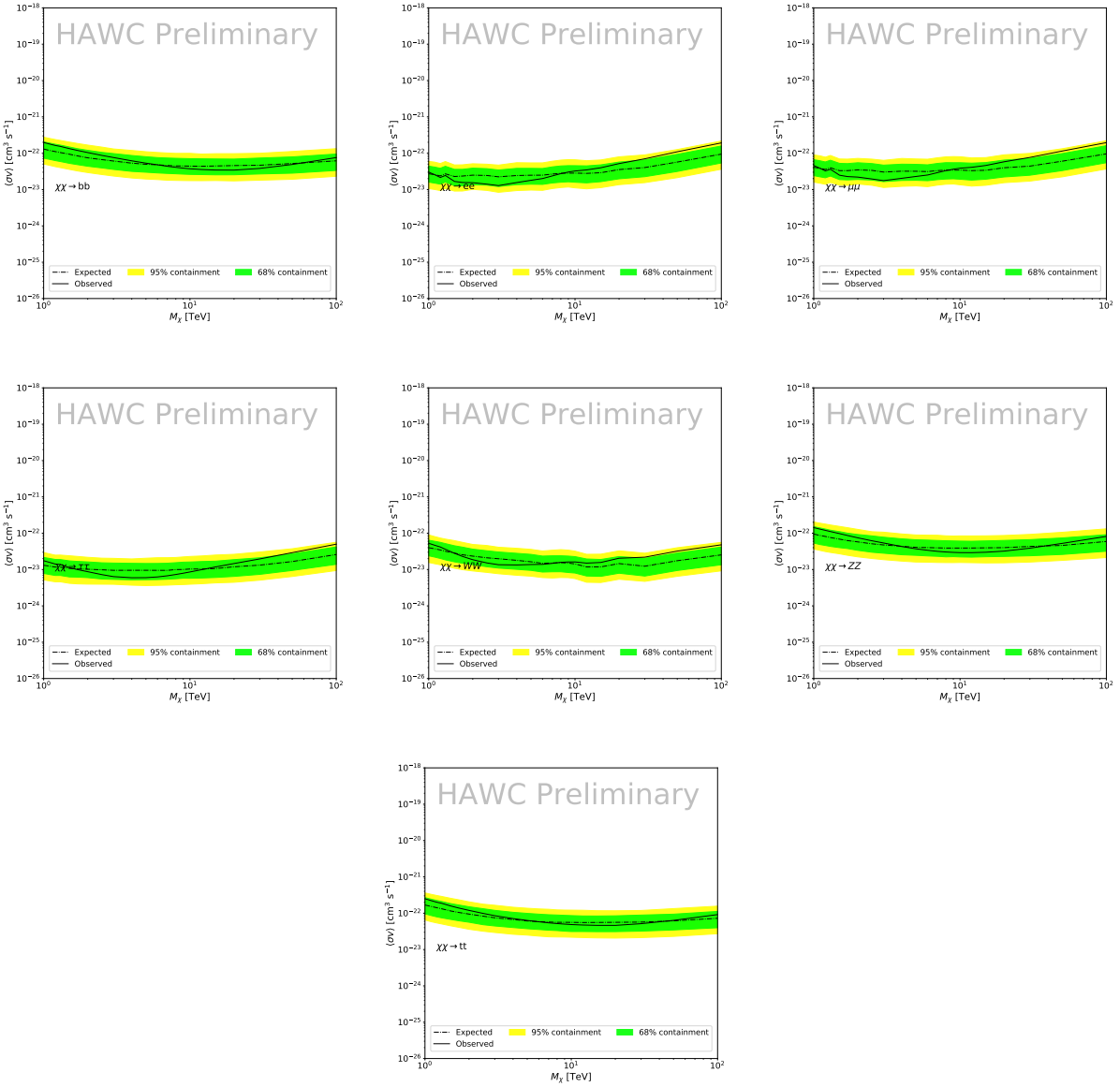


Figure 6.7 HAWC Brazil bands at 95% confidence level on  $\langle\sigma v\rangle$  versus DM mass for seven annihilation channels with  $J$ -factors from  $\mathcal{GS}$  [53]. The solid line represents the combined limit from 13 dSphs. The dashed line is the expected limit. The green band is the 68% containment. The yellow band is the 95% containment.

## 948 6.6 Glory Duck Combined Results

949 The crux of this analysis is that HAWC's results are combined with 4 other gamma-ray observa-  
 950 tories: Fermi-LAT, H.E.S.S., MAGIC, and VERITAS. No significant DM emission was observed  
 951 by any of the five instruments. We present the upper limits on  $\langle\sigma v\rangle$  assuming seven independent  
 952 DM self annihilation channels, namely  $W^+W^-$ ,  $Z^+Z^-$ ,  $b\bar{b}$ ,  $t\bar{t}$ ,  $e^+e^-$ ,  $\mu^+\mu^-$ , and  $\tau^+\tau^-$ . The 68%

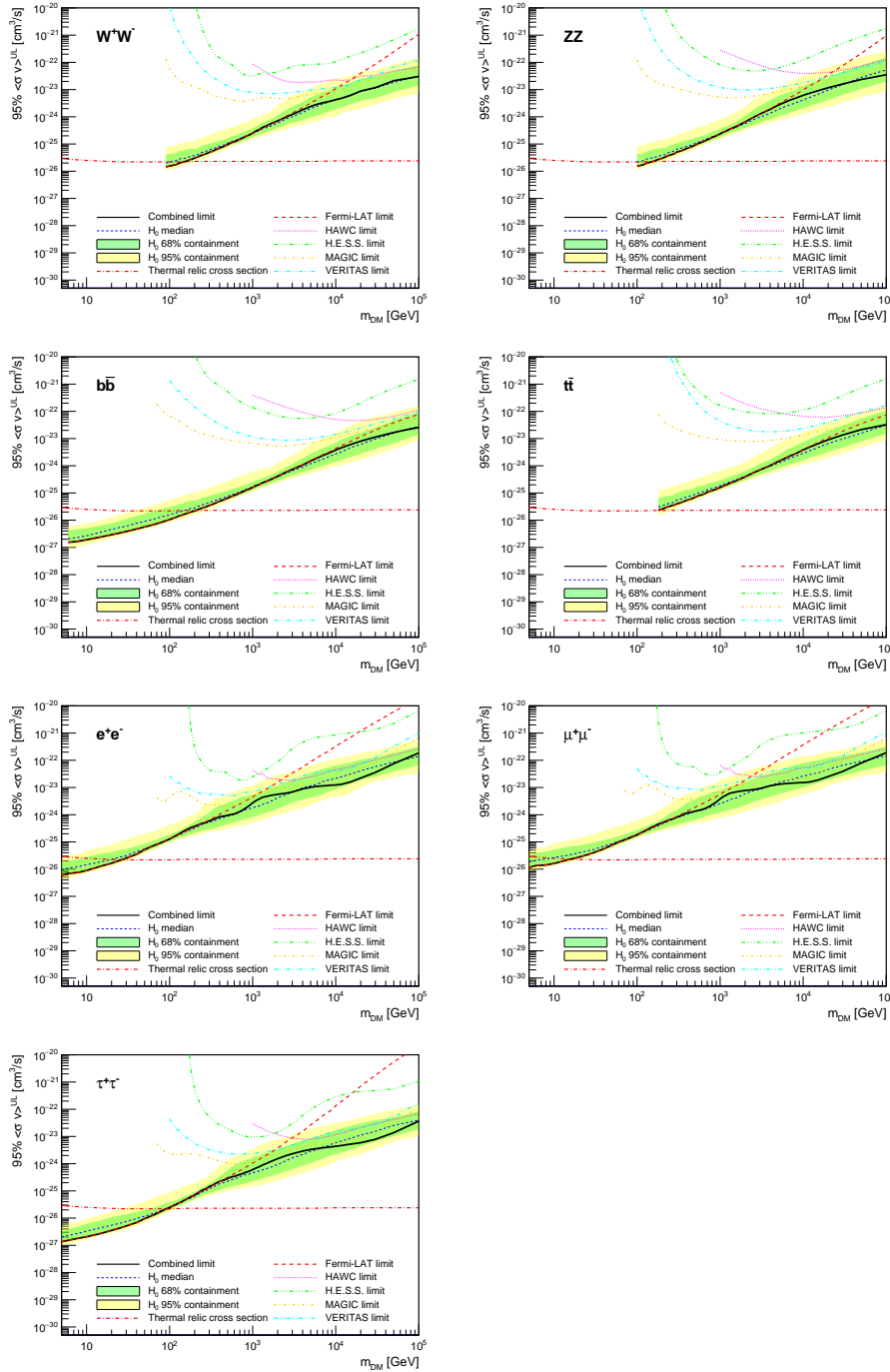


Figure 6.8 Upper limits at 95% confidence level on  $\langle\sigma v\rangle$  in function of the DM mass for eight annihilation channels, using the set of  $J$  factors from Ref. [53] ( $\mathcal{GS}$  set in Table 6.1). The black solid line represents the observed combined limit, the black dashed line is the median of the null hypothesis corresponding to the expected limit, while the green and yellow bands show the 68% and 95% containment bands. Combined upper limits for each individual detector are also indicated as solid, colored lines. The value of the thermal relic cross-section in function of the DM mass is given as the red dotted-dashed line [54].

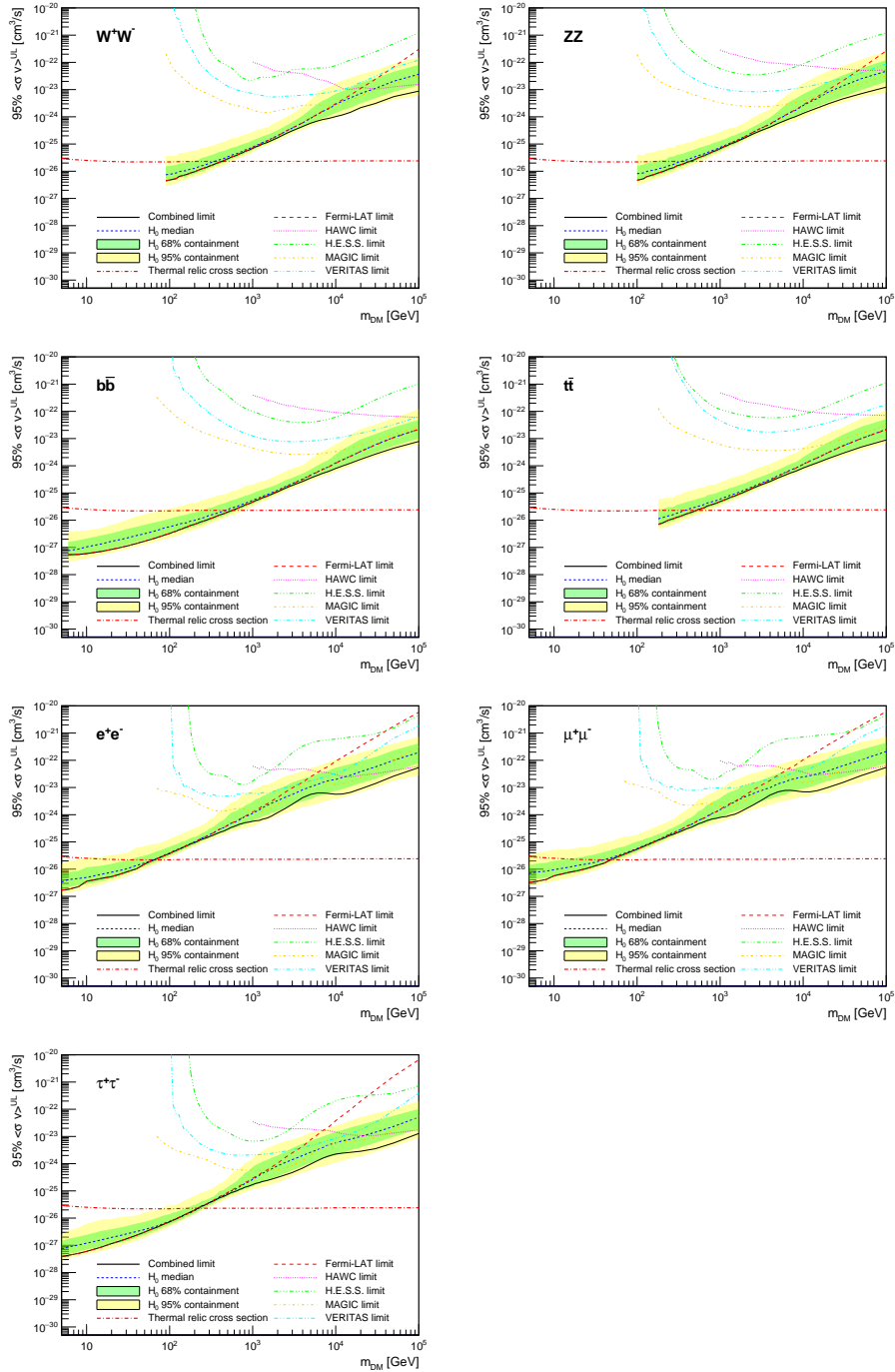


Figure 6.9 Same as Fig. 6.8, using the set of  $J$  factors from Ref. [47, 55] ( $\mathcal{B}$  set in Table 6.1).

and 95% containment bands are produced from 300 Poisson realizations of the null hypothesis corresponding to each of the combined datasets. These 300 realizations are combined identically to dSph observations. The containment bands and the median are extracted from the distribution of resulting limits on the null hypothesis. These 300 realizations are obtained either by fast simu-

957 lations of the OFF observations, for H.E.S.S., MAGIC, VERITAS, and HAWC, or taken from real  
958 observations of empty fields of view in the case of Fermi-LAT [48, 56, 57].

959 The obtained limits are shown in Figure 6.8 for the  $\mathcal{G}\mathcal{S}$  set of  $J$ -factors [53] and in Figure 6.9  
960 for the  $\mathcal{B}$  set of  $J$ -factors [47, 55]. The combined limits are presented with their 68% and 95%  
961 containment bands, and are expected to be close to the median limit when no signal is present.  
962 We observe agreement with the null hypothesis for all channels, within  $2\sigma$  standard deviations,  
963 between the observed limits and the expectations given by the median limits. Limits obtained from  
964 each detector are also indicated in the figures, where limits for all dSphs observed by the specific  
965 instrument have been combined.

966 Below  $\sim 300$  GeV, the *Fermi*-LAT dominates the DM limits for all annihilation channels. From  
967  $\sim 300$  GeV to  $\sim 2$  TeV, *Fermi*-LAT continues to dominate for the hadronic and bosonic DM channels,  
968 yet the IACTs (H.E.S.S., MAGIC, and VERITAS) and *Fermi*-LAT all contribute to the limit for  
969 leptonic DM channels. For DM masses between  $\sim 2$  TeV to  $\sim 10$  TeV, the IACTs dominate leptonic  
970 DM annihilation channels, whereas both the *Fermi*-LAT and the IACTs dominate bosonic and  
971 hadronic DM annihilation channels. From  $\sim 10$  TeV to  $\sim 100$  TeV, both the IACTs and HAWC  
972 contribute significantly to the leptonic DM limit. For hadronic and bosonic DM, the IACTs and  
973 *Fermi*-LAT both contribute strongly.

974 We notice that the limits computed using the  $\mathcal{B}$  set of  $J$ -factor are always better compared to the  
975 ones calculated with the  $\mathcal{G}\mathcal{S}$  set. For the  $W^+W^-$ ,  $Z^+Z^-$ ,  $b\bar{b}$ , and  $t\bar{t}$  channels, the ratio between the  
976 limits computed with the two sets of  $J$ -factor is varying between a factor of  $\sim 3$  and  $\sim 5$  depending  
977 on the energy, with the largest ratio around 10 TeV. For the channels  $e^+e^-$ ,  $\mu^+\mu^-$ , and  $\tau^+\tau^-$ , the  
978 ratio lies between  $\sim 2$  to  $\sim 6$ , being maximum around 1 TeV. Examining Figure 6.16 and Figure 6.17  
979 in Section 6.8, these differences are explained by the fact that the  $\mathcal{B}$  set provides higher  $J$ -factors  
980 for the majority of the studied dSphs, with the notable exception of Segue I. The variation on the  
981 ratio of the limits for the two sets is due to different dSph dominating the limits depending on the  
982 energy. This pushes the range of thermal cross-section which can be excluded to higher mass. This  
983 comparison demonstrates the magnitude of systematic uncertainties associated with the choice of

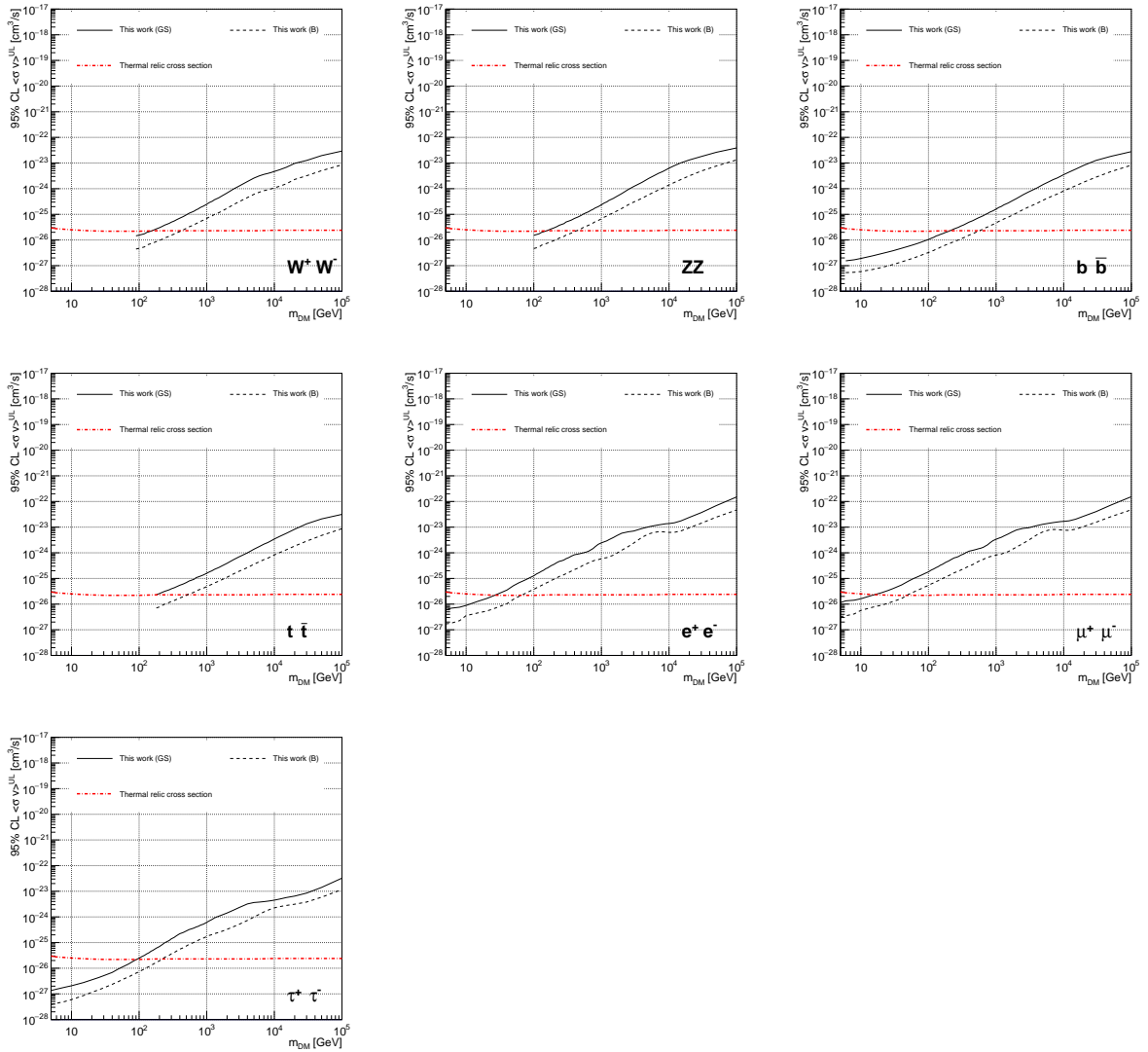


Figure 6.10 Comparisons of the combined limits at 95% confidence level for each of the eight annihilation channels when using the  $J$  factors from Ref. [53] ( $\mathcal{GS}$  set in Table 6.1), plain lines, and the  $J$  factor from Ref. [47, 55] ( $\mathcal{B}$  set in Table 6.1), dashed lines. The cross-section given by the thermal relic is also indicated [54].

984 the  $J$ -factor

985 This comparison demonstrates the magnitude of systematic uncertainties associated with the  
 986 choice of the  $J$ -factor calculation. The  $\mathcal{GS}$  and  $\mathcal{B}$  sets present a difference in the limits for all  
 987 channels of about This difference is explained, see Figure 6.16 and Figure 6.17 in Appendix, by the  
 988 fact that the  $\mathcal{B}$  set provides higher  $J$  factors for all dSph except for Segue I. This pushes the range  
 989 of thermal cross-section which can be excluded to higher mass.

990 **6.7 HAWC Systematics**

991 **6.7.1 Inverse Compton Scattering**

992 The DM-DM annihilation channels produce many high energy electrons regardless of the  
993 primary annihilation channel. These high energy electrons can produce high energy gamma-rays  
994 through Inverse Compton Scattering (ICS). If this effect is strong, it would change the morphology  
995 of the source and increase the total expected gamma-ray counts from any source. The PPPC [44]  
996 provides tools in Mathematica for calculating the impact of ICS for an arbitrary location in the  
997 sky for a specified annihilation channel. We calculated the change in gamma-ray counts for DM  
998 annihilation to primary  $e\bar{e}$  for RA and Dec corresponding to Segue1 and Coma Berenices. These  
999 dSphs were chosen because they are the strongest contributors to the limit.  $e\bar{e}$  was selected because  
1000 it would have the largest number of high energy electrons. The effect was found to be on the order  
1001 of  $10^{-7}$  on the gamma-ray spectrum. As a result, this systematic is not considered in our analysis.

1002 **6.7.2 Point Source Versus Extended Source Limits**

1003 The previous DM search toward dSph approximated the dSphs as point sources [46]. In  
1004 this analysis, the dSphs are implemented as extended with J-factor distributions following those  
1005 produced by [53]. The resolution of the cited map is much finer than HAWC's angular resolution.  
1006 The vast majority of the J-factor distribution is represented on the central HAWC pixel of the dSph  
1007 spatial map. However, the neighboring 8 pixels are not negligible and contribute to our limit.

1008 Figure 6.11 shows a substantial improvement to the limit for Segue1. Fig. 6.12 however showed  
1009 identical limits. These disparities are best explained by the relative difference in their J-Factors.  
1010 Both dSphs pass almost overhead the HAWC detector, however Segue1 has the larger J-Factor  
1011 between the two. Adjacent pixels to the central pixel will therefore contribute to the limits. This is  
1012 the case for other dSph that are closer to overhead the HAWC detector.

1013 Comparison plots for all sources and the combined limit can be found in the sandbox for the  
1014 Glory Duck project.

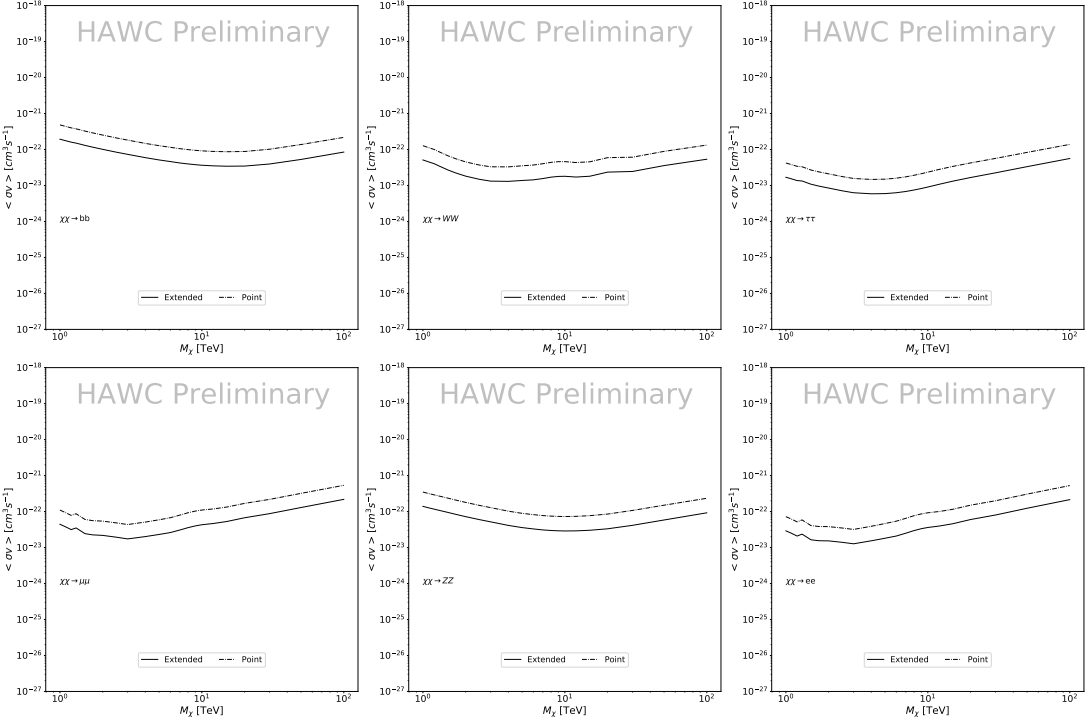


Figure 6.11 Comparisons of the combined limits at 95% confidence level for a point source analysis and extended source using [53]  $\mathcal{GS}$  J-factor distributions and PPPC [44] annihilation spectra. Shown are the limits for Segue1 which will have the most significant impact on the combined limit. 6 of the 7 DM annihilation channels are shown. Solid lines are extended source studies. Dashed lines are point source studies. Overall, the extended source analysis improves the limit by a factor of 2.

### 1015 6.7.3 Impact of Pointing Systematic

1016 During the analysis it was discovered that reconstruction of gamma-rays. Slides describing this  
 1017 systematic can be found [here](#). Shown on the presentation is dependence on the pointing systematic  
 1018 on declination. New spatial profiles were generated for every dSph and limits were computed for  
 1019 the adjusted declination.

1020 Section 6.7.3 demonstrates the impact of this systematic for all DM annihilation channels  
 1021 studied by HAWC. The impact is a tiny improvement, yet mostly identical, to the combined limits.

## 1022 6.8 J-factor distributions

### 1023 6.8.1 Numerical integration of $\mathcal{GS}$ maps

1024 It was discovered well after the HAWC analysis was completed that the published tables from  
 1025  $\mathcal{GS}$  [45] quoted median J-factors were computed in a non-trivial manner. The assumption myself

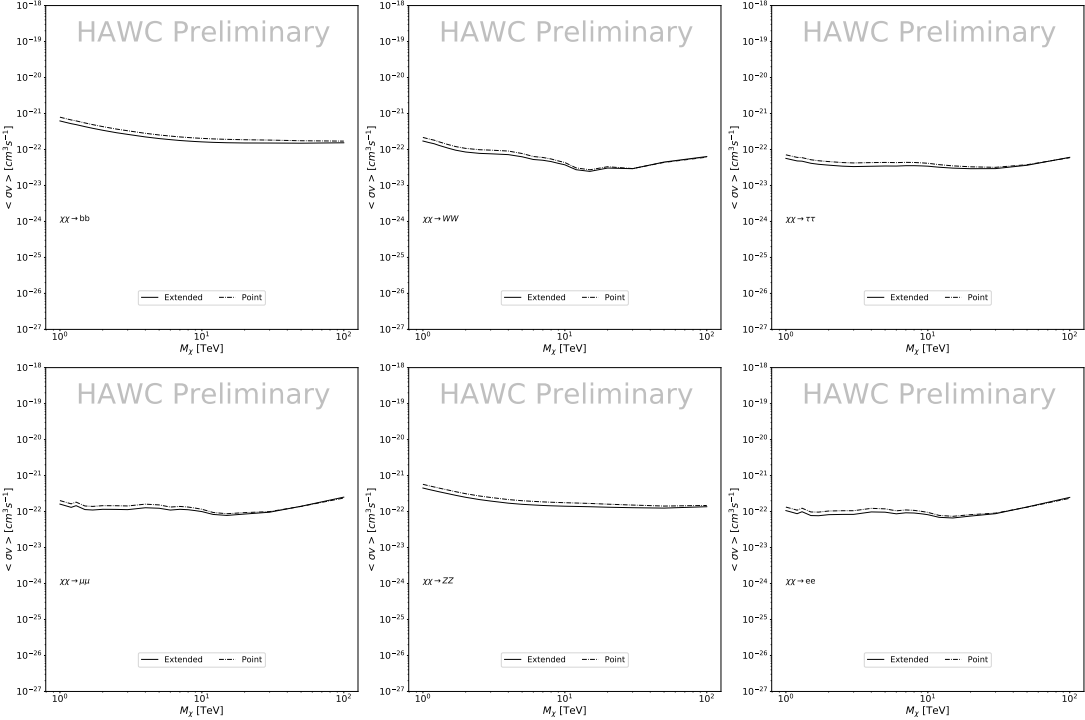


Figure 6.12 Same as Fig. 6.11 on Coma Berenices. This dSph also contributes significantly to the limit. The limits are identical in this case.

and collaborators had been that the published tables represented the  $J$ -factor as a function of  $\theta$  for the best global fit model on a per-source basis. However, this is not the case. Instead, what is published are the best fit model for each dwarf that only considers stars up to the angular separation  $\theta$ . Therefore, the model is changing for each value of  $\theta$  for each dwarf. Yet, the introduced features from unique models at each  $\theta$  are much smaller than the angular resolution of HAWC. It is not expected for these effects to impact the limits and TS greatly as a result.

Median  $J$ -factor model profiles were provided by the authors. New maps were generated and analyzed for Segue1 and Coma Berenices. Figure 6.14 shows the differential between maps generated with the method from Section 6.8.1 and from the authors of [45]. These maps were reanalyzed for all SM DM annihilation channels. Upper limits for these channels are shown in Figure 6.15

From Figure 6.15, we can see that the impact of these model difference was no substantial. The observed impact was a fractional effect which is much smaller than the impact from selecting another DM spatial distribution model as was shown in Figure 6.10.

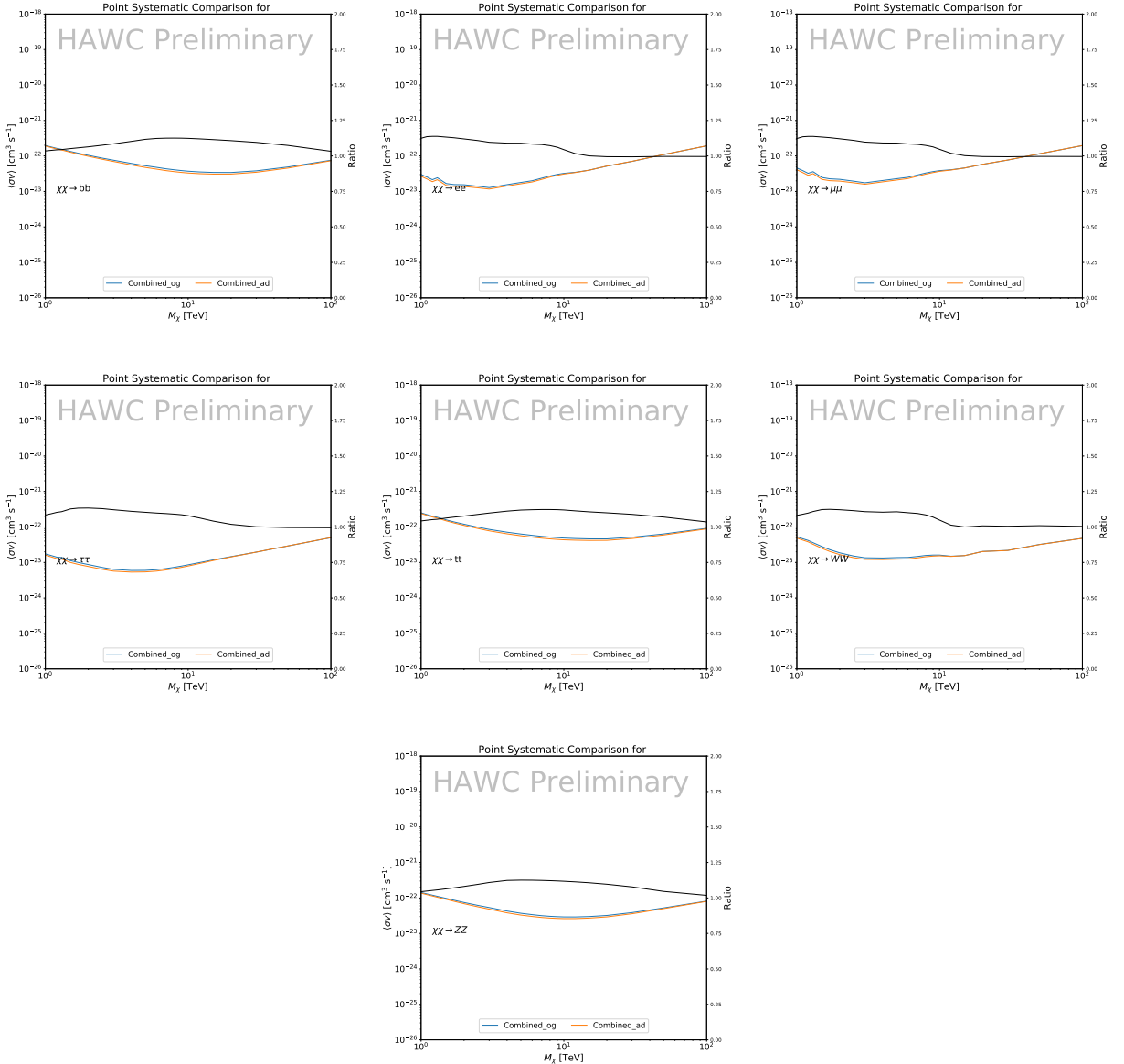


Figure 6.13 Comparison of combined limits when correcting for HAWC’s pointing systematic. All DM annihilation channels are shown. The solid black line is the ratio between published limit to the declination corrected limit. The blue solid line or “Combined<sub>og</sub>” represented the limits computed for Glory Duck. The solid orange line or “Combined<sub>ad</sub>” represented the limits computed after correcting for the pointing systematic.

## 1040 6.8.2 $\mathcal{G}\mathcal{S}$ Versus $\mathcal{B}$ spatial models

1041 We show in this appendix a comparison between the  $J$ -factors computed by Geringer-Sameth  
 1042 *et al.* [53] (the  $\mathcal{G}\mathcal{S}$  set) and the ones computed by Bonnivard *et al.* [47, 55] (the  $\mathcal{B}$  set). The  
 1043  $\mathcal{G}\mathcal{S}$   $J$ -factors are computed through a Jeans analysis of the kinematic stellar data of the selected

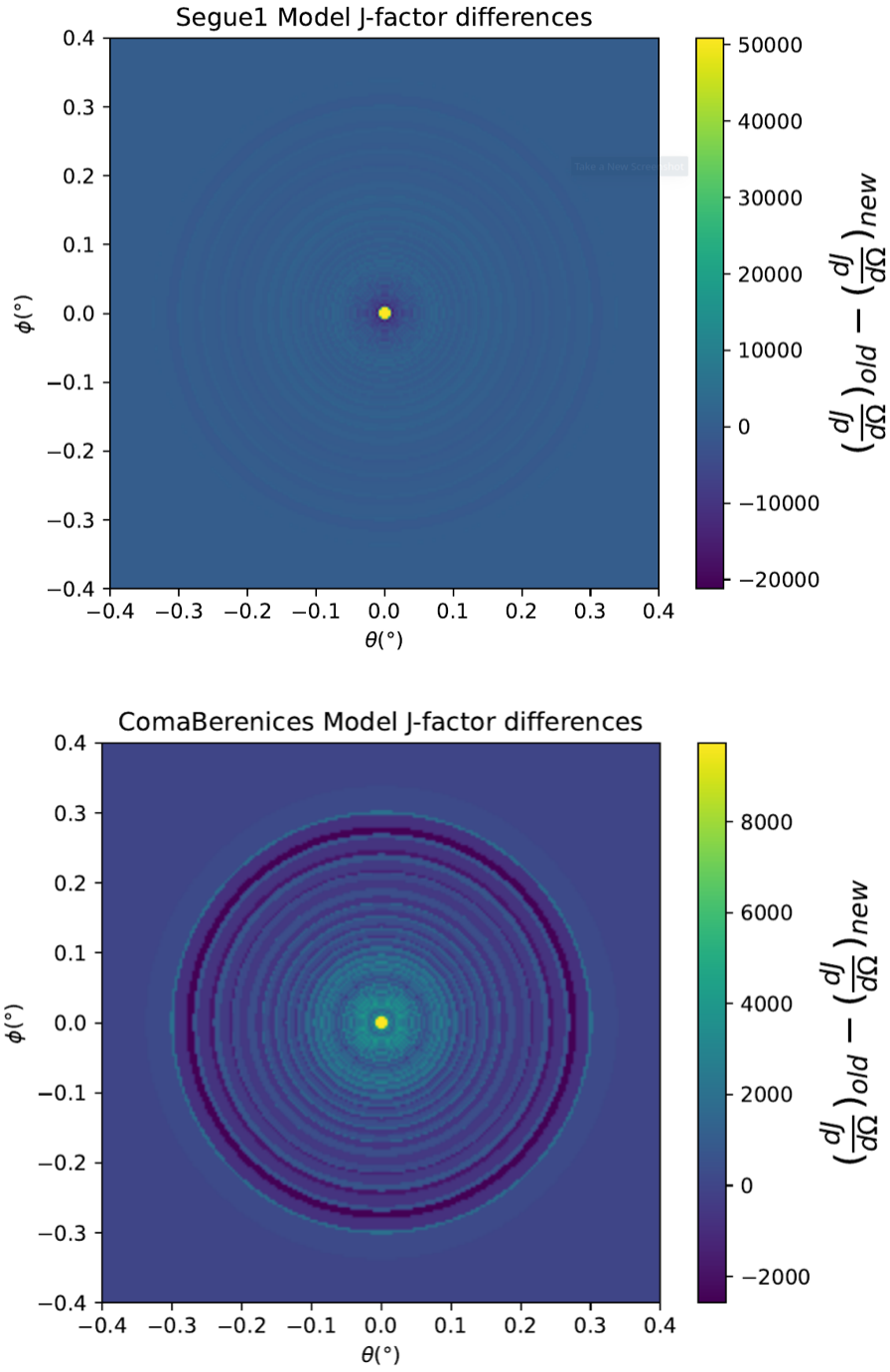


Figure 6.14 Differential map of  $dJ/\Omega$  from model built in Section 6.8.1 and profiles provided directly from authors. (Top) Differential from Segue1. (bottom) Differential from Coma Berenices. Note that their scales are not the same. Segue1 shows the deepest discrepancies which is congruent with its large uncertainties. Both models show anuli where unique models become apparent.

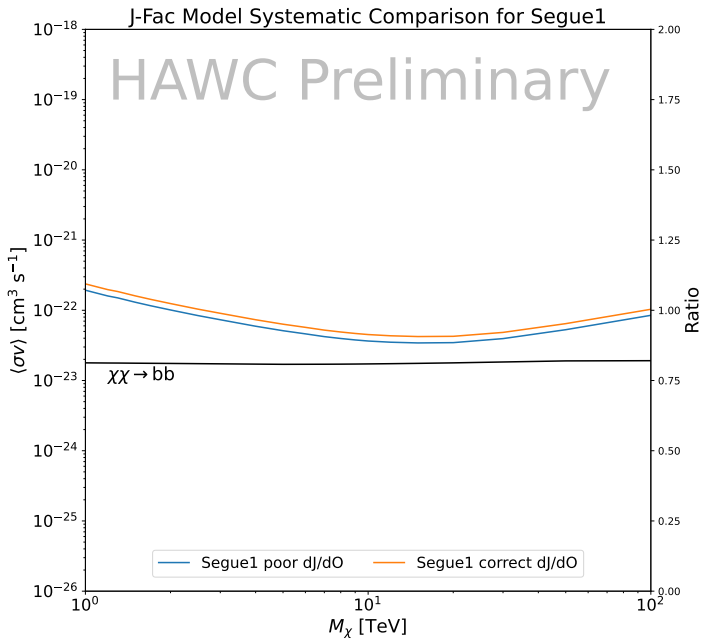
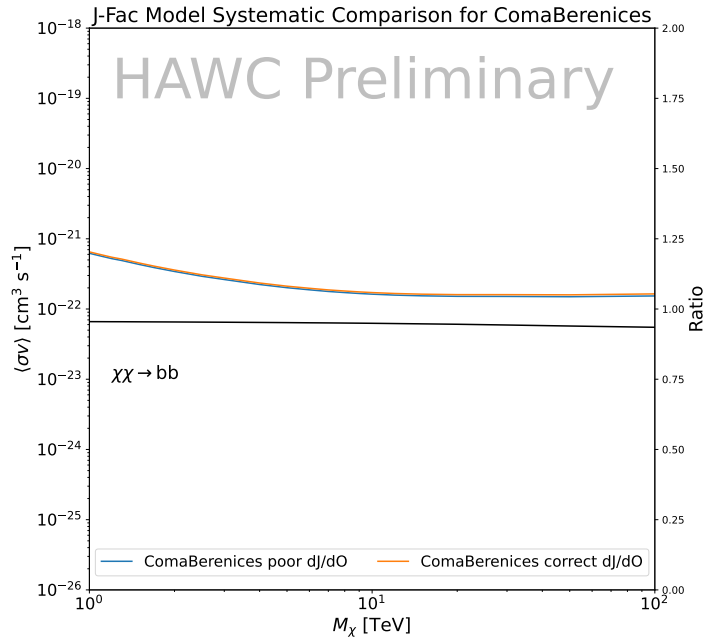


Figure 6.15 HAWC limits for Coma Berenices (top) and Segue1 (bottom) for two different map sets. Blue lines are limits calculated on maps with poor model representation. Orange lines are limits calculated on spatial profiles provided by the authors of [45]. Black line is the ratio of the poor spatial model limits to the corrected spatial models. The left y-axis measures  $\langle \sigma v \rangle$  for the blue and orange lines. The right y-axis measures the ratio and is unitless.

1044 dSphs, assuming a dynamic equilibrium and a spherical symmetry for the dSphs. They adopted  
1045 the generalized DM density distribution, known as Zhao-Hernquist, introduced by [58], carrying  
1046 three additional index parameters to describe the inner and outer slopes, and the break of the  
1047 density profile. Such a profile parametrization allows the reduction of the theoretical bias from  
1048 the choice of a specific radial dependency on the kinematic data. In other words, the increase of  
1049 free parameters with the use of the Zhao-Hernquist profile allows a better description of the mass  
1050 density distribution of dark matter.

1051 In addition, a constant velocity anisotropy profile and a Plummer light profile [59] for the stellar  
1052 distribution were assumed. The velocity anisotropy profile depends on the radial and tangential  
1053 velocity dispersion. However, its determination remains challenging since only the line-of-sight  
1054 velocity dispersion can be derived from velocity measurements. Therefore, the parametrization of  
1055 the anisotropy profile is obtained from simulated halos (see [60] for more details). They provide the  
1056 values of the  $J$ -factors of regions extending to various angular radius up to the outermost member  
1057 star.

1058 The  $\mathcal{B}$   $J$ -factors were computed through a Jeans analysis taking into account the systematic  
1059 uncertainties induced by the DM profile parametrization, the radial velocity anisotropy profile, and  
1060 the triaxiality of the halo of the dwarf galaxies. They performed a more complete study of the dSph  
1061 kinematics and dynamics than  $\mathcal{GS}$  for the determination of the  $J$ -factor. Conservative values of the  
1062  $J$ -factors where obtained using an Einasto DM density profile [61], a realistic anisotropy profile  
1063 known as the Baes & Van Hese profile [62] which takes into account that the inner regions can be  
1064 significantly non-isotropic, and a Zhao-Hernquist light profile [58].

1065 For both sets,  $J$ -factor values are provided for all dSphs as a function of the radius of the  
1066 integration region [53, 47, 55]. Table 6.1 shows the heliocentric distance and Galactic coordinates  
1067 of the twenty dSphs, together with the two sets of  $J$ -factor values integrated up to the outermost  
1068 observed star for  $\mathcal{GS}$  and the tidal radius for  $\mathcal{B}$ . Both  $J$ -factor sets were derived through a Jeans  
1069 analysis based on the same kinematic data, except for Draco where the measurements of [63] have  
1070 been adopted in the computation of the  $\mathcal{B}$  value. The computations for producing the  $\mathcal{GS}$  and  $\mathcal{B}$

1071 samples differ in the choice of the DM density, velocity anisotropy, and light profiles, for which the  
1072 set  $\mathcal{B}$  takes into account some sources of systematic uncertainties.

1073 Figure 6.16 and Figure 6.17 show the comparisons for the  $J$ -factor versus the angular radius  
1074 for each of the 20 dSphs used in this study. The uncertainties provided by the authors are also  
1075 indicated in the figures. For the  $\mathcal{GS}$  set, the computation stops at the angular radius corresponding  
1076 to the outermost observed star, while for the  $\mathcal{B}$  set, the computation stops at the angular radius  
1077 corresponding to the tidal radius.

## 1078 6.9 Discussion and Conclusions

1079 In this multi-instrument analysis, we have used observations of 20 dSphs from the gamma-ray  
1080 telescopes Fermi-LAT, H.E.S.S., MAGIC, VERITAS, and HAWC to perform a collective DM  
1081 search annihilation signals. The data were combined across sources and detectors to significantly  
1082 increase the sensitivity of the search. We have observed no significant deviation from the null, no  
1083 DM, hypothesis, and so present our results in terms of upper limits on the annihilation cross-section  
1084 for seven potential DM annihilation channels.

1085 Fermi-LAT brings the most stringent constraints for continuum channels below approximately  
1086 1 TeV. The remaining detectors dominate at higher energies. Overall, for multi-TeV DM mass,  
1087 the combined DM constraints from all five telescopes are 2-3 times stronger than any individual  
1088 telescope for multi-TeV DM.

1089 Derived from observations of many dSphs, our results produce robust limits given the DM  
1090 content of the dSphs is relatively well constrained. The obtained limits span the largest mass  
1091 range of any WIMP DM search. Our combined analysis improves the sensitivity over previously  
1092 published results from each detector which produces the most stringent limits on DM annihilation  
1093 from dSphs. These results are based on deep exposures of the most promising known dSphs with  
1094 the currently most sensitive gamma-ray instruments. Therefore, our results constitute a legacy of  
1095 a generation of gamma-ray instruments on WIMP DM searches towards dSphs. Our results will  
1096 remain the reference in the field until a new generation of more sensitive gamma-ray instruments  
1097 begin operations, or until new dSphs with higher  $J$ -factors are discovered.

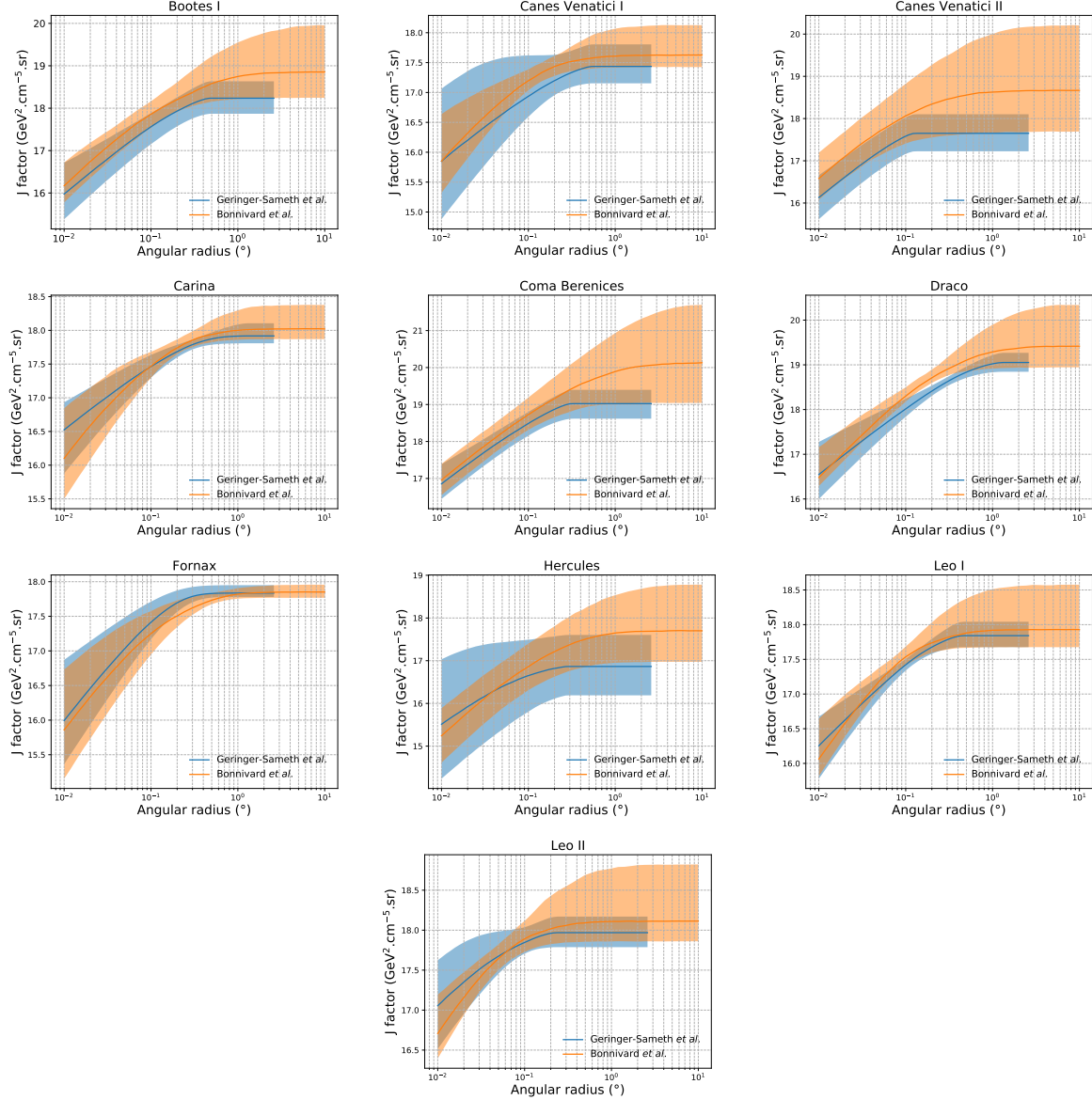


Figure 6.16 Comparisons between the  $J$ -factors versus the angular radius for the computation of  $J$  factors from Ref. [53] ( $\mathcal{GS}$  set in Table 6.1) in blue and for the computation from Ref. [47, 55] ( $\mathcal{B}$  set in Tab. 6.1) in orange. The solid lines represent the central value of the  $J$ -factors while the shaded regions correspond to the  $1\sigma$  standard deviation.

1098 This analysis serves as a proof of concept for future multi-instrument and multi-messenger  
 1099 combination analyses. With this collaborative effort, we have managed to sample over four orders  
 1100 in magnitude in gamma-ray energies with distinct observational techniques. Determining the nature  
 1101 of DM continues to be an elusive and difficult problem. Larger datasets with diverse measurement  
 1102 techniques could be essential to tackling the DM problem. A future collaboration using similar

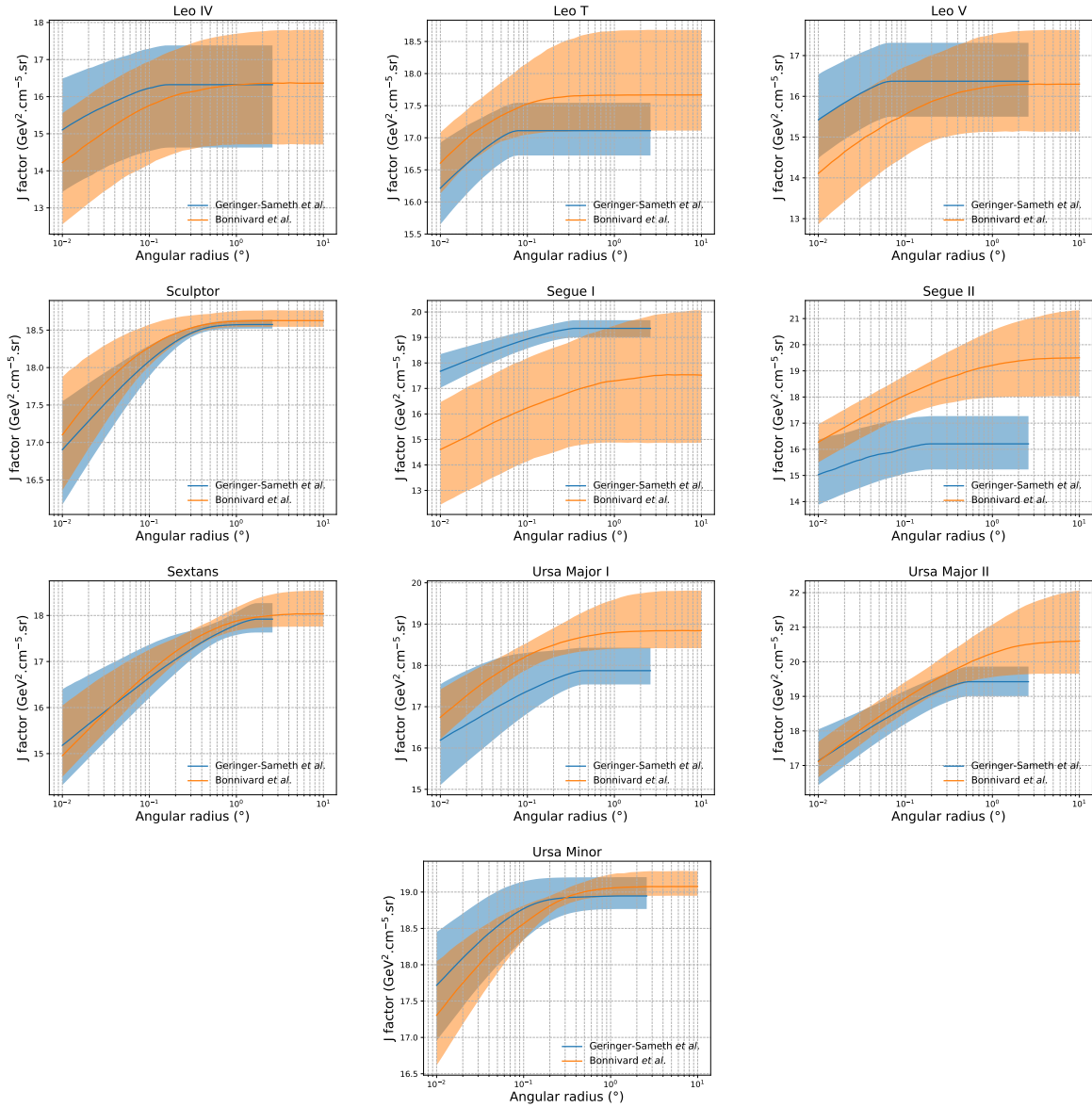


Figure 6.17 Comparisons between the  $J$ -factors versus the angular radius for the computation of  $J$  factors from Ref. [53] ( $\mathcal{GS}$  set in Tab. 6.1) in blue and for the computation from Ref. [47, 55] ( $\mathcal{B}$  set in Tab. 6.1) in orange. The solid lines represent the central value of the  $J$ -factors while the shaded regions correspond to the  $1\sigma$  standard deviation.

techniques as the ones described in this paper could grow even beyond gamma rays. The models we used for this study include annihilation channels with neutrinos in the final state. Advanced studies could aim to merge our results with those from neutrino observatories with large data sets. Efforts are already underway to add data from the IceCube, ANTARES, and KM3NeT observatories to these gamma-ray results.

1108 From this work, a selection of the best candidates for observations, according to the latest  
1109 knowledge on stellar dynamics and modelling techniques for the derivation of the  $J$ -factors on  
1110 the potential dSphs targets, is highly desirable at the time that new experiments are starting their  
1111 dark matter programs using dSphs. Given the systematic uncertainty inherent to the derivation of  
1112 the  $J$ -factors, an informed observational strategy would be to select both objects with the highest  
1113  $J$ -factors that could lead to DM signal detection, and objects with robust  $J$ -factor predictions, i.e.  
1114 with kinematic measurements on many bright stars, which would strengthen the DM interpretation  
1115 reliability of the observation outcome.

1116 This analysis combines data from multiple telescopes to produce strong constraints on astro-  
1117 physical objects. From this perspective, these methods can be applied beyond just DM searches.  
1118 Almost every astrophysical study can benefit from multi-telescope, multi-wavelength gamma-ray  
1119 studies. We have enabled these telescopes to study the cosmos with greater precision and detail.  
1120 Many astrophysical searches can benefit from multi-instrument gamma-ray studies, for which our  
1121 analysis lays the foundation.

## CHAPTER 7

### MULTITHREADING HAWC ANALYSES FOR DARK MATTER SEARCHES

#### 7.1 Introduction

HAWC's current software suite, plugins to 3ML, does not fully utilize computational advancements of recent decades. Said advancements include the proliferation of Graphical Processing Units (GPUs), and multithreading on multi-core processors. The analysis described in chapter 6 took up to 3 months of human time waiting for the full gambit of data analysis and simulation of background to run. Additionally, with the addition of a 2D binning scheme,  $f_{\text{hit}}$  and NN, the compute time is expected to grow. Although excessive computing time was, in part, from an intense use of a shared computing cluster, it was evident that there was room for improvement. In HAWC's next generation dSph DM search, I decided to develop codes that would utilize the multi-core processors on modern high performance computing clusters. The results of this work are featured in this chapter and brought a human timing improvement to computation that scales as  $1/N$  where  $N$  is the number of threads.

#### 7.2 Dataset and Background

This section enumerates the data and background methods used for HAWC's multi-threaded study of dSphs. Section 7.2.1 and Section 7.2.2 are most useful for fellow HAWC collaborators looking to replicate a multithreaded dSph DM search.

##### 7.2.1 Itemized HAWC files

- Detector Resolution: `refit-Pass5-Final-NN-detRes-zenith-dependent.root`
- Data Map: `Pass5-Final-NN-maptree-ch103-ch1349-zenith-dependent.root`
- Spectral Dictionary: `HDMspectra_dict_gamma.npy`

##### 7.2.2 Software Tools and Development

This analysis was performed using HAL and 3ML [42, 43] in Python version 3. I built software in collaboration with Michael Martin and Letrell Harris to implement the *Dark Matter Spectra from*

1146 *the Electroweak to the Planck Scale* (HDM) [64] and dSphs spatial model from [65] for HAWC  
1147 analysis. A NumPy dictionary of HDM was made for Py3. The corresponding Python3 file is  
1148 `HDMspectra_dict_gamma.npy`. These files can also be used for decay channels and tools are  
1149 provided in HDM’s [git repository](#) [64]. The analysis was performed using the Neural Network  
1150 energy estimator for Pass 5.F. A description of this estimator was provided in chapter 4. **TODO:**  
1151 **define a subsection when it’s written**, and its key improvements are an improved energy estimation  
1152 and improved sensitivities at higher zenith angles. All other software used for data analysis, DM  
1153 profile generation, and job submission to SLURM are also kept in my sandbox in the [Dark Matter](#)  
1154 [HAWC](#) project. The above repository also incorporates the model inputs used previously in Glory  
1155 Duck, described in chapter 6

1156 **7.2.3 Data Set and Background Description**

1157 The HAWC data maps used for this analysis contain 2565 days of data between runs 2104 (

1158 **TODO: Day start**) and 7476 (**TODO: day end**). They were generated from pass 5.f reconstruction.

1159 The analysis is performed using the NN energy estimator with bin list:

1160       B1C0Ea, B1C0Eb, B1C0Ec, B1C0Ed, B1C0Ee, B2C0Ea, B2C0Eb, B2C0Ec, B2C0Ed, B2C0Ee,  
1161       B3C0Ea, B3C0Eb, B3C0Ec, B3C0Ed, B3C0Ee, B3C0Ef, B4C0Eb, B4C0Ec, B4C0Ed, B4C0Ee,  
1162       B4C0Ef, B5C0Ec, B5C0Ed, B5C0Ee, B5C0Ef, B5C0Eg, B6C0Ed, B6C0Ee, B6C0Ef, B6C0Eg,  
1163       B6C0Eh, B7C0Ee, B7C0Ef, B7C0Eg, B7C0Eh, B7C0Ei, B8C0Ee, B8C0Ef, B8C0Eg, B8C0Eh,  
1164       B8C0Ei, B8C0Ej, B9C0Ef, B9C0Eg, B9C0Eh, B9C0Ei, B9C0Ej, B10C0Eg, B10C0Eh,  
1165       B10C0Ei, B10C0Ej, B10C0Ek, B10C0El

1166 Bin 0 was excluded as it has substantial hadronic contamination and poor angular resolution.

1167 Background considerations and source selection was identical to Section 6.2, and no additional  
1168 arguments are provided here. Many of the HAWC systematics explored in Section 6.7 also apply  
1169 for this DM search and are not added upon here.

1170 **7.3 Analysis**

1171 The analysis and its systematics are almost identical to Section 6.3. Importantly, we use the  
1172 same Equation (6.1) and Equation (6.2) for estimating the gamma-ray flux at HAWC from our  
1173 sources. We add on to the previous study with a search for DM decay. The flux equations for DM  
1174 decay are

$$\frac{d\Phi_\gamma}{dE_\gamma} = \frac{1}{4\pi\tau m_\chi} \frac{dN_\gamma}{dE_\gamma} \times \int_{\text{source}} d\Omega \int_{l.o.s} \rho_\chi dl(r, \theta') \quad (7.1)$$

1175 with a new quantity, the  $D$  factor, defined as

$$D = \int d\Omega \int_{l.o.s} dl \rho_\chi(r, \theta') \quad (7.2)$$

1176 Software was written to accomodate DM decay from dSphs, however decay profiles were not  
1177 received from  $\mathcal{L}\mathcal{S}$  by the time of writing this tehsis.

1178 **7.3.1  $\frac{dN_\gamma}{dE_\gamma}$  - Particle Physics Component**

1179 For these spectra, we import HDM with Electroweak (EW) corrections and additional correc-  
1180 tions for neutrinos above the EW scale [64]. The spectrum is implemented as a model script in  
1181 astromodels for 3ML. A comprehensive description of EW corrections and neutrino considerations  
1182 are provided later in **TODO: refeance MM nu duck**.

1183 Figure 7.1 demonstrates the impact of changes from HDM on DM annihilation to W bosons.  
1184 A class in astromodels was developed to include HDM and is aptly named **HDMspectra** within  
1185 **DM\_models.py**. The SM DM annihilation channels studied here are  $\chi\chi \rightarrow:$

1186  $e^+e^-, \mu^+\mu^-, \tau^+\tau^-, b\bar{b}, t\bar{t}, gg, W^+W^-, ZZ, c\bar{c}, u\bar{u}, d\bar{d}, s\bar{s}, \nu_e\bar{\nu}_e, \nu_\mu\bar{\nu}_\mu, \nu_\tau\bar{\nu}_\tau, \gamma\gamma, hh.$

1187 For  $\gamma\gamma$  and  $ZZ$ , a substantial fraction of the signal photons are expected to have total energy equal  
1188  $m_\chi$  [64]. This introduces a  $\delta$ -function that is much narrower than the energy resolution of the  
1189 HAWC detector. To ensure that this feature is not lost in the likelihood fits, the 'line' feature is  
1190 convolved with a gaussian kernel with a  $1\sigma$  width of  $0.05 \cdot m_\chi$  and total kernel window of  $\pm 4\sigma$ .  
1191 This difers from HAWC's previous line study where 30% of HAWC's energy resolution was used  
1192 for the kernel [66]. The NN energy estimator's strength compared to  $f_{\text{hit}}$  at low gamma-ray energy

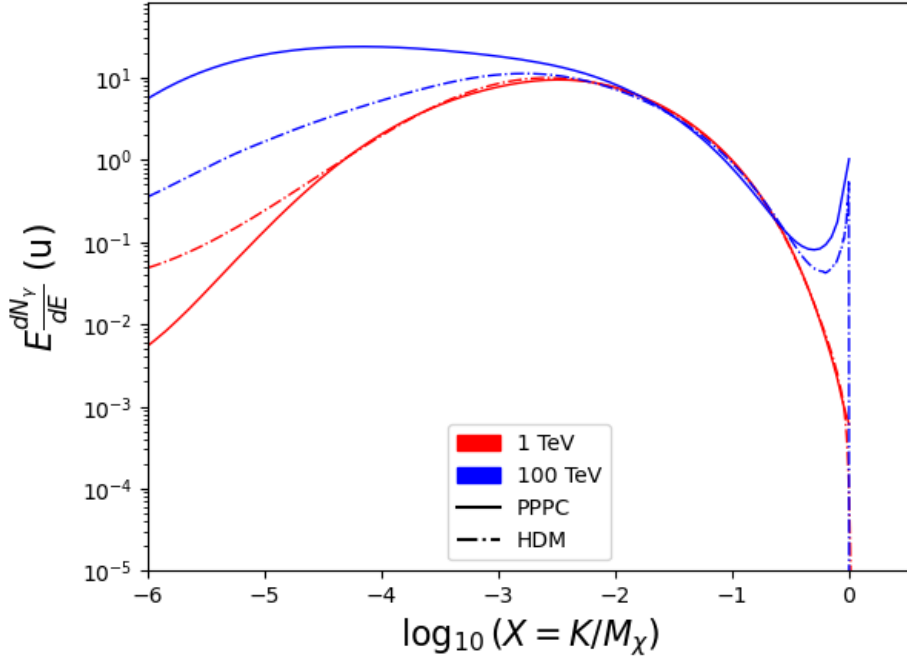


Figure 7.1 Difference between spectral hypotheses from PPPC [44] and HDM [64]. Shown is the expected DM annihilation spectrum for  $\chi\chi \rightarrow W^-W^+$ . Solid lines are spectral models with EW corrections from the PPPC. Dash-dot lines are spectral models from HDM. Red lines are models for  $M_\chi = 1$  TeV. Blue lines represent models for  $M_\chi = 100$  TeV.

enables smaller resolutions in addition to low energy tails in the spectral models [64].  $\chi\chi \rightarrow \gamma\gamma$  and ZZ spectral hypotheses are shown in Figure 7.2. Spectral models for the remaining annihilation channels are plotted for each  $m_\chi$  in Figure B.1.

### 7.3.2 J and D- Astrophysical Components

The J-factor profiles for each source are imported from Louis Strigari et al. (referred to with  $\mathcal{LS}$ ) [65]. Profiles in  $\frac{dJ}{d\Omega}(\theta)$  up to  $\theta = 0.5^\circ$  were provided directly from the authors. Map generation from these profiles were almost identical to Section 6.3.2 except that a higher order trapezoidal integral was used for the normalization of the square, uniformly-spaced map:

$$p^2 \cdot \sum_{i=0}^N \sum_{j=0}^M w_{i,j} \frac{d\mathcal{K}}{d\Omega}(\theta_{i,j}, \phi_{i,j}) \quad (7.3)$$

$\mathcal{K}$  is either  $J$  or  $D$  for the spatial distributions of annihilation or decay respectively.  $p$  is the angular side of one pixel in the map.  $w_{i,j}$  is a weight assigned the following ways:

$w_{i,j} = 1$  if  $(\theta_{i,j}, \phi_{i,j})$  is fully within the region of integration

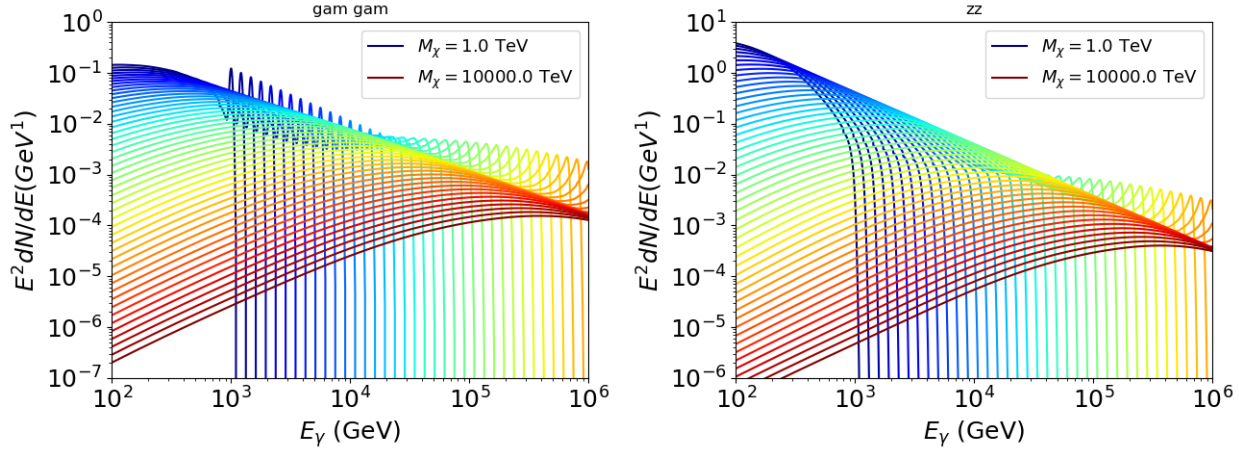


Figure 7.2 Photon spectra for  $\chi\chi \rightarrow \gamma\gamma$  (left) and  $\chi\chi \rightarrow ZZ$  (right) after gaussian convolution of line features. Both spectra have  $\delta$ -features at photon energies equal to the DM mass. Bluer lines are annihilation spectra with lower DM mass. Redder lines are spectra from larger DM mass. All Spectral models are sourced from the Heavy Dark Matter models [64]. Axes are drawn roughly according to the energy sensitivity of HAWC.

1204        $w_{i,j} = 1/2$  if  $(\theta_{i,j}, \phi_{i,j})$  is on an edge of the region of integration

1205        $w_{i,j} = 1/4$  if  $(\theta_{i,j}, \phi_{i,j})$  is on a corner of the region of integration

1206   Figure 7.3 shows the median and  $\pm 1\sigma$  maps used as input for DM annihilation studied by  $\mathcal{LS}$ .

### 1207   **7.3.3 Source Selection and Annihilation Channels**

1208   HAWC's sources for this multithreaded analysis include Coma Berenices, Draco, Segue 1, and  
 1209   Sextans  $\mathcal{LS}$  observes up to 43 sources in its publication, however only 4 of the best fit profiles were  
 1210   provided at the time this thesis was written. A full description of each source used in this analysis  
 1211   is found in Table 7.1.

1212   This analysis improves on chapter 6 in the following ways. Previously, the particle physics  
 1213   model used for gamma-ray spectra from DM annihilation was from the PPPC [44] which missed  
 1214   important considerations relevant for the neutrino sector. HDM is used to account for this shortfall  
 1215   [64]. HDM also models DM to the Planck scale which permits HAWC to probe PeV scale DM.  
 1216   For this study, we sample DM masses: 1 TeV - 10 PeV with 6 mass bins per decade in DM mass.  
 1217   In the case of line spectra ( $\chi\chi \rightarrow \gamma\gamma$ , or  $ZZ$ ), we double the mass binning to 12 DM mass bins  
 1218   per decade in DM mass. A larger source catalog is used that uses a Navarro–Frenk–White (NFW)

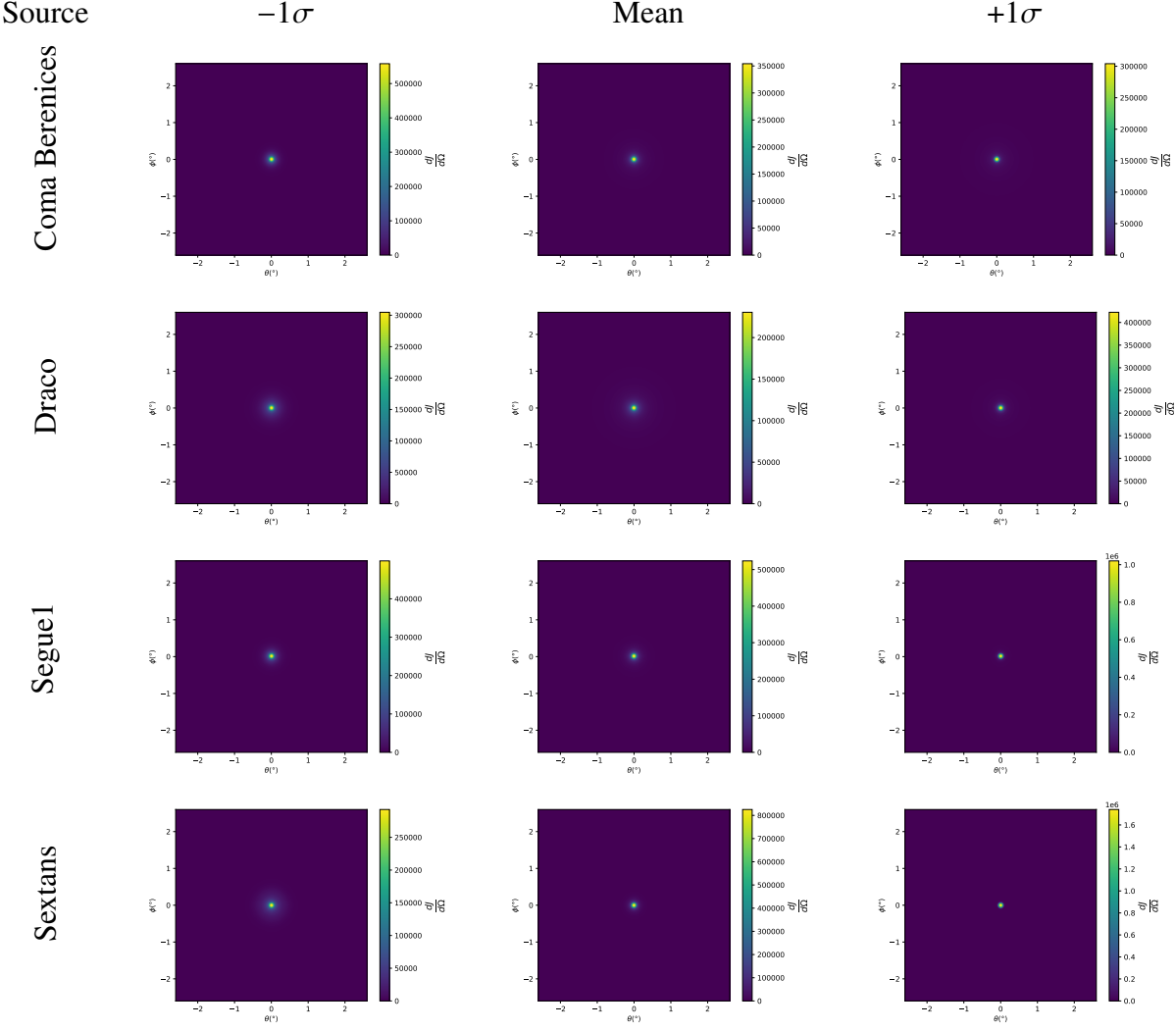


Figure 7.3  $\frac{dJ}{d\Omega}$  maps for Coma Berenices, Draco, Segue1, and Sextans. Columns are divided for the  $\pm 1\sigma$  uncertainties in  $dJ/d\Omega$  around the mean value from  $\mathcal{LS}$  [65]. Origin is centered on the specific dwarf spheroidal galaxies (dSph).  $\theta$  and  $\phi$  axes are the angular separation from the center of the dwarf

1219 spatial DM distribution from  $\mathcal{LS}$  [65]. Because NFW has fewer parameters than what is used  
 1220 for  $\mathcal{GS}$ ,  $\mathcal{LS}$  is able to fit ultra-faint dwarves, expanding the number of sources available for DM  
 1221 searches. Finally, the gamma-ray ray dataset is much larger. The study performed here analyzes  
 1222 2565 days of data compared to 1017 days analyzed in chapter 6.

## 1223 7.4 Likelihood Methods

1224 These are identical to Section 6.4.1 and no additional changes are made to the likelihood. Bins  
 1225 in this analysis are expanded to include HAWC’s NN energy estimator.

1226 **7.5 Computational Methods: Multithreading**

1227 Previously, as in Section 6.3, the likelihood was minimized for one model at a time. One  
 1228 model in this case representing a DM annihilation channel, DM mass, and dSph. In an effort  
 1229 to conserve human and CPU time, jobs submitted for high performance computing contained a  
 1230 list of DM masses to iterate over for likelihood fitting. Jobs were then trivially parallelized for  
 1231 each permutation of the two lists: CHANS (SM annihilation channel) and SOURCES (dSph spatial  
 1232 templates). The lists for CHANS and SOURCES are found in Section 7.3.1 and Table 7.1, respectively.  
 1233 Initially, 11 DM mass bins were serially sampled for one job defined by a [SM channel, dSph] set.  
 1234 Computing the likelihoods would take between 1.5 to 2 hrs, stocastically, for a job. We expect to  
 1235 compute likelihoods for data and 300 Poisson background trials. The estimated CPU time based on  
 1236 the above for all SM annihilation channels (17) and 25 sources (all  $\mathcal{LS}$  sources withing HAWC's  
 1237 field of view) amounted to 127,925 jobs. In total, 1,407,175 likelihood fits and profiles would be  
 1238 computed for the 11 mass bins we wished to study. The estimated CPU time ranged between 10k  
 1239 CPU days - 8k CPU days. Human time is more challenging to estimate as job allocation is stochastic  
 1240 and highly dependant on what other users are submitting, yet it is unlikely that all jobs would run  
 1241 simultaneously. Therefore we can expect human time to be about as long as was seen in chapter 6  
 1242 which was on the order of months to fully compute on a smaller analysis. A visual aid to describe  
 1243 how jobs were organized is provided in Figure 7.4.

Name	Distance (kpc)	$l, b$ ( $^{\circ}$ )	$\log_{10} J$ ( $\mathcal{LS}$ set) $\log_{10}(\text{GeV}^2\text{cm}^{-5}\text{sr})$
Coma Berenices	44	241.89, 83.61	$19.00^{+0.36}_{-0.35}$
Draco	76	86.37, 34.72	$18.83^{+0.12}_{-0.12}$
Segue I	23	220.48, 50.43	$19.12^{+0.49}_{-0.58}$
Sextans	86	243.50, 42.27	$17.73^{+0.13}_{-0.12}$

Table 7.1 Summary of the relevant properties of the dSphs used in the present work. Column 1 lists the dSphs. Columns 2 and 3 present their heliocentric distance and galactic coordinates, respectively. Column 4 reports the  $J$ -factors of each source given from the  $\mathcal{LS}$  studies and estimated  $\pm 1\sigma$  uncertainties. The values  $\log_{10} J$  ( $\mathcal{LS}$  set) [65] correspond to the mean  $J$ -factor values for a source extension truncated at  $0.5^{\circ}$ .

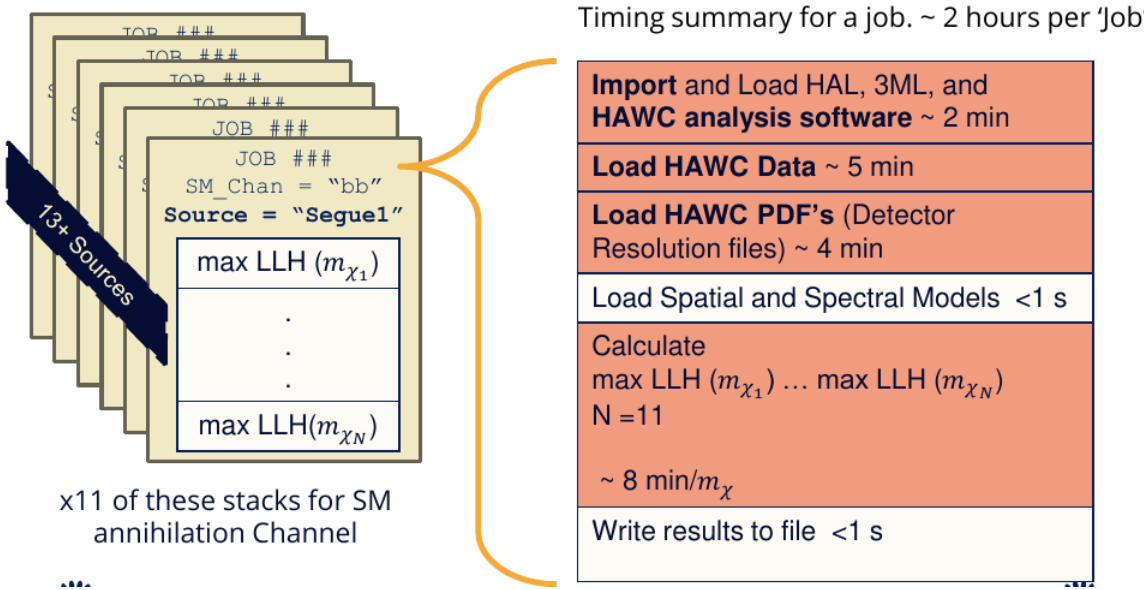


Figure 7.4 Infographic on how jobs and DM computation was organized in Section 6.3. Jobs were built for each permutation of CHANS and SOURCES shown by the left block in the figure. Each job, which took on the order 2 hrs to compute, had the following work flow: 1. Import HAWC analysis software, 2 min to run. 2. Load HAWC count maps, 5 min to run. 3. Load HAWC energy and spatial resolutions, 4 min. 5. Load DM spatial source templates and spectral models, less than 1 s. 6. Perform likelihood fit on data and model, about 8 min per DM mass. 7. Write results to file, less than 1s.

The computational needs for this next generation DM analysis are extreme and is unlike other analyses performed on HAWC. It became clear that there was a lot to gain from optimizing how the likelihoods are computed. This section discusses how multi-threading was applied to solve and reduce HAWC's computing of likelihoods for large parameter spaces like in DM searches.

### 7.5.1 Relevant Foundational Information

The profiling of the likelihood for HAWC is done via gradient descent where the normalization of Equation (6.1) (linearly correlated with  $\langle \sigma v \rangle$ ) is rescaled in the descent. Additionally, we sample the likelihood space for a defined list of  $\langle \sigma v \rangle$ 's described in Section 6.4.2. The time to compute these values is not predictable or consistent because many variables can change across the full model-space. comprehensively, these variables are:

- $m_{\chi}$  : DM rest mass
- CHAN : DM SM annihilation channel.

1256 • SOURCE : dSph within HAWC's field of view. This involves a spatial template AND coordinate  
1257 in HAWC data.

1258 •  $\langle\sigma v\rangle$  : Effectevly the flux normalization and free parameter in the likelihood fit.

1259 Therefore, we develop an asynchronous, functional-parallel coding pattern. Asynchronous meaning  
1260 that the instructions and computing within a function are independent and permitted to be out of sync  
1261 with sibling computations. Functional-parallel meaning that instructions are the subject of parral-  
1262 lelization rather than threading the likelihood computation. This is close to trivial parametrization  
1263 seen in Figure 7.4 except that we seek to consolidate the loading stages (software, data, and detector  
1264 resolution loading). Reducing the total instances of loading stages and distributing access to the  
1265 reduced loads across multiple asynchronous threads is expected to reduce serial processing time and  
1266 the overhead implicit to each job in addition to saving human time.

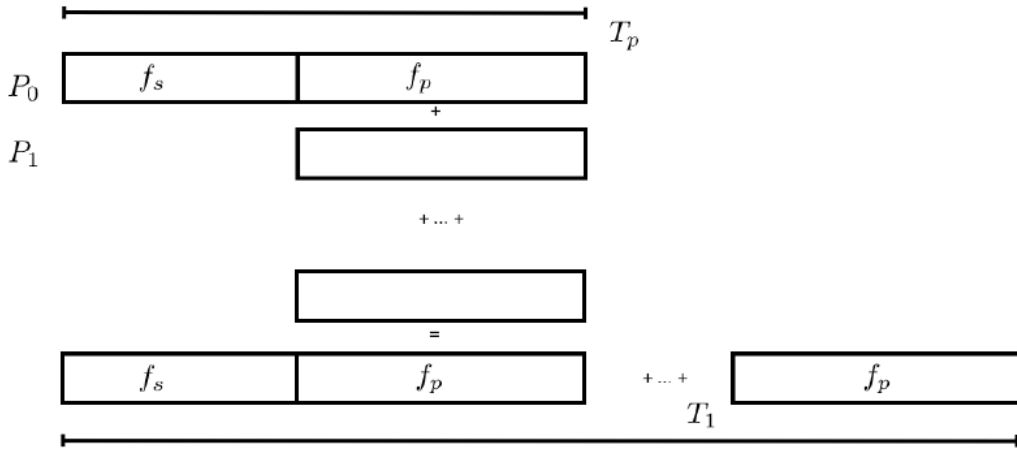


Figure 7.5 Graphic of Gustafson parallel coding pattern.  $f_s$  is the fraction of a program, in time, spent on serial computation.  $f_p$  is the fraction of computing time that is parallelizable.  $T_p$  is the total time for a parallel program to run.  $T_1$  is the total time for a parallel program to run if only 1 processor is allocated.  $P_N$  is the  $N$ -th processor where it's row is the computation the processor performs. The Gustafson pattern is most similar to what is implemented for this analysis. Figure is pulled from [67].

1267 We need a way to measure and compare the expected speedup and efficiency gain for this  
1268 asynchronous coding pattern. I pull inspiration for timing measurement from [67] and use *Amdahl's  
1269 law with hybrid programming*. Hybrid programming meaning that the computation is a mix of

1270 distributed and shared memory programming. If we assume the code is fully parallelizable over  $p$   
1271 processors and  $c$  threads, the ideal speedup is simply  $pc$  and ideal run-time is  $T_1/(pc)$ .  $T_1$  is the  
1272 total time for a parallel program to run if only 1 processor is allocated. However, the coding pattern  
1273 contains some amount of unavoidable serial computation, as shown in Figure 7.5. In our case, the  
1274 run time is estimated to be

$$T_{p,c} = \frac{T_1}{pc} (1 + F_s(c - 1)). \quad (7.4)$$

1275  $F_s$  is the fraction of CPU time dedicated to serial computation. The expected speedup is

$$S_{p,c} \equiv \frac{T_1}{T_{p,c}} = \frac{pc}{1 + F_s(c - 1)}. \quad (7.5)$$

1276 From Equation (7.5), we can see that the speed up scales with  $p/F_s$ . We are free to minimize  
1277  $F_s$  asymptotically by enlarging the total models that are submitted to the thread pool, thereby  
1278 shrinking the CPU fraction dedicated to serial operation. We are also free to define exactly how  
1279 many threads and processors we utilize, yet eventually hit a hard cap at the hardware available on  
1280 our computing cluster. HAWC uses Intel Xeon processors with 48 cores and 96 threads. This  
1281 means when N-threads ( $c$ ) are defined,  $N \bmod 2$  cores ( $p$ ) are needed. We see that a successful  
1282 code scales well as the expected speedup is inversely correlated with  $F_s$ . As the total number of  
1283 models sampled grows, the speedup will also.

### 1284 7.5.2 Implementation

1285 The multithreaded code was written in Python3 and is documented in the `dark_matter_hawc`  
1286 [repository](#) within the script named `mpu_analysis.py`. A version of the script as of April 25  
1287 **TODO: make sure to update on this date** is also provided in Section B.2 It has many dependancies  
1288 including the HAWC analysis software. Figure 7.6 displays the workflow of a job with 3 threads.  
1289 Within a job, SOURCE is kept fixedh . CHAN(S) remains 17 elements long. More  $m_\chi$  are sampled  
1290 from 11 bins up to 49 (for  $\gamma\gamma$  and ZZ) and 25 (for remaining CHANS) which amounts to 12 or 6  
1291 mass bins per decade. The DM mass,  $m_\chi$ , and SM annihilation channels, CHANS, are permuted into  
1292 a 473 element list which is split evenly across N threads where N ranges between 5 - 16. Within a  
1293 thread, for each  $m_\chi$ -CHAN tuple, 1001  $\langle\sigma v\rangle$  values are sampled in the likelihood, and the value of

Timing summary for a multi-threaded job.

Import and Load HAL, 3ML, and <b>HAWC analysis software</b> ~ 2 min		
Load HAWC Data ~ 5 min		
Load HAWC PDF's (Detector Resolution files) ~ 4 min		
Load Spatial Model < 1s		
Load Spectra Models <1 s	Load Spectra Models <1 s	Load Spectra Models <1 s
Calculate max LLH (Chan_0, $m_{\chi_1}$ ) ... max LLH (Chan_?, $m_{\chi_N}$ ) N = TOTAL/N_THREADS  ~ 8 min/Spec_model	Calculate max LLH (Chan_?, $m_{\chi_1}$ ) ... max LLH (Chan_?, $m_{\chi_N}$ ) N = TOTAL/N_THREADS  ~ 8 min/Spec_model	Calculate max LLH (Chan_?, $m_{\chi_1}$ ) ... max LLH (Chan_?, $m_{\chi_N}$ ) N = TOTAL/N_THREADS  ~ 8 min/Spec_model
Write results to file <1 s	Write results to file <1 s	Write results to file <1 s
Join Threads and terminate < 1s		

Figure 7.6 Task chart for one multi-threaded job developed for this project. Green blocks indicate a shared resource across the threads AND computation performed serially. Red blocks indicate functional parallel processing within each thread. 3 threads are represented here, yet many more can be employed during the full analysis. Jobs are defined by the SOURCE as these require unique maps to be loaded into the likelihood estimator. The  $m_{\chi}$ , CHAN, and  $\langle \sigma v \rangle$  variables are entered into the thread pool and allocated as evenly as possible across the threads.

1294  $\langle \sigma v \rangle$  that maximizes the likelihood is found. Although rare, fits that failed are handled on a case  
1295 by case basis.

### 1296 7.5.3 Performance

M Tasks	$T_{p,c}$ (hr:min:s)			
	$T_{1,1}$	$T_{1,2}$	$T_{1,8}$	$T_{1,16}$
50	1:40:37.5	0:52:43.7	0:19:13.8	0:13:44.0
74	2:22:30.0	1:15:00.6	0:25:21.3	0:15:49.8
100	(3:07:51.9)	1:40:10.5	0:30:44.4	0:20:01.4
200	(6:02:20.6)	-	1:00:32.0	0:30:35.0
473	(13:58:40.3)	-		1:09:42.9

Table 7.2 Timing summaries for analyses for serial and multithreaded processes. M tasks is the number of functional-parallel tasks ran for the computation.  $T_{p,c}$  is a single run time in hours:minutes:seconds for runs utilizing  $p$  nodes and  $c$  threads. Runs are run interactively on the same computer to maximize consistency. Empty entries are indicated with '-'. (·) entries are estimated entries extrapolated from data earlier in the column.

1297 We see a tremendous reduction to human time waiting for our dSph analyses to run. Table 7.2

1298 shows the timing summaries for analyses of different sizes and thread counts. Additionally, the  
 1299 efficiency gained when consolidating the serial loading of data is also apparent in our ability to  
 1300 study many more tasks in about the same amount of wall time as a smaller serial computation. Trials  
 1301 represented in the table were run on an AMD Opteron® processor 6344 with 48 cores, 2 threads  
 1302 per core; 2.6 GHz clock. This is not the same architecture used for analysis on the computing  
 1303 cluster however they are similar enough that results shown here are reasonably representative of  
 1304 computing on the HAWC computing cluster. I use the Tab. 7.2 for the inferences and conclusions  
 1305 in the following paragraphs.

1306 First, we want to find  $T_s$ , the time of serial computation. From Fig. 7.5, the timing for our  
 1307 coding pattern can be written as

$$T_s + Mt_p = T_{1,1}^M. \quad (7.6)$$

1308  $M$  is the number of functional-parallel tasks (represented as column 1 of Tab. 7.2), and  $t_p$  is the  
 1309 average time to complete a single parallel task.  $T_{1,1}^M$  is the total time for a parallel program to run if  
 1310 only 1 processor is allocated for  $M$  parallel task. With two runs of different  $M$  ( $M1$  and  $M2$ ), we  
 1311 can use a system of equations to derive

$$T_s = T_{1,1}^{M1} - M1 \left( \frac{T_{1,1}^{M1} - T_{1,1}^{M2}}{M1 - M2} \right). \quad (7.7)$$

1312 We also extract  $t_p$  using the same methods:

$$t_p = \frac{T_{1,1}^{M1} - T_{1,1}^{M2}}{M1 - M2}. \quad (7.8)$$

1313 From Tab. 7.2, we set  $M1 = 50$  and  $M2 = 74$  and take their corresponding  $T_{1,1}$  from the table to  
 1314 calculate  $T_s$  and  $t_p$ .

$$T_s = 803.1\text{s} \text{ and } t_p = 104.6\text{s} \quad (7.9)$$

1315 Now, we have specific estimation for the fraction of serial computing time,  $F_s$ :

$$F_s = \frac{803.1}{803.1 + 104.6 \cdot M}. \quad (7.10)$$

1316 The maximum  $M$  for this study is 473 which evaluates Eq. (7.10):  $F_s = 0.016$  or 1.6% of computing  
 1317 time. Table 7.3 shows the resulting speedups.

M Tasks	$F_s$	$S_{1,2}$	$S_{1,8}$	$S_{1,16}$
50	1.33 E-1	1.90 [1.76]	5.23 [4.14]	6.35 [5.34]
74	9.40 E-2	1.90 [1.83]	5.62 [4.82]	9.00 [6.64]
100	7.13 E-2	1.88 [1.87]	6.11 [5.34]	9.38 [7.73]
200	3.70 E-2	- [1.93]	5.98 [6.36]	11.85 [10.29]
473	1.60 E-2	[1.97]	[7.20]	[12.91]

Table 7.3 Speed up summaries for analyses for serial and multithreaded processes. M tasks is the number of functional-parallel tasks ran for the computation.  $S_{p,c}$  is a single speedup comparison for runs utilizing  $p$  nodes and  $c$  threads. [·] are the estimated speedups calculated from Tab. 7.2, Eq. (7.10), and Eq. (7.5). Empty entries are indicated with '-'.

1318 We see a speedup that exceeds expectations from Eq. (7.5) for real trail runs. **TODO: reflect**

1319 **on results when the tables are totally filled in.** We also see that there are diminishing returns as  
 1320 the number of threads increases. For small jobs with large  $c$ , both the expected and observed  
 1321 speedup are significantly smaller than  $c$ . One thing not considered in Eq. (7.5) is the time incurred  
 1322 via communication latency. Communication latency increases with the number of threads and  
 1323 contributes to diminishing returns. Therefor, these results are not conclusive. Each entry in  
 1324 Tab. 7.2 represent only one run of the script and therefore the data are not precise and lacks the  
 1325 full scope of timing costs. Yet, they do give us a good idea of what HAWC gains in multithreading  
 1326 analysis software. We see very clearly that there is a lot to gain, and this new coding pattern will  
 1327 expand HAWC's analysis capabilities.

1328 **7.6 Analysis Results**

1329 **TODO: talk about the results**

1330 We were not able to generate background trials in time of writing this thesis. These are not  
 1331 shown and are an immediate next step for this analysis before publication.

1332 We did not see DM, but we did see some interesting excesses in the 10 Tev range at order  $2\sigma$ .

1333 Draco was not included as the PDF of some of our analysis bins were wider than what is reasonable  
 1334 for a point source analysis. Draco is at a high zenith for HAWC, so the effort required to include it  
 1335 was not justified by the benefits.

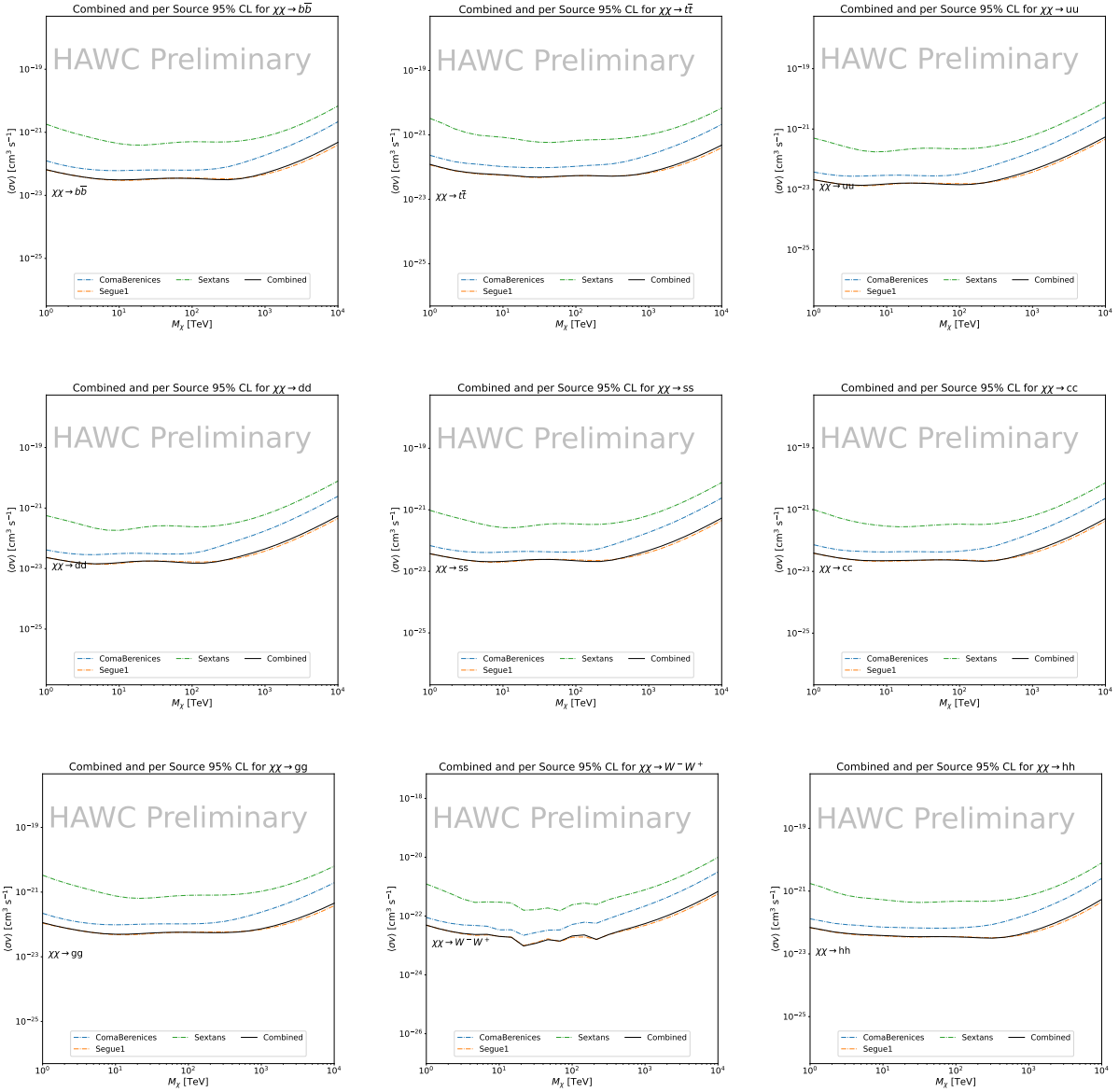


Figure 7.7 HAWC upper limits at 95% confidence level on  $\langle\sigma v\rangle$  versus DM mass for  $\chi\chi \rightarrow b\bar{b}$ ,  $t\bar{t}$ ,  $u\bar{u}$ ,  $d\bar{d}$ ,  $s\bar{s}$ ,  $c\bar{c}$ ,  $gg$ ,  $W^-W^+$ , and  $hh$ . Limits are with  $\mathcal{LS}$   $J$ -factors [65]. The solid line represents the observed combined limit. Dashed lines represent limits from individual dSphs.

## 1336 7.7 Systematics

1337 These are identical to what was performed earlier in Glory Duck, Section 6.7. We are also  
 1338 sensitive to the choice in spatial template, and this was explored in Section 6.7.2 and Section 6.8.2.  
 1339  $\mathcal{LS}$  also provided the uncertainty on their mean spatial models. We perform a study on the  
 1340  $\pm 1\sigma$  spatial templates and show corresponding confidence limits in [TODO: link to figure](#)

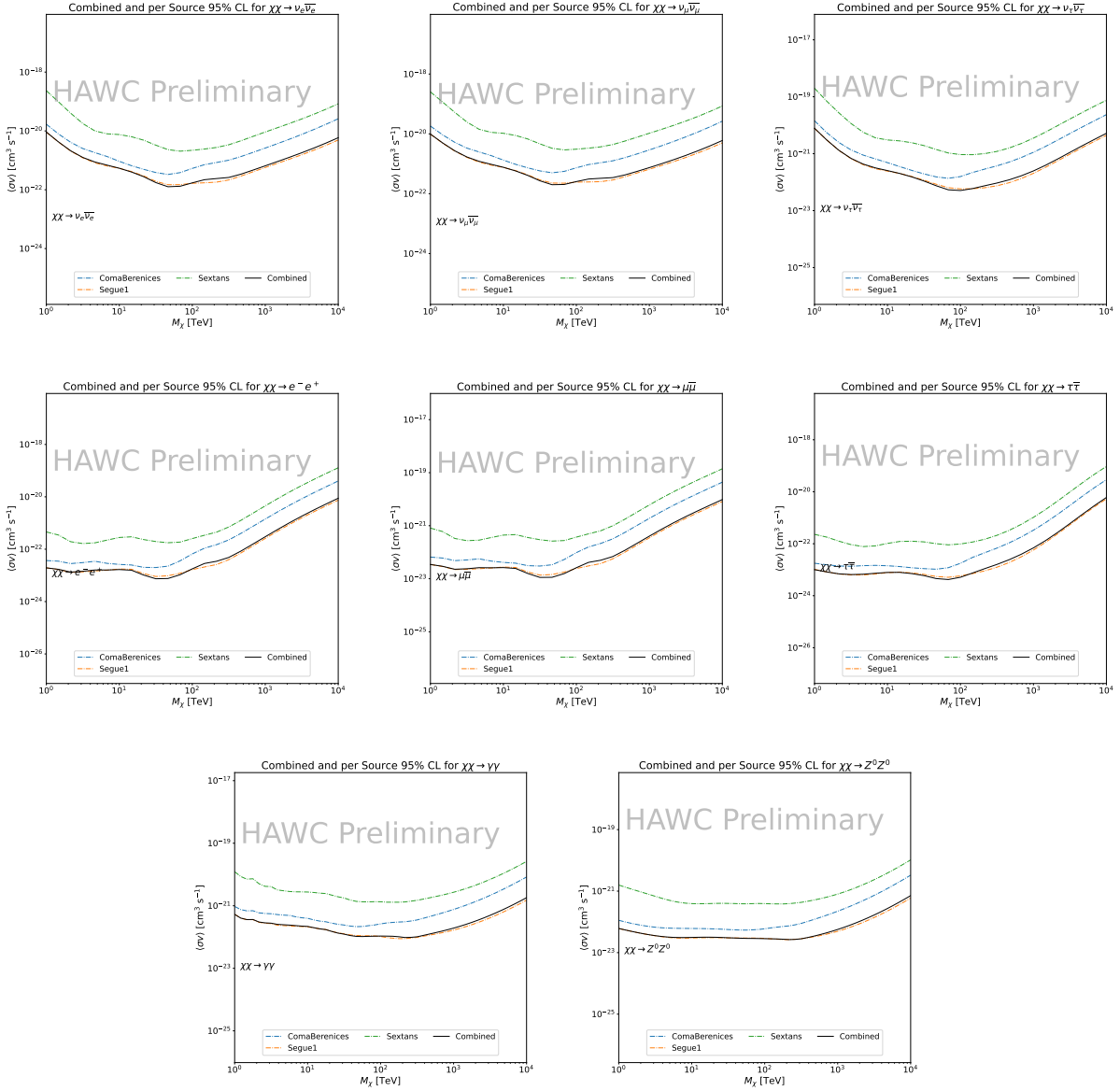


Figure 7.8 HAWC upper limits at 95% confidence level on  $\langle\sigma v\rangle$  versus DM mass for  $\chi\chi \rightarrow \nu_e \bar{\nu}_e$ ,  $\nu_\mu \bar{\nu}_\mu$ ,  $\nu_\tau \bar{\nu}_\tau$ ,  $e^- e^+$ ,  $\mu \bar{\mu}$ ,  $\tau \bar{\tau}$ ,  $\gamma \gamma$  and  $ZZ$ . Limits use  $\mathcal{L}S J$  factors [65]. The solid line represents the observed combined limit. Dashed lines represent limits from individual dSphs.

## 1341 7.8 Conclusion and Discussion

1342 We want to include the remaining dSph and DM decay from the dSphs. We saw an improvement  
 1343 of TODO: value compared to Glory Duck which had many more dSphs. TODO: copy some text  
 1344 from earlier section.

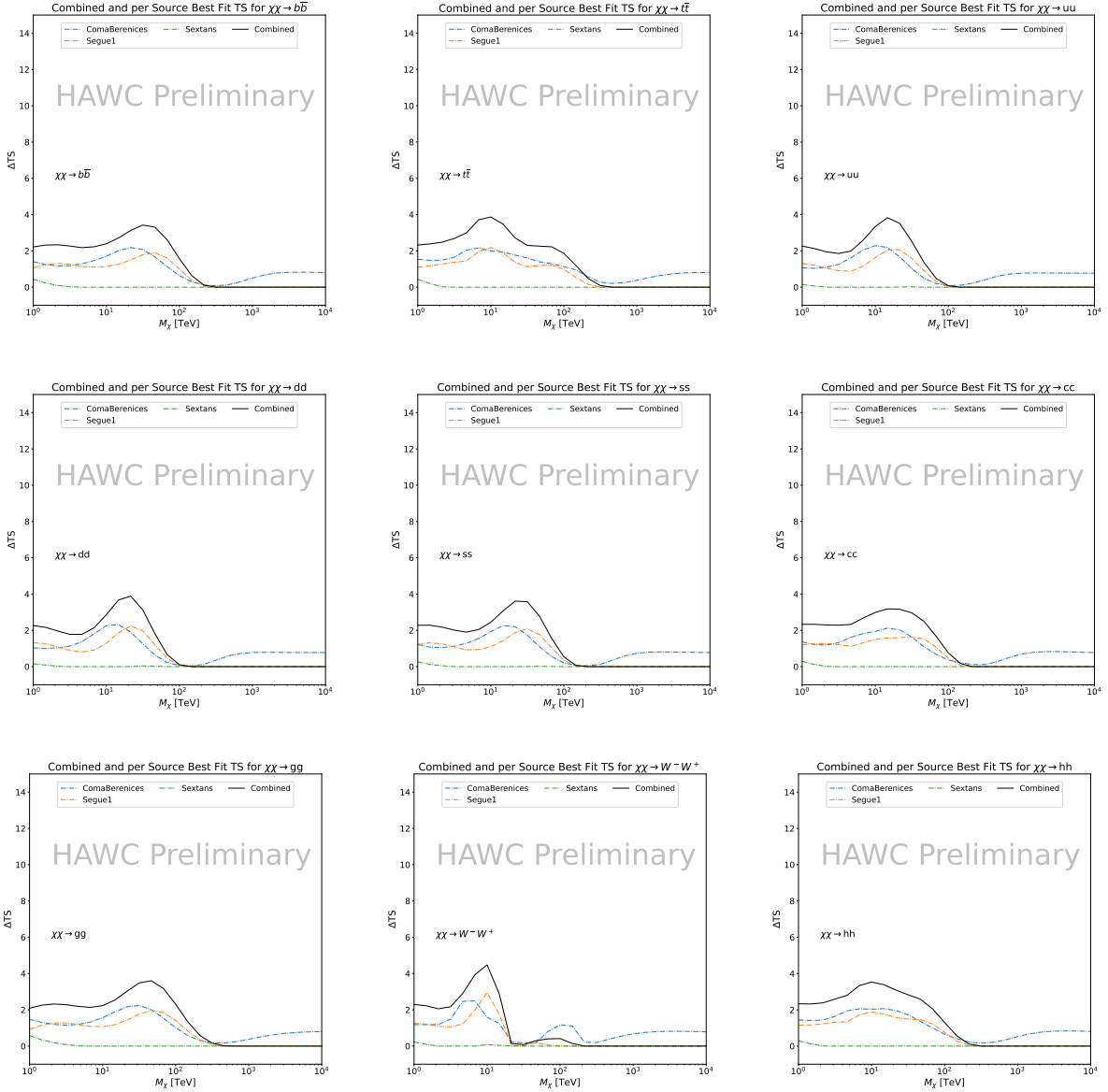


Figure 7.9 HAWC TS values for best fit  $\langle \sigma v \rangle$  versus  $m_\chi$  for SM annihilation channels:  $\chi\chi \rightarrow b\bar{b}$ ,  $t\bar{t}$ ,  $u\bar{u}$ ,  $d\bar{d}$ ,  $s\bar{s}$ ,  $c\bar{c}$ ,  $gg$ ,  $W^+W^-$ , and  $hh$ . Limits use  $\mathcal{L}\mathcal{S} J$  factors. The solid black line shows the combined best fit TS values. The colored, dashed lines are the TS values from each dSph.

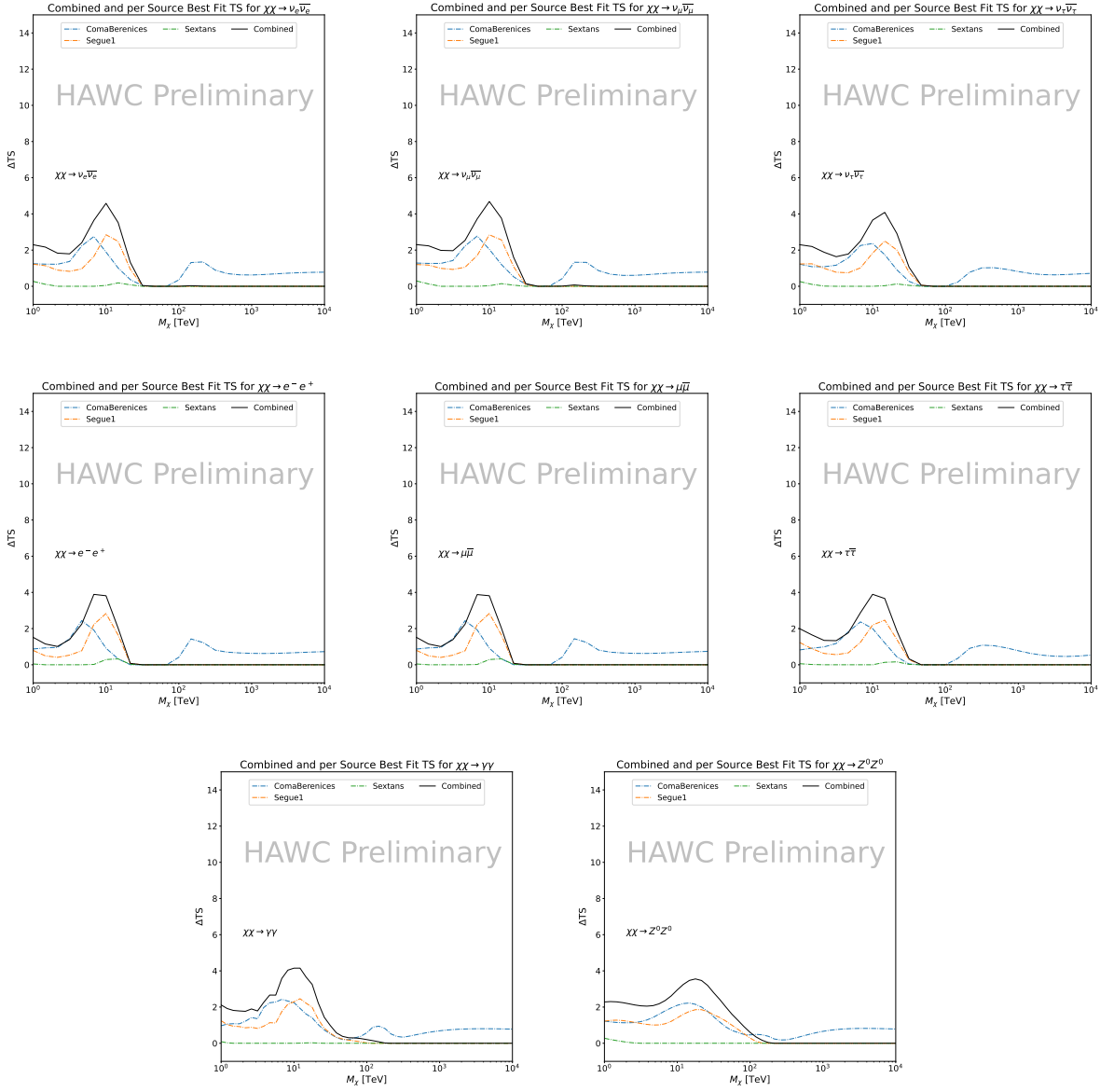


Figure 7.10 HAWC TS values for best fit  $\langle \sigma v \rangle$  versus  $m_\chi$  for SM annihilation channels:  $\chi\chi \rightarrow \nu_e \bar{\nu}_e$ ,  $\nu_\mu \bar{\nu}_\mu$ ,  $\nu_\tau \bar{\nu}_\tau$ ,  $e\bar{e}$ ,  $\mu\bar{\mu}$ ,  $\tau\bar{\tau}$ ,  $\gamma\gamma$  and  $ZZ$ . Limits use  $\mathcal{L}S J$  factors. The solid black line shows the combined best fit TS values. The colored, dashed lines are the TS values from each dSph.

Segue1

Coma Berenices

Sextans

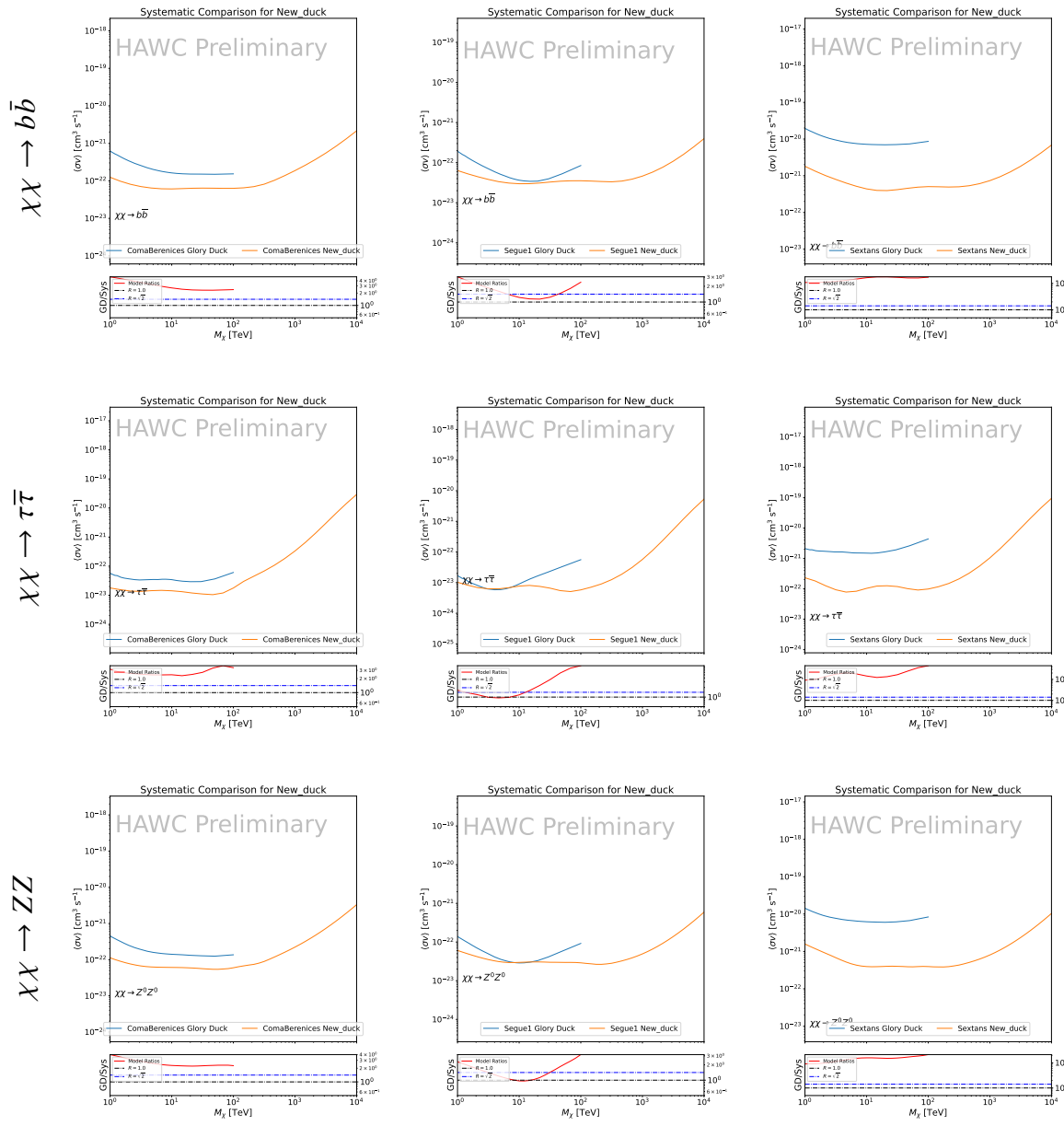


Figure 7.11 TODO: fill this out

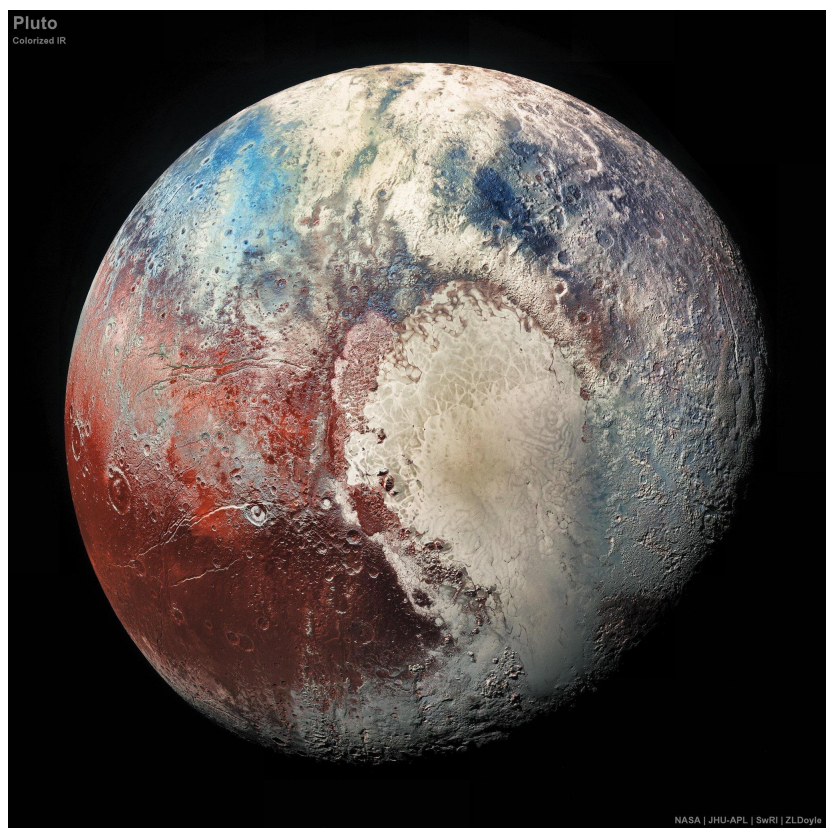


Figure 7.12 TODO: show p1 and m1 limits around[NEEDS A SOURCE][FACT CHECK THIS]



Figure 7.13 TODO: there will be 2[NEEDS A SOURCE][FACT CHECK THIS]

## **CHAPTER 8**

1345   **HEAVY DARK MATTER ANNIHILATION SEARCH WITH ICECUBE'S NORTH SKY**  
1346   **TRACK DATA**

1347

## **CHAPTER 9**

### **NU DUCK**

## MULTI-EXPERIMENT SUPPLEMENTARY FIGURES

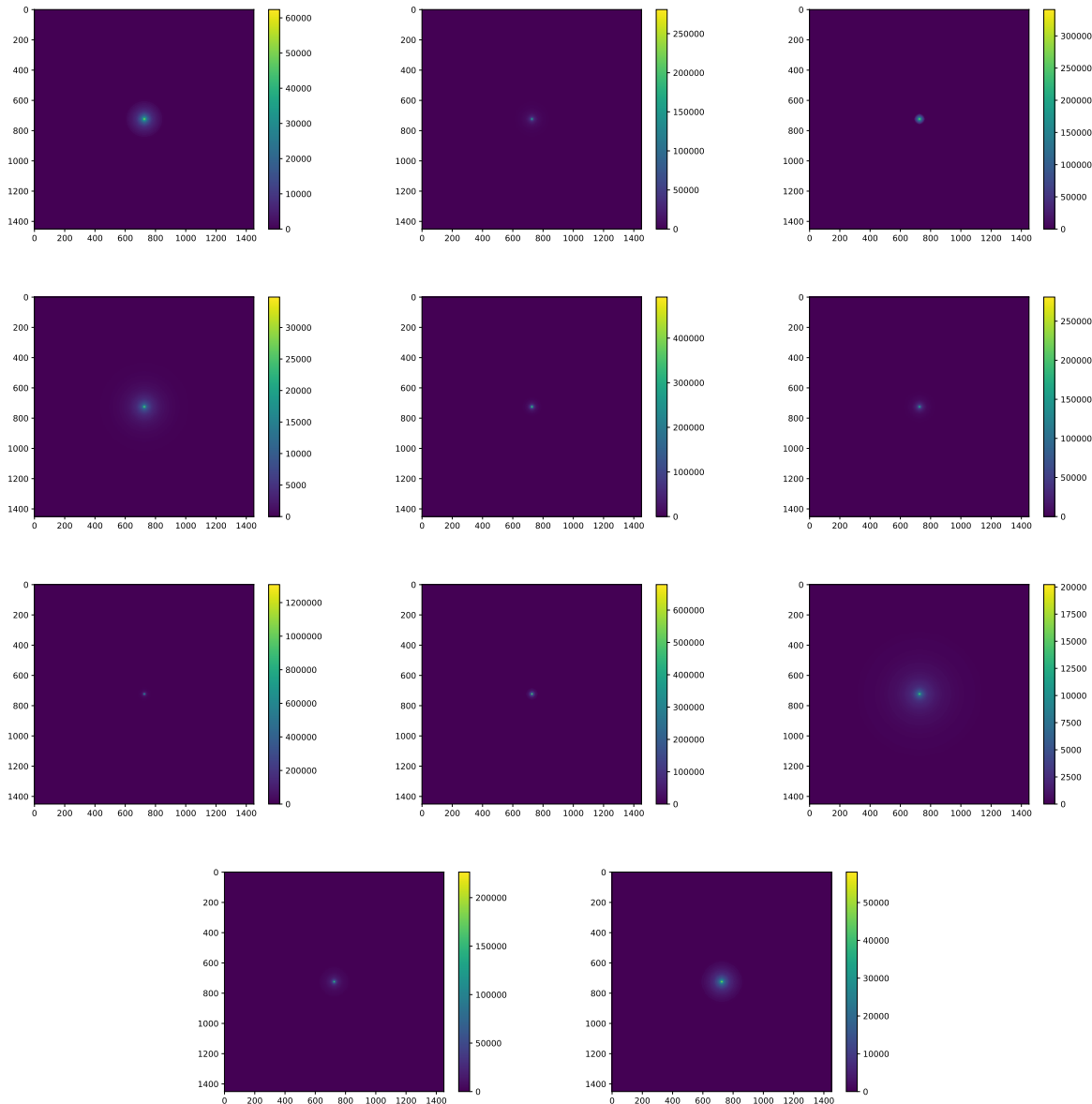


Figure A.1 Sister figure to Figure 6.3. Sources in the first row from left to right: Bootes I, Canes Venatici I, II. In second row: Draco, Hercules, Leo I. In the first row: Leo II, Leo IV, Sextans. In the final row: Ursa Major I, Ursa Major II.

## APPENDIX B

## MULTITHREADING DARK MATTER ANALYSES SUPPLEMENTARY MATERIAL

## 1350 B.1 Remaining Spectral Models

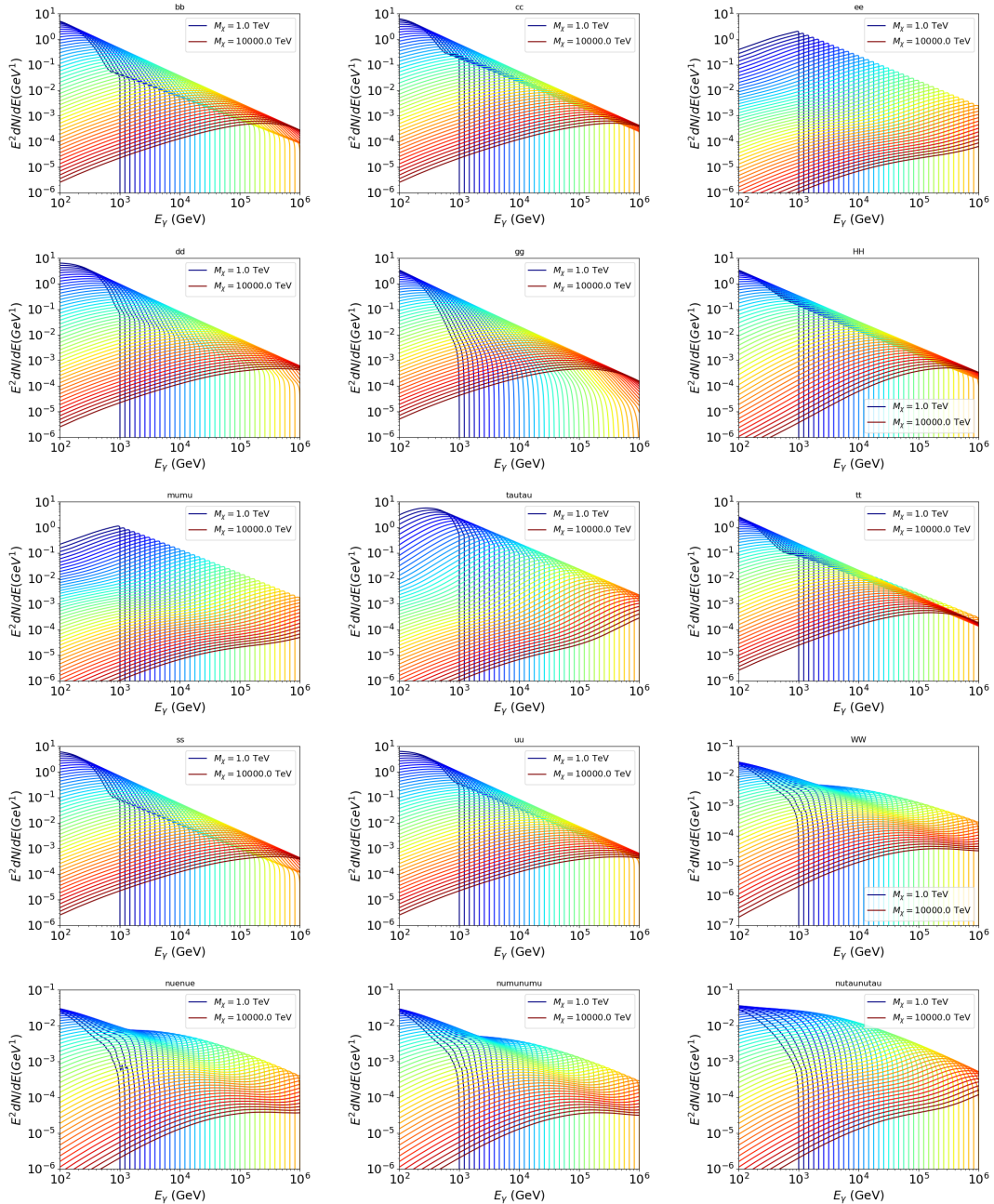


Figure B.1 Sister figure to Figure 7.2 for remaining SM primary annihilation channels studied for this thesis. These did not require any post generation smoothing and so are directly pulled from [64] with a binning scheme most helpful for a HAWC analysis.

## 1351 B.2 mpu\_analysis.py

```
13521 import warnings
13532 with warnings.catch_warnings():
13543     warnings.simplefilter("ignore")
13554 # Python base libraries
13565 import os
13576 import sys
13587 import time
13598 # Import general libraries with namespace
13609 import matplotlib
13610 # Necessary for computing on cluster
13621 matplotlib.use("agg")
13632 import numpy as np
13643 import multiprocessing as mp
13654 # Import HAWC software
13665 sys.path.insert(1, os.path.join(os.environ['HOME'], 'hawc_software', 'threeML-
1367     analysis-scripts', 'fitModel'))
13686 from analysis_modules import *
13697 from threeML import *
13708 from hawc_hal import HAL, HealpixConeROI
13719 from threeML.minimizer.minimization import FitFailed
13720 # Import Dark Matter HAWC Libraries
13731 import analysis_utils as au
13742 import spectra as spec
13753 import sources as srcs
13764
13775 #* READ ONLY PATHS This block will change eventually
13786 MASS_LIST = './plotting/studies/nd/masses.txt'
13797 CHAN_LIST = './plotting/studies/nd/chans.txt'
13808
13819 #* WRITE PATHS, default location is to scratch
13820 OUT_PATH = os.path.join(os.environ["SCRATCH"], os.environ["USER"], 'New_duck')
```

```

13831 print('Our out path is going to be {}'.format(OUT_PATH))
13842
13853 # Define parallel Function. Can also be run serially
13864 def some_mass_fit(sigVs, datalist, shape, dSph, jfactor, mass_chan,
13875                 progress=None, log_file='', queue=None, i_job=0):
13886
13897     if progress is None:
13908         progress = [0]
13919     else: # Create log files for each thread
13920         log_file = log_file.replace('.log', '_ThreadNo_')
13931         log_file = log_file + str(i_job) + ".log"
13942         sys.stdout = open(log_file, "w")
13953
13964     fits = []
13975
13986     try:
13997         for m_c in mass_chan:
14008             print(f'Mass chan tuple: {m_c}')
14019             mass = int(m_c[0])
14020             ch = m_c[1]
14031             # Build path to output files
14042             outPath = os.path.join(OUT_PATH, ch, dSph)
14053             au.ut.ensure_dir(outPath)
14064
14075             if progress[i_job] < 0:
14086                 # If the master gets a Keyboard interrupt, commit suicide.
14097                 break
14108
14119                 ### Start Model Building for DM mass and SM channel #####
14120                 spectrum = spec.DM_models.HDMSpectra()
14131                 spectrum.set_channel(ch)
14142
14153                 myDwarf = ExtendedSource(dSph, spatial_shape=shape,

```

```

14164                     spectral_shape=spectrum)
14175
14186             spectrum.J = jfactor * u.GeV**2 / u.cm**5
14197             spectrum.sigmav = 1e-24 * u.cm**3 / u.s
14208             spectrum.set_dm_mass(mass * u.GeV)
14219
14220             spectrum.sigmav.bounds = (1e-30, 1e-12)
14231             model = Model(myDwarf)
14242             ##### End model Building #####
14253
14264             jl = JointLikelihood(model, datalist, verbose=False)
14275
14286             try:
14297                 result, lhdf = jl.fit(compute_covariance=False)
14308                 ts = -2.* (jl.minus_log_like_profile(1e-30) - jl.
1431 _current_minimum)
14329                 # Also profile the LLH vs sv
14330                 ll = jl.get_contours(spectrum.sigmav, sigVs[0],
14341                               sigVs[-1], len(sigVs),
14352                               progress=False, log=['False'])
14363
14374                 sigv_ll = au.ut.calc_95_from_profile(ll[0], ll[2])
14385                 # Write results to file
14396                 outFileLL = outPath+f"/LL_{dSph}_{ch}_mass{int(mass)}_GD.txt"
14407                 np.savetxt(outFileLL, (sigVs, ll[2]),
14418                               delimiter='\t', header='sigV\tLL\n')
14429
14430                 with open(outPath+f"/results_{dSph}_{ch}_mass{int(mass)}_GD.
1444 txt", "w") as results_file:
14451                     results_file.write("mDM [GeV]\tsigV_95\tsigV_B.F.\n")
14462
14473                     results_file.write("%i\t%.5E\t%.5E\t%.5E"%(mass, sigv_ll,
14484                                         ts, result.value[0]))

```

```

14495         # End write to file
14506     except FitFailed: # Don't kill all threads if a fit fails
14517         print("Fit failed. Go back and calculate this spectral model
1452 later")
14538         fits.append((ch, mass, -1, -1))
14549         with open(log_file+'.fail', 'w') as f_file:
14550             f_file.write(f'{ch}, {mass}\n')
14561
14572         progress[i_job] += 1
14583         matplotlib.pyplot.close() # Prevent leaky memory
14594
14605         fits.append((ch, mass, result.value[0], ts))
14616         progress[i_job] += 1
14627         matplotlib.pyplot.close()
14638     except KeyboardInterrupt:
14649         progress[i_job] = -1
14650
14661     fits = np.array(fits)
14672     if queue is None:
14683         return fits
14694     else:
14705         queue.put((i_job, fits))
14716
14727 def main(args):
14738     masses = np.loadtxt(MASS_LIST, dtype=int)
14749     chans = np.loadtxt(CHAN_LIST, delimiter=',', dtype=str)
14750     mass_chan = au.ut.permute_lists(chans, masses)
14761
14772     print(f"DM masses for this study are: {masses}")
14783     print(f"SM Channels for this study are XX -> {chans}")
14794     print(mass_chan)
14805
14816 # extract information from input argument

```

```

14827 dSph = args.dSph
14838 data_mngr = au.ut.Data_Selector('P5_NN_2D')
14849 dm_profile = srcts.Spatial_DM(args.catalog, dSph, args.sigma, args.decay)
14850
14861     ### Extract Source Information ####
14872 if dm_profile.get_dec() < -22.0 or dm_profile.get_dec() > 62.0:
14883     raise ValueError("HAWC can't see this source D: Exitting now...")
14894
14905 print(f'{dSph} information')
14916 print(f'jfac: {dm_profile.get_factor()}\tRA: {dm_profile.get_ra()}\tDec: {dm_profile.get_dec()}\n')
1492
14937
14948 shape = SpatialTemplate_2D(fits_file=dm_profile.get_src_fits())
14959     ### Finish Extract Source Information ####
14960
14971     ### LOAD HAWC DATA ####
14982 roi = HealpixConeROI(data_radius=2.0, model_radius=8.0,
14993                         ra=dm_profile.get_ra(), dec=dm_profile.get_dec())
15004 bins = choose_bins.analysis_bins(args, dec=dm_profile.get_dec())
15015
15026 hawc = HAL(dSph, data_mngr.get_datmap(), data_mngr.get_detres(), roi)
15037 hawc.set_active_measurements(bin_list=bins)
15048 datalist = DataList(hawc)
15059     ### FINISH LOAD HAWC DATA ####
15060
15071 # set up SigV sampling. This sample is somewhat standardized
15082 sigVs = np.logspace(-28,-18, 1001, endpoint=True) # NOTE This will change
1509 whith HDM
15103
15114 if args.n_threads == 1:
15125     # No need to start || programming just iterate over the masses
15136     kw_arg = dict(sigVs=sigVs, datalist=datalist, shape=shape, dSph=dSph,
15147                     jfactor=dm_profile.get_factor(), mass_chan=mass_chan,

```

```

15158                 log_file=args.log)
15159             some_mass_fit(**kw_arg)
15160         else:
15161             # I Really want to suppress TQMD output
15162             from tqdm import tqdm
15163             from functools import partialmethod
15164             tqdm.__init__ = partialmethod(tqdm.__init__, disable=True)
15165
15166             x = np.array_split(mass_chan, args.n_threads)
15167             n_jobs = len(x)
15168
15169             print("Thread jobs summary by mass and SM channel")
15170             for xi in x:
15171                 print(f'{xi}')
15172
15173             queue = mp.Queue()
15174             progress = mp.Array('i', np.zeros(n_jobs, dtype=int))
15175
15176             # Define task pool that will be split amongsts threads
15177             kw_args = [dict(sigVs=sigVs, datalist=datalist, shape=shape,
15178                            dSph=dSph, jfactor=dm_profile.get_factor(),
15179                            mass_chan=mass_chan, progress=progress,
15180                            queue=queue, i_job=i, log_file=args.log)
15181                     for i, mass_chan in enumerate(x)]
15182
15183             # Define each process
15184             procs = [mp.Process(target=some_mass_fit, kwargs=kw_args[i]) \
15185                     for i in range(n_jobs)]
15186
15187             ### Start MASTER Thread only code block ###
15188             # Begin running all child threads
15189             for proc in procs: proc.start()
15190

```

```

15481     try:
15492         # In this case, the master does nothing except monitor progress of
1550         the threads
15513         # In an ideal world, the master thread also does some computation.
15524             n_complete = np.sum(progress)
15535             while_count = 0
15546
15557             while n_complete < len(mass_chan):
15568
15579                 if np.any(np.asarray(progress) < 0):
15580                     # This was no threads are stranded when killing the script
15591                     raise KeyboardInterrupt()
15602                     if while_count%1000 == 0:
15613                         print(f"{np.sum(progress)} of {len(mass_chan)} finished")
15624
15635                     n_complete = np.sum(progress)
15646                     time.sleep(.25)
15657                     while_count += 1
15668
15679             except KeyboardInterrupt:
15680                 # signal to jobs that it's time to stop
15691                     for i in range(n_jobs):
15702                         progress[i] = -2
15713                         print('\nKeyboardInterrupt: terminating early.')
15724                     ### End MASTER Thread only code block ###
15735
15746                     fitss = [queue.get() for proc in procs]
15757                     print(fitss)
15768                     print(f'Thread statuses: {progress[:]}')
15779
15780                     # putting results in a file
15791
15802                     print("QUACK! All Done!")

```

```

15813
15824
15835 if __name__ == '__main__':
15846     import argparse
15857
15868     p = argparse.ArgumentParser(description="Run a DM annihilation analysis on
1587         a dwarf spheroidal for a specific SM channel for DM masses [1 TeV to 10
1588         PeV]")
15899
15900     # Dwarf spatial modeling arguements
15911     p.add_argument("-ds", "--dSph", type=str,
15922                     help="dwarf spheroidal galaxy to be studied", required=
1593 True)
15943     p.add_argument("-cat", "--catalog", type=str, choices=['GS15', 'LS20'],
15954                     default='LS20', help="source catalog used")
15965     p.add_argument("-sig", "--sigma", type=int, choices=[-1, 0, 1], default=0,
15976                     help="Spatial model uncertainty. 0 corresponds to the
1598 median. +/-1 correspond to the +/-1sigma uncertainty respectively.")
15997
16008     # Arguements for the energy estimators
16019     p.add_argument("-e", "--estimator", type=str,
16020                     choices=['P5_NHIT', 'P5_NN_2D'],
16031                     default="P5_NN_2D", required=False,
16042                     help="The energy estimator choice. Options are: P5_NHIT,
1605 P5_NN_2D. GP not supported (yet).")
16063     p.add_argument("--use-bins", default=None, nargs="*",
16074                     help="Bins to use for the analysis", dest="use_bins")
16085     p.add_argument('--select_bins_by_energy', default=None, nargs="*",
16096                     help="Does nothing. May fill in later once better
1610 understood")
16117     p.add_argument('--select_bins_by_fhit', default=None, nargs="*",
16128                     help="Also does nothing see above")
16139     p.add_argument( '-ex', "--exclude", default=None, nargs="*",

```

```

16140         help="Exclude Bins", dest="exclude")

16151

16162 # Computing and logging arguements.

16173 p.add_argument('-nt', '--n_threads', type=int, default=1,
16184                         help='Maximum number of threads spawned by script. Default
1619 is 4')

16205 p.add_argument('-log', '--log', type=str, required=True,
16216                         help='Name for log files. Especially needed for threads')

16227

16238 p.add_argument('--decay', action="store_true",
16249                         help='Set spectral DM hypothesis to decay')

16250

16261 args = p.parse_args()

16272 print(args.decay)

16283 if args.exclude is None: # default exclude bins 0 and 1
16294     args.exclude = ['B0C0Ea', 'B0C0Eb', 'B0C0Ec', 'B0C0Ed', 'B0C0Ee']

16305

16316 if args.decay: OUT_PATH += '_dec'
16327 else: OUT_PATH += '_ann'

16338

16349 OUT_PATH = OUT_PATH + '_' + args.catalog
16350 if args.sigma != 0: OUT_PATH += f'_{args.sigma}sig'

16361

16372 main(args)

```

1638 B.3 Comparison with Glory Duck

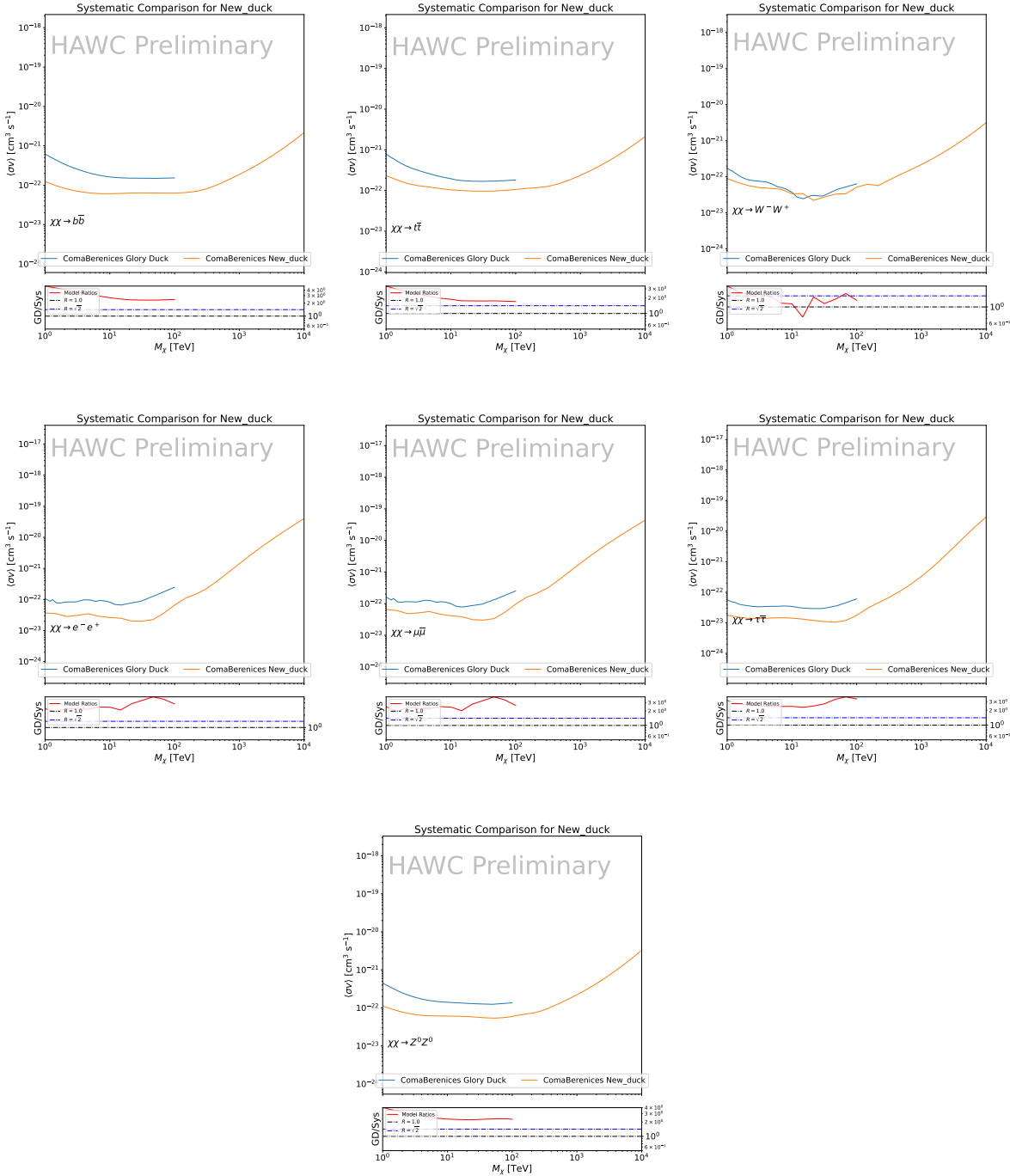


Figure B.2 TODO: fill this out

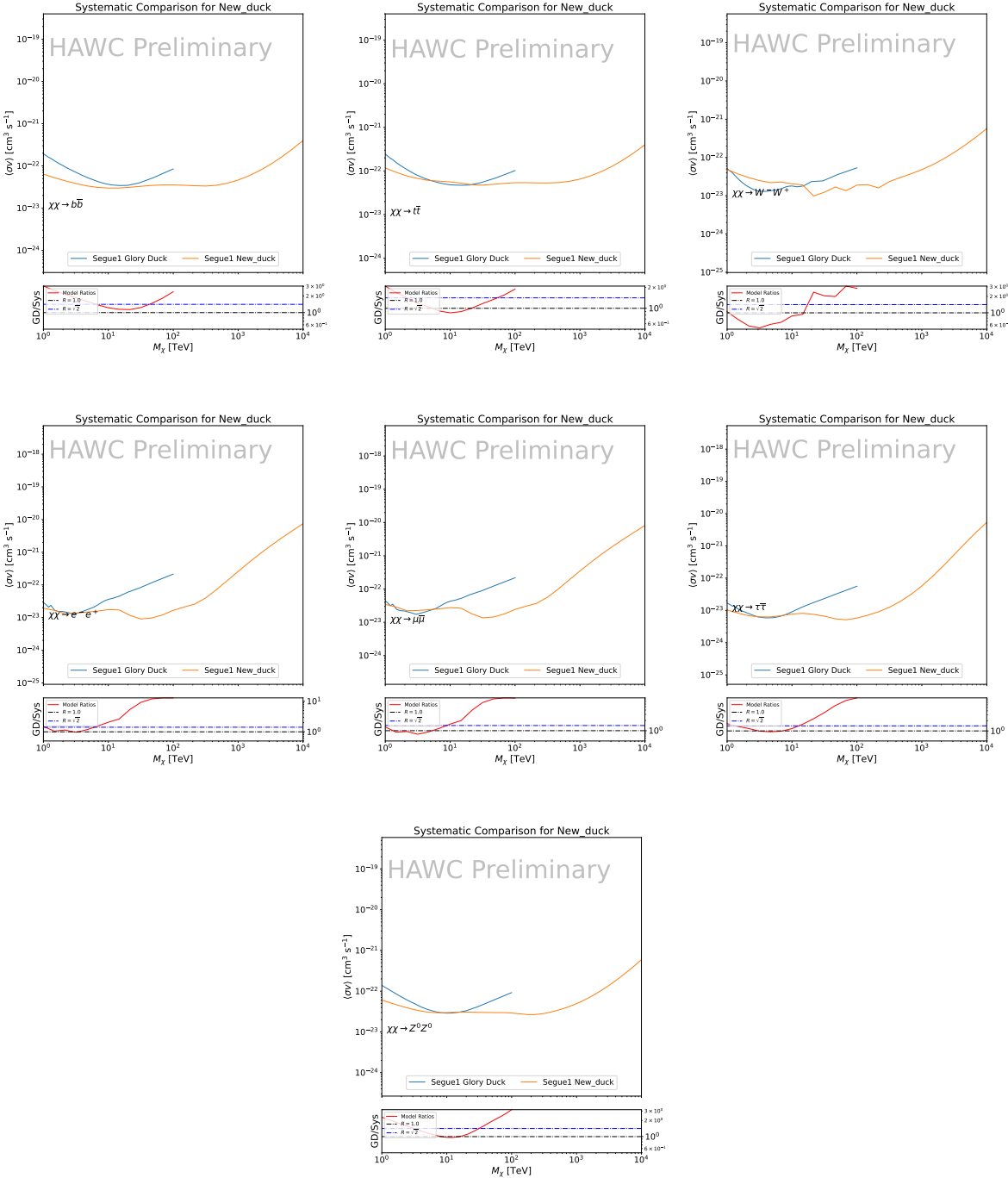


Figure B.3 TODO: fill this out

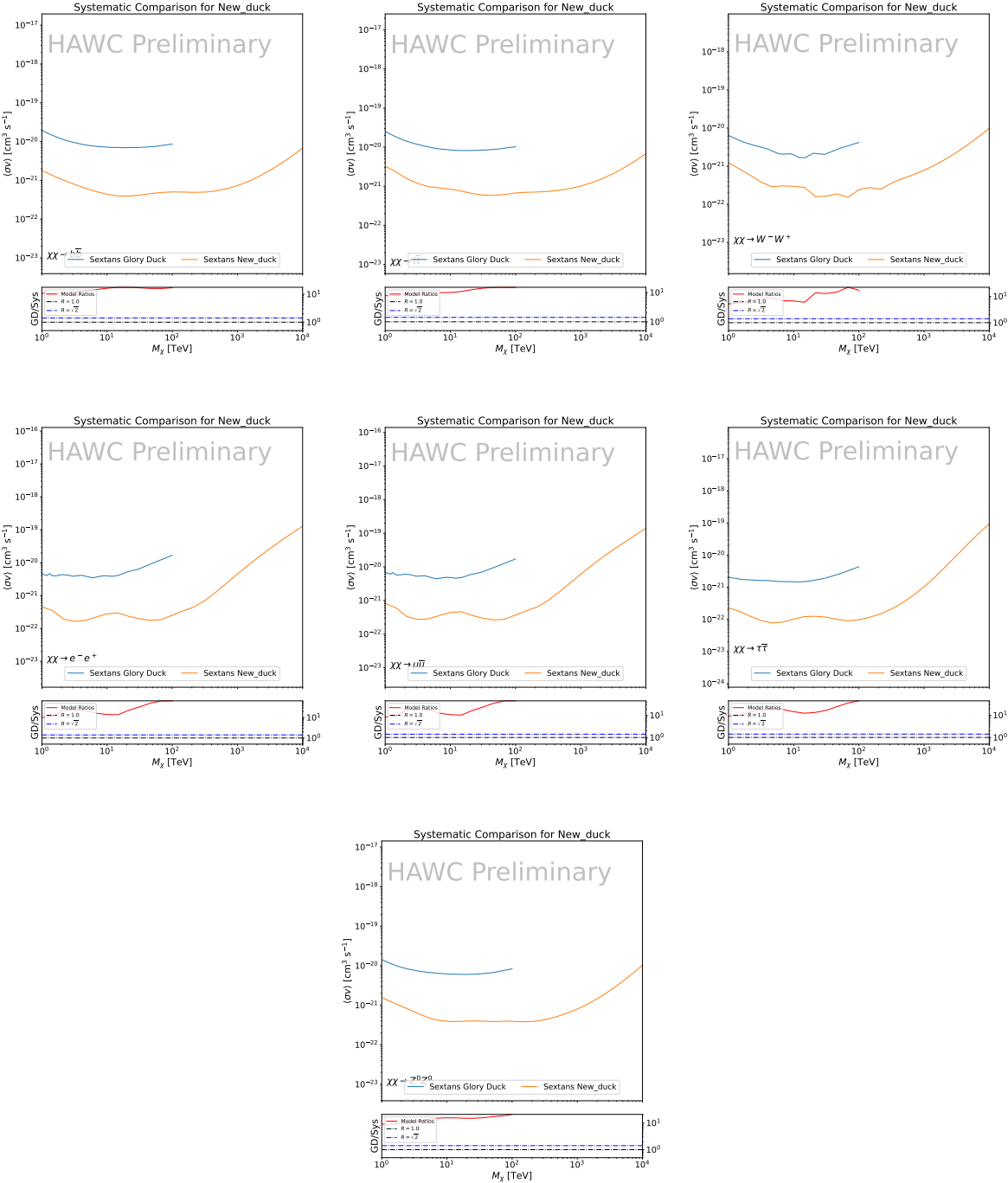


Figure B.4 TODO: fill this out

## BIBLIOGRAPHY

- [1] Anne M. Green. “Dark matter in astrophysics/cosmology”. In: *SciPost Phys. Lect. Notes* (2022), p. 37. doi: [10.21468/SciPostPhysLectNotes.37](https://doi.org/10.21468/SciPostPhysLectNotes.37). URL: <https://scipost.org/10.21468/SciPostPhysLectNotes.37>.
- [2] Bing-Lin Young. “A survey of dark matter and related topics in cosmology”. In: *Frontiers of Physics* 12 (Oct. 2016). doi: <https://doi.org/10.1007/s11467-016-0583-4>. URL: <https://doi.org/10.1007/s11467-016-0583-4>.
- [3] Gianfranco Bertone, Dan Hooper, and Joseph Silk. “Particle dark matter: evidence, candidates and constraints”. In: *Physics Reports* 405.5 (2005), pp. 279–390. issn: 0370-1573. doi: <https://doi.org/10.1016/j.physrep.2004.08.031>. URL: <https://www.sciencedirect.com/science/article/pii/S0370157304003515>.
- [4] Gianfranco Bertone and Dan Hooper. “History of dark matter”. In: *Rev. Mod. Phys.* 90 (4 Aug. 2018), p. 045002. doi: [10.1103/RevModPhys.90.045002](https://doi.org/10.1103/RevModPhys.90.045002). URL: <https://link.aps.org/doi/10.1103/RevModPhys.90.045002>.
- [5] Fritz Zwicky. “The Redshift of Extragalactic Nebulae”. In: *Helvetica Physica Acta* 6. (1933), pp. 110–127. doi: [10.5169/seals-110267](https://doi.org/10.5169/seals-110267).
- [6] Vera C. Rubin and Jr. Ford W. Kent. “Rotation of the Andromeda Nebula from a Spectroscopic Survey of Emission Regions”. In: *ApJ* 159 (Feb. 1970), p. 379. doi: [10.1086/150317](https://doi.org/10.1086/150317).
- [7] K. G. Begeman, A. H. Broeils, and R. H. Sanders. “Extended rotation curves of spiral galaxies: dark haloes and modified dynamics”. In: *Monthly Notices of the Royal Astronomical Society* 249.3 (Apr. 1991), pp. 523–537. issn: 0035-8711. doi: [10.1093/mnras/249.3.523](https://doi.org/10.1093/mnras/249.3.523). eprint: <https://academic.oup.com/mnras/article-pdf/249/3/523/18160929/mnras249-0523.pdf>. URL: <https://doi.org/10.1093/mnras/249.3.523>.
- [8] *Different types of gravitational lenses*. website. Feb. 2004. URL: <https://esahubble.org/images/heic0404b/>.
- [9] Douglas Clowe et al. “A Direct Empirical Proof of the Existence of Dark Matter”. In: *apjl* 648.2 (Sept. 2006), pp. L109–L113. doi: [10.1086/508162](https://doi.org/10.1086/508162). arXiv: [astro-ph/0608407 \[astro-ph\]](https://arxiv.org/abs/astro-ph/0608407).
- [10] Planck Collaboration and N. et. al. Aghanim. “Planck 2018 results I. Overview and the cosmological legacy of Planck”. In: *A&A* 641 (2020). doi: [10.1051/0004-6361/201833880](https://doi.org/10.1051/0004-6361/201833880). URL: <https://doi.org/10.1051/0004-6361/201833880>.
- [11] Wayne Hu. *Matter Density Animation*. web. 2024. URL: <http://background.uchicago.edu/~whu/animbut/anim2.html>.

- 1673 [12] Wenlong Yuan et al. “A First Look at Cepheids in a Type Ia Supernova Host with JWST”. in:  
1674     *The Astrophysical Journal Letters* 940.1 (Nov. 2022). doi: [10.3847/2041-8213/ac9b27](https://doi.org/10.3847/2041-8213/ac9b27).  
1675     URL: <https://dx.doi.org/10.3847/2041-8213/ac9b27>.
- 1676 [13] Wendy L. Freedman. “Measurements of the Hubble Constant: Tensions in Perspective”. In:  
1677     *The Astrophysical Journal* 919.1 (Sept. 2021), p. 16. doi: [10.3847/1538-4357/ac0e95](https://doi.org/10.3847/1538-4357/ac0e95).  
1678     URL: <https://dx.doi.org/10.3847/1538-4357/ac0e95>.
- 1679 [14] Jodi Cooley. “Dark Matter direct detection of classical WIMPs”. In: *SciPost Phys. Lect.*  
1680     *Notes* (2022), p. 55. doi: [10.21468/SciPostPhysLectNotes.55](https://doi.org/10.21468/SciPostPhysLectNotes.55). URL: <https://scipost.org/10.21468/SciPostPhysLectNotes.55>.
- 1682 [15] “Search for new phenomena in events with an energetic jet and missing transverse momentum  
1683     in  $pp$  collisions at  $\sqrt{s} = 13$  TeV with the ATLAS detector”. In: *Phys. Rev. D* 103  
1684     (11 July 2021), p. 112006. doi: [10.1103/PhysRevD.103.112006](https://doi.org/10.1103/PhysRevD.103.112006). URL: <https://link.aps.org/doi/10.1103/PhysRevD.103.112006>.
- 1686 [16] *Jetting into the dark side: a precision search for dark matter*. website. July 2020. URL:  
1687     <https://atlas.cern/updates/briefing/precision-search-dark-matter>.
- 1688 [17] Celine Armand et. al. “Combined dark matter searches towards dwarf spheroidal galaxies  
1689     with Fermi-LAT, HAWC, H.E.S.S., MAGIC, and VERITAS”. in: *Proceedings of Science*.  
1690     Vol. 395. Mar. 2022. doi: <https://doi.org/10.22323/1.395.0528>.
- 1691 [18] Tracy R. Slatyer. “Les Houches Lectures on Indirect Detection of Dark Matter”. In: *SciPost*  
1692     *Phys. Lect. Notes* (2022), p. 53. doi: [10.21468/SciPostPhysLectNotes.53](https://doi.org/10.21468/SciPostPhysLectNotes.53). URL:  
1693     <https://scipost.org/10.21468/SciPostPhysLectNotes.53>.
- 1694 [19] Christian W Bauer, Nicholas L. Rodd, and Bryan R. Webber. “Dark matter spectra from  
1695     the electroweak to the Planck scale”. In: *Journal of High Energy Physics* 2021.1029-8479  
1696     (June 2021). doi: [https://doi.org/10.1007/JHEP06\(2021\)121](https://doi.org/10.1007/JHEP06(2021)121).
- 1697 [20] Riccardo Catena and Piero Ullio. “A novel determination of the local dark matter density”.  
1698     In: *Journal of Cosmology and Astroparticle Physics* 2010.08 (Aug. 2010), p. 004. doi:  
1699     [10.1088/1475-7516/2010/08/004](https://doi.org/10.1088/1475-7516/2010/08/004). URL: <https://dx.doi.org/10.1088/1475-7516/2010/08/004>.
- 1701 [21] B. P. Abbott et al. “Observation of Gravitational Waves from a Binary Black Hole Merger”.  
1702     In: *Phys. Rev. Lett.* 116 (6 Feb. 2016), p. 061102. doi: [10.1103/PhysRevLett.116.061102](https://doi.org/10.1103/PhysRevLett.116.061102). URL: <https://link.aps.org/doi/10.1103/PhysRevLett.116.061102>.
- 1704 [22] R. Abbasi et. al. “Observation of high-energy neutrinos from the Galactic plane”. In: *Science*  
1705     380.6652 (June 2023), pp. 1338–1343.

- 1706 [23] NASA Goddard Space Flight Center. *Fermi's 12-year view of the gamma-ray sky*. website.  
1707 2022. URL: <https://svs.gsfc.nasa.gov/14090>.
- 1708 [24] Marco Cirelli et al. "PPPC 4 DM ID: a poor particle physicist cookbook for dark matter  
1709 indirect detection". In: *Journal of Cosmology and Astroparticle Physics* 2011.03 (Mar.  
1710 2011), p. 051. doi: [10.1088/1475-7516/2011/03/051](https://doi.org/10.1088/1475-7516/2011/03/051). URL: <https://dx.doi.org/10.1088/1475-7516/2011/03/051>.
- 1712 [25] Javier Rico. "Gamma-Ray Dark Matter Searches in Milky Way Satellites—A Comparative  
1713 Review of Data Analysis Methods and Current Results". In: *Galaxies* 8.1 (Mar. 2020), p. 25.  
1714 doi: [10.3390/galaxies8010025](https://doi.org/10.3390/galaxies8010025). arXiv: [2003.13482 \[astro-ph.HE\]](https://arxiv.org/abs/2003.13482).
- 1715 [26] W. B. Atwood et al. "The Large Area Telescope on the Fermi Gamma-Ray Space Telescope  
1716 Mission". In: *apj* 697.2 (June 2009), pp. 1071–1102. doi: [10.1088/0004-637X/697/2/1071](https://doi.org/10.1088/0004-637X/697/2/1071). arXiv: [0902.1089 \[astro-ph.IM\]](https://arxiv.org/abs/0902.1089).
- 1718 [27] M. Ackermann et al. "Searching for Dark Matter Annihilation from Milky Way Dwarf  
1719 Spheroidal Galaxies with Six Years of Fermi Large Area Telescope Data". In: *prl* 115.23,  
1720 231301 (Dec. 2015), p. 231301. doi: [10.1103/PhysRevLett.115.231301](https://doi.org/10.1103/PhysRevLett.115.231301). arXiv:  
1721 [1503.02641 \[astro-ph.HE\]](https://arxiv.org/abs/1503.02641).
- 1722 [28] Mattia Di Mauro, Martin Stref, and Francesca Calore. "Investigating the effect of Milky  
1723 Way dwarf spheroidal galaxies extension on dark matter searches with Fermi-LAT data".  
1724 In: *Phys. Rev. D* 106 (12 Dec. 2022), p. 123032. doi: [10.1103/PhysRevD.106.123032](https://doi.org/10.1103/PhysRevD.106.123032).  
1725 URL: <https://link.aps.org/doi/10.1103/PhysRevD.106.123032>.
- 1726 [29] F. et al. Aharonian. "Observations of the Crab Nebula with H.E.S.S.". In: *Astron. Astrophys.*  
1727 457 (2006), pp. 899–915. doi: [10.1051/0004-6361:20065351](https://doi.org/10.1051/0004-6361:20065351). arXiv: [astro-ph/0607333](https://arxiv.org/abs/astro-ph/0607333).
- 1729 [30] J. Albert et al. "VHE  $\gamma$ -Ray Observation of the Crab Nebula and its Pulsar with the MAGIC  
1730 Telescope". In: *The Astrophysical Journal* 674.2 (Feb. 2008), p. 1037. doi: [10.1086/525270](https://doi.org/10.1086/525270). URL: <https://dx.doi.org/10.1086/525270>.
- 1732 [31] N. Park. "Performance of the VERITAS experiment". In: *Proceedings, 34th International  
1733 Cosmic Ray Conference (ICRC2015): The Hague, The Netherlands, July, 30th July - 6th  
1734 August*. Vol. 34. 2015, p. 771. arXiv: [1508.07070 \[astro-ph.IM\]](https://arxiv.org/abs/1508.07070).
- 1735 [32] A. Abramowski et al. "H.E.S.S. constraints on Dark Matter annihilations towards the Sculptor  
1736 and Carina Dwarf Galaxies". In: *Astropart. Phys.* 34 (2011), pp. 608–616. doi: [10.1016/j.astropartphys.2010.12.006](https://doi.org/10.1016/j.astropartphys.2010.12.006). arXiv: [1012.5602 \[astro-ph.HE\]](https://arxiv.org/abs/1012.5602).
- 1738 [33] A. Abramowski et al. "Search for dark matter annihilation signatures in H.E.S.S. observations  
1739 of Dwarf Spheroidal Galaxies". In: *Phys. Rev. D* 90 (2014), p. 112012. doi: [10.1103/PhysRevD.90.112012](https://doi.org/10.1103/PhysRevD.90.112012). arXiv: [1410.2589 \[astro-ph.HE\]](https://arxiv.org/abs/1410.2589).

- 1741 [34] H. Abdalla et al. “Searches for gamma-ray lines and ‘pure WIMP’ spectra from Dark  
1742 Matter annihilations in dwarf galaxies with H.E.S.S”. in: *JCAP* 11 (2018), p. 037. doi:  
1743 [10.1088/1475-7516/2018/11/037](https://doi.org/10.1088/1475-7516/2018/11/037). arXiv: [1810.00995 \[astro-ph.HE\]](https://arxiv.org/abs/1810.00995).
- 1744 [35] J. Aleksić et al. “Optimized dark matter searches in deep observations of Segue 1 with  
1745 MAGIC”. in: *JCAP* 1402 (2014), p. 008. doi: [10.1088/1475-7516/2014/02/008](https://doi.org/10.1088/1475-7516/2014/02/008).  
1746 arXiv: [1312.1535 \[hep-ph\]](https://arxiv.org/abs/1312.1535).
- 1747 [36] V.A. Acciari et al. “Combined searches for dark matter in dwarf spheroidal galaxies observed  
1748 with the MAGIC telescopes, including new data from Coma Berenices and Draco”. In: *Physics of the Dark Universe* (2021), p. 100912. issn: 2212-6864. doi: <https://doi.org/10.1016/j.dark.2021.100912>. URL: <https://www.sciencedirect.com/science/article/pii/S2212686421001370>.
- 1752 [37] M. L. Ahnen et al. “Indirect dark matter searches in the dwarf satellite galaxy Ursa Major II  
1753 with the MAGIC Telescopes”. In: *JCAP* 1803.03 (2018), p. 009. doi: [10.1088/1475-7516/2018/03/009](https://doi.org/10.1088/1475-7516/2018/03/009). arXiv: [1712.03095 \[astro-ph.HE\]](https://arxiv.org/abs/1712.03095).
- 1755 [38] S. et al. Archambault. “Dark matter constraints from a joint analysis of dwarf Spheroidal  
1756 galaxy observations with VERITAS”. in: *prd* 95.8 (Apr. 2017). doi: [10.1103/PhysRevD.95.082001](https://doi.org/10.1103/PhysRevD.95.082001). arXiv: [1703.04937 \[astro-ph.HE\]](https://arxiv.org/abs/1703.04937).
- 1758 [39] Louise Oakes et al. “Combined Dark Matter searches towards dwarf spheroidal galaxies with  
1759 Fermi-LAT, HAWC, HESS, MAGIC and VERITAS”. in: *Proceedings of Science*. 2019.
- 1760 [40] Celine Armand et al. on behalf of the Fermi-LAT, HAWC, HESS, MAGIC, VERITAS.  
1761 “Combined Dark Matter searches towards dwarf spheroidal galaxies with Fermi-LAT,  
1762 HAWC, HESS, MAGIC and VERITAS”. in: *Proceedings of Science*. 2021.
- 1763 [41] Daniel Kerszberg et al. on behalf of the Fermi-LAT, HAWC, HESS, MAGIC, and VER-  
1764 TIAS collaborations. “Search for dark matter annihilation with a combined analysis of  
1765 dwarf spheroidal galaxies from Fermi-LAT, HAWC, H.E.S.S., MAGIC and VERITAS”. in:  
1766 *Proceedings of Science*. 2023.
- 1767 [42] A. U. Abeysekara et al. “Observation of the Crab Nebula with the HAWC Gamma-Ray  
1768 Observatory”. In: *The Astrophysical Journal* 843.1 (June 2017), p. 39. doi: [10.3847/1538-4357/aa7555](https://doi.org/10.3847/1538-4357/aa7555). URL: <https://doi.org/10.3847/1538-4357/aa7555>.
- 1770 [43] Giacomo Vianello et al. *The Multi-Mission Maximum Likelihood framework (3ML)*. 2015.  
1771 arXiv: [1507.08343 \[astro-ph.HE\]](https://arxiv.org/abs/1507.08343).
- 1772 [44] Marco Cirelli et al. “PPPC 4 DM ID: a poor particle physicist cookbook for dark matter  
1773 indirect detection”. In: *Journal of Cosmology and Astroparticle Physics* 2011.03 (Mar.  
1774 2011). issn: 1475-7516. doi: [10.1088/1475-7516/2011/03/051](https://doi.org/10.1088/1475-7516/2011/03/051). URL: <http://dx.doi.org/10.1088/1475-7516/2011/03/051>.

- 1776 [45] Alex Geringer-Sameth, Savvas M. Koushiappas, and Matthew Walker. “DWARF GALAXY  
1777 ANNIHILATION AND DECAY EMISSION PROFILES FOR DARK MATTER EXPERI-  
1778 MENTS”. in: *The Astrophysical Journal* 801.2 (Mar. 2015), p. 74. ISSN: 1538-4357. doi:  
1779 [10.1088/0004-637X/801/2/74](https://doi.org/10.1088/0004-637X/801/2/74). URL: <http://dx.doi.org/10.1088/0004-637X/801/2/74>.
- 1781 [46] A. Albert et al. “Dark Matter Limits from Dwarf Spheroidal Galaxies with the HAWC  
1782 Gamma-Ray Observatory”. In: *The Astrophysical Journal* 853.2 (Feb. 2018), p. 154. ISSN:  
1783 1538-4357. doi: [10.3847/1538-4357/aaa6d8](https://doi.org/10.3847/1538-4357/aaa6d8). URL: <http://dx.doi.org/10.3847/1538-4357/aaa6d8>.
- 1785 [47] V. Bonnivard et al. “Spherical Jeans analysis for dark matter indirect detection in dwarf  
1786 spheroidal galaxies - Impact of physical parameters and triaxiality”. In: *Mon. Not. Roy.  
1787 Astron. Soc.* 446 (2015), pp. 3002–3021. doi: [10.1093/mnras/stu2296](https://doi.org/10.1093/mnras/stu2296). arXiv:  
1788 [1407.7822 \[astro-ph.HE\]](https://arxiv.org/abs/1407.7822).
- 1789 [48] M. Ackermann et al. “Searching for Dark Matter Annihilation from Milky Way Dwarf  
1790 Spheroidal Galaxies with Six Years of Fermi Large Area Telescope Data”. In: *prl* 115.23,  
1791 231301 (Dec. 2015), p. 231301. doi: [10.1103/PhysRevLett.115.231301](https://doi.org/10.1103/PhysRevLett.115.231301). arXiv:  
1792 [1503.02641 \[astro-ph.HE\]](https://arxiv.org/abs/1503.02641).
- 1793 [49] M. L. Ahnen et al. “Limits to Dark Matter Annihilation Cross-Section from a Combined  
1794 Analysis of MAGIC and Fermi-LAT Observations of Dwarf Satellite Galaxies”. In: *JCAP*  
1795 1602.02 (2016), p. 039. doi: [10.1088/1475-7516/2016/02/039](https://doi.org/10.1088/1475-7516/2016/02/039). arXiv: [1601.06590](https://arxiv.org/abs/1601.06590)  
1796 [astro-ph.HE].
- 1797 [50] Javier Rico et al. *gLike: numerical maximization of heterogeneous joint  
1798 likelihood functions of a common free parameter plus nuisance parameters*.  
1799 <https://doi.org/10.5281/zenodo.4601451>. Version v00.09.03. Mar. 2021. doi: [10.5281/zenodo.4601451](https://doi.org/10.5281/zenodo.4601451). URL: <https://doi.org/10.5281/zenodo.4601451>.
- 1801 [51] Tjark Miener and Daniel Nieto. *LklCom: Combining likelihoods from different experiments*.  
1802 <https://doi.org/10.5281/zenodo.4597500>. Version v0.5.3. Mar. 2021. doi: [10.5281/zenodo.4597500](https://doi.org/10.5281/zenodo.4597500). URL: <https://doi.org/10.5281/zenodo.4597500>.
- 1804 [52] T. Miener et al. “Open-source Analysis Tools for Multi-instrument Dark Matter Searches”.  
1805 In: *arXiv e-prints*, arXiv:2112.01818 (Dec. 2021), arXiv:2112.01818. arXiv: [2112.01818](https://arxiv.org/abs/2112.01818)  
1806 [astro-ph.IM].
- 1807 [53] Alex Geringer-Sameth and Matthew Koushiappas Savvas M. and Walker. “Dwarf galaxy  
1808 annihilation and decay emission profiles for dark matter experiments”. In: *Astrophys.  
1809 J.* 801.2 (2015), p. 74. doi: [10.1088/0004-637X/801/2/74](https://doi.org/10.1088/0004-637X/801/2/74). arXiv: [1408.0002](https://arxiv.org/abs/1408.0002)  
1810 [astro-ph.CO].

- 1811 [54] Gianfranco Bertone, Dan Hooper, and Joseph Silk. “Particle dark matter: evidence, can-  
1812 didates and constraints”. In: *Physics Reports* 405.5-6 (Jan. 2005), pp. 279–390. ISSN:  
1813 0370-1573. doi: [10.1016/j.physrep.2004.08.031](https://doi.org/10.1016/j.physrep.2004.08.031). URL: <http://dx.doi.org/10.1016/j.physrep.2004.08.031>.
- 1815 [55] V. Bonnivard et al. “Dark matter annihilation and decay in dwarf spheroidal galaxies: The  
1816 classical and ultrafaint dSphs”. In: *Mon. Not. Roy. Astron. Soc.* 453.1 (2015), pp. 849–867.  
1817 doi: [10.1093/mnras/stv1601](https://doi.org/10.1093/mnras/stv1601). arXiv: [1504.02048 \[astro-ph.HE\]](https://arxiv.org/abs/1504.02048).
- 1818 [56] A. et al. Albert. “Searching for Dark Matter Annihilation in Recently Discovered Milky Way  
1819 Satellites with Fermi-LAT”. in: *Astrophys. J.* 834.2 (2017), p. 110. doi: [10.3847/1538-4357/834/2/110](https://doi.org/10.3847/1538-4357/834/2/110). arXiv: [1611.03184 \[astro-ph.HE\]](https://arxiv.org/abs/1611.03184).
- 1821 [57] Mattia Di Mauro and Martin Wolfgang Winkler. “Multimessenger constraints on the dark  
1822 matter interpretation of the Fermi-LAT Galactic Center excess”. In: *prd* 103.12, 123005  
1823 (June 2021), p. 123005. doi: [10.1103/PhysRevD.103.123005](https://doi.org/10.1103/PhysRevD.103.123005). arXiv: [2101.11027 \[astro-ph.HE\]](https://arxiv.org/abs/2101.11027).
- 1825 [58] HongSheng Zhao. “Analytical models for galactic nuclei”. In: *Mon. Not. Roy. Astron. Soc.*  
1826 278 (1996), pp. 488–496. doi: [10.1093/mnras/278.2.488](https://doi.org/10.1093/mnras/278.2.488). arXiv: [astro-ph/9509122 \[astro-ph\]](https://arxiv.org/abs/astro-ph/9509122).
- 1828 [59] H. C. Plummer. “On the Problem of Distribution in Globular Star Clusters: (Plate 8.)”  
1829 In: *Monthly Notices of the Royal Astronomical Society* 71.5 (Mar. 1911), pp. 460–470.  
1830 ISSN: 0035-8711. doi: [10.1093/mnras/71.5.460](https://doi.org/10.1093/mnras/71.5.460). eprint: <https://academic.oup.com/mnras/article-pdf/71/5/460/2937497/mnras71-0460.pdf>. URL:  
1832 <https://doi.org/10.1093/mnras/71.5.460>.
- 1833 [60] Daniel R. Hunter. “Derivation of the anisotropy profile, constraints on the local velocity  
1834 dispersion, and implications for direct detection”. In: *JCAP* 02 (2014), p. 023. doi:  
1835 [10.1088/1475-7516/2014/02/023](https://doi.org/10.1088/1475-7516/2014/02/023). arXiv: [1311.0256 \[astro-ph.CO\]](https://arxiv.org/abs/1311.0256).
- 1836 [61] Barun Kumar Dhar and Liliya L. R. Williams. “Surface mass density of the Einasto family  
1837 of dark matter haloes: are they Sersic-like?” In: *Mon. Not. Roy. Astron. Soc.* (2010). doi:  
1838 [10.1111/j.1365-2966.2010.16446.x](https://doi.org/10.1111/j.1365-2966.2010.16446.x).
- 1839 [62] M. Baes and E. Van Hese. “Dynamical models with a general anisotropy profile”. In:  
1840 *Astron. Astrophys.* 471 (2007), p. 419. doi: [10.1051/0004-6361:20077672](https://doi.org/10.1051/0004-6361:20077672). arXiv:  
1841 [0705.4109 \[astro-ph\]](https://arxiv.org/abs/0705.4109).
- 1842 [63] Matthew G. Walker, Edward W. Olszewski, and Mario Mateo. “Bayesian analysis of re-  
1843 solved stellar spectra: application to MMT/Hectochelle observations of the Draco dwarf  
1844 spheroidal”. In: *mnras* 448.3 (Apr. 2015), pp. 2717–2732. doi: [10.1093/mnras/stv099](https://doi.org/10.1093/mnras/stv099).  
1845 arXiv: [1503.02589 \[astro-ph.GA\]](https://arxiv.org/abs/1503.02589).

- 1846 [64] Nicholas L. Rodd et al. “Dark matter spectra from the electroweak to the Planck scale”. In:  
1847       *J. High Energy Physics* 121.10.1007 (June 2021).
- 1848 [65] Pace, Andrew B and Strigari, Louis E. “Scaling relations for dark matter annihilation and  
1849       decay profiles in dwarf spheroidal galaxies”. In: *Monthly Notices of the Royal Astronomical  
1850       Society* 482.3 (Oct. 2018), pp. 3480–3496. ISSN: 0035-8711. doi: [10.1093/mnras/sty2839](https://doi.org/10.1093/mnras/sty2839).
- 1852 [66] Albert, A. et al. “Search for gamma-ray spectral lines from dark matter annihilation in  
1853       dwarf galaxies with the High-Altitude Water Cherenkov observatory”. In: *Phys. Rev. D* 101 (10 May 2020), p. 103001. doi: [10.1103/PhysRevD.101.103001](https://doi.org/10.1103/PhysRevD.101.103001). URL:  
1854       <https://link.aps.org/doi/10.1103/PhysRevD.101.103001>.
- 1856 [67] Victor Eijkhout and Edmund Show and Robert van de Geijn. *The Science of Computing.  
1857       The Art of High Performance Computing*. Vol. 3. Open Copy published under CC-BY 4.0  
1858       license, 2023, pp. 63–66.